NPS-61-86-008

NAVAL POSTGRADUATE SCHOOL
Monterey, California

THESIS

REMOTE MEASUREMENT OF THE ATMOSPHERIC ISOPLANATIC ANGLE AND DETERMINATION OF REFRACTIVE TURBULENCE PROFILES BY DIRECT INVERSION OF THE SCINTILLATION AMPLITUDE COVARIANCE FUNCTION WITH TIKHONOV REGULARIZATION

by

Kurt Benedict Stevens

December 1985

Dissertation Supervisor: D. L. Walters

Prepared for Rome Air Development Center (RADC/OCSP, Dr. Don Hanson), Griffiss AFB, New York

NAVAL POSTGRADUATE SCHOOL
Monterey, California 93943

Rear Admiral R.H. Shumaker
Superintendent

D. A. Schrady
Provost

This thesis prepared in conjunction with research sponsored by the Space Defense Initiative Organization through Rome Air Development Center under NPS-61-86-008.

Released by:

ITY CLASSIFICATION OF THIS PAGE

REPORT DOCUMENTATION PAGE

EPORT SECURITY CLASSIFICATION JNCLASSIFIED	1b. RESTRICTIVE MARKINGS
ECURITY CLASSIFICATION AUTHORITY	3. DISTRIBUTION/AVAILABILITY OF REPORT Approved for public release; distribution is unlimited
ECLASSIFICATION/DOWNGRADING SCHEDULE	
RFORMING ORGANIZATION REPORT NUMBER(S) NPS-61-86-008	5. MONITORING ORGANIZATION REPORT NUMBER(S)
AME OF PERFORMING ORGANIZATION val Postgraduate School 6b. OFFICE SYMBOL (If applicable) 61	7a. NAME OF MONITORING ORGANIZATION Space Defense Initiative Organization (SDIO/DE)
DDRESS (City, State, and ZIP Code) nterey, California 93943-5100	7b. ADDRESS (City, State, and ZIP Code) 1717 H Street Washington, D.C. 20301
AME OF FUNDING/SPONSORING RGANIZATION Rome Air Develop-t Center (RADC) Dr. Don Hanson 8b. OFFICE SYMBOL (If applicable) OCSP	9. PROCUREMENT INSTRUMENT IDENTIFICATION NUMBER FQ761940016
DDRESS (City, State, and ZIP Code) riffiss AFB, New York 13441	10. SOURCE OF FUNDING NUMBERS PROGRAM ELEMENT NO. / PROJECT NO. / TASK NO. / WORK UNIT ACCESSION NO.

TLE (Include Security Classification) REMOTE MEASUREMENT OF THE ATMOSPHERIC ISOPLANATIC ANGLE AND TERMINATION OF REFRACTIVE TURBULENCE PROFILES BY DIRECT INVERSION OF THE SCINTILLATION PLITUDE COVARIANCE FUNCTION WITH TIKHONOV REGULARIZATION

ERSONAL AUTHOR(S) Stevens, Kurt B.

TYPE OF REPORT	13b. TIME COVERED	14. DATE OF REPORT (Year, Month, Day)	15 PAGE COUNT
D. Dissertation	FROM _____ TO _____	1985 December	170

UPPLEMENTARY NOTATION This work was supported by the Space Defense Initiative Organization ough Rome Air Development Center. ARPA Order #4021, Program Code #4E20, Amendment #31. ounting: D14 4713 4E200 040210 41526 62301E 503901 F03901 D0210017

COSATI CODES		
IELD	GROUP	SUB-GROUP

18. SUBJECT TERMS (Continue on reverse if necessary and identify by block number)
Isoplanatic angle
Refractive turbulence profiles
Stellar scintillation
Apodization
Tikhonov regularization

BSTRACT (Continue on reverse if necessary and identify by block number)

It is difficult to propagate a diffraction-limited laser beam through the mosphere, since the atmosphere contains random index of refraction fluctuations. o parameters that characterize the atmosphere for optical propagation are the mospheric isoplanatic angle, θ_o, and the refractive turbulence structure parameter, ^{2}. This dissertation deals with improved methods for measuring θ_o and C_n^2 profiles ing optical techniques.

By apodizing the receiver telescope aperture, one can improve the weighting function r isoplanatic angle measurement substantially over previous systems. We find that e weighting function is not significantly affected by inner scale changes with titude and that the error in isoplanatic angle measurement from strong low altitude rbulence ($z < 1$ km) with this weighting function is small. Data collected with the (continued)

ISTRIBUTION/AVAILABILITY OF ABSTRACT UNCLASSIFIED/UNLIMITED ☐ SAME AS RPT. ☐ DTIC USERS	21. ABSTRACT SECURITY CLASSIFICATION UNCLASSIFIED
NAME OF RESPONSIBLE INDIVIDUAL D. L. Walters	22b. TELEPHONE (Include Area Code) 408-646-2267 22c. OFFICE SYMBOL 61We

ORM 1473, 84 MAR 83 APR edition may be used until exhausted. All other editions are obsolete.

SECURITY CLASSIFICATION OF THIS PAGE

19. (Continued)

improved isoplanometer shows temporal trends in the isoplanatic angle on the order of 90 seconds that have not been observed before.

Direct inversion of the amplitude covariance function (including aperture averaging effects) to yield refractive turbulence profiles is known to be ill-posed. I suppress this condition using Tikhonov regularization and reproduce refractive turbulence profiles from actual C_n^2 data with some success.

Approved for public release; distribution is unlimited

Remote Measurement of the Atmospheric Isoplanatic Angle and Determination of Refractive Turbulence Profiles by Direct Inversion of the Scintillation Amplitude Covariance Function with Tikhonov Regularization

by

Kurt Benedict Stevens
Captain, United States Air Force
B.S., United States Air Force Academy, 1979
M.S., Naval Postgraduate School, 1983

Submitted in partial fulfillment of the
requirements for the degree of

DOCTOR OF PHILOSOPHY

from the

NAVAL POSTGRADUATE SCHOOL
December 1985

ABSTRACT

It is difficult to propagate a diffraction-limited laser beam through the atmosphere, since the atmosphere contains random index of refraction fluctuations. Two parameters that characterize the atmosphere for optical propagation are the atmospheric isoplanatic angle, θ_o, and the refractive turbulence structure parameter, C_n^2. This dissertation deals with improved methods for measuring θ_o and C_n^2 profiles using optical techniques.

By apodizing the receiver telescope aperture, one can improve the weighting function for isoplanatic angle measurement substantially over previous systems. We find that the weighting function is not significantly affected by inner scale changes with altitude and that the error in isoplanatic angle measurement from strong low altitude turbulence ($z < 1$ km) with this weighting function is small. Data collected with the improved isoplanometer shows temporal trends in the isoplanatic angle on the order of 90 seconds that have not been observed before.

Direct inversion of the amplitude covariance function (including aperture averaging effects) to yield refractive turbulence profiles is known to be ill-posed. I suppress this condition using Tikhonov regularization and reproduce refractive turbulence profiles from actual C_n^2 data with some success.

TABLE OF CONTENTS

I. INTRODUCTION 9

II. BACKGROUND 11

A. GENERAL DESCRIPTION OF TURBULENCE 11

B. STATISTICAL DESCRIPTION OF TURBULENCE 16

1. Random Variables 16

2. Homogeneity and Isotropy 16

3. Structure Functions 17

4. Covariance Functions and Spectra 20

C. EM PROPAGATION THEORY IN TURBULENCE 25

1. Solving the Wave Equation 25

2. The Rytov Approximation 28

3. The Huygens-Fresnel Approach 31

4. The Modulation Transfer Function Approach 35

5. Measures of Spatial Coherence 36

6. Intensity Fluctuations 39

7. Problems in the Theory 42

III. REMOTE MEASUREMENTS OF THE ISOPLANATIC ANGLE . . . 44

A. TECHNIQUE 44

B. THE FIRST ISOPLANOMETERS 46

C. APERTURE APODIZATION FOR WEIGHTING FUNCTION IMPROVEMENT 47

1. Weighting Functions for the Top Hat Aperture 47

2. Improved Weighting Functions 54

3. Double Annulus Calibration 62

4. Double Annulus Improvements 66

IV. APODIZED ISOPLANOMETER SENSITIVITY ANALYSIS 67

A. WEIGHTING FUNCTION PERFORMANCE IN STRONG TURBULENCE 67

1. The C_n^2 Profile 68

2. The Analysis 69

B. INNER SCALE EFFECTS 71

1. Constructing the Inner Scale as a Function of Altitude 71

2. Weighting Function Dependence on the Inner Scale 74

C. SENSITIVITY ANALYSIS CONCLUSIONS 77

V. INSTRUMENT QUALIFICATION 80

A. HARDWARE 80

1. Telescope 80

2. Detector 81

3. Signal Conditioning and Isoplanatic Angle Extraction 83

B. ZENITH ANGLE QUALIFICATION TESTS 84

C. APODIZED AND 10 cm ISOPLANOMETER COMPARISON . . 89

D. ISOPLANATIC ANGLE MEASUREMENTS WITH SUPPORTING METEOROLOGICAL DATA 89

E. QUALIFICATION CONCLUSIONS 95

VI. DATA COLLECTED IN MAUI 96

VII. REFRACTIVE TURBULENCE PROFILING 106

A. PREVIOUS WORK 107

1. Remote Probing with Apodized Apertures 108

2. Binary Star Techniques 109

B. INVERSION WITH TIKHONOV REGULARIZATION 109

1. Inverting the Fredholm Equation 110

2. Constructing the Filter Function 117

3. Noise Computations 124

4. Inversion Conclusions 126

VIII. NUMERICAL SIMULATION OF THE AMPLITUDE COVARIANCE FUNCTION INVERSION WITH TIKHONOV REGULARIZATION 127

A. CONSTRUCTING THE C_N^2 AND SCINTILLATION SPECTRA 127

B. CONSTRUCTING THE COVARIANCE FUNCTION 132

C. CONSTRUCTING THE SCINTILLATION SPECTRUM AND APPLYING TIKHONOV REGULARIZATION 135

D. REGULARIZATION CONCLUSIONS 142

IX. CONCLUSIONS 146

A. ISOPLANATIC ANGLE MEASUREMENT 146

B. REFRACTIVE TURBULENCE PROFILING 148

APPENDIX A: OTHER WEIGHTING FUNCTIONS 149

APPENDIX B: MAUI METEOROLOGICAL BALLOON DATA 158

LIST OF REFERENCES 163

INITIAL DISTRIBUTION LIST 168

ACKNOWLEDGEMENT

Briefly, I would like to thank my Ph.D. Committee members for their advice and support, especially my mentor, D. L. Walters. A note of thanks to my parents whose love and devotion provided a wonderful environment in which to grow. And most especially, I thank my wife, Kathy, without whom I could not have endured.

I. INTRODUCTION

If one wishes to propagate a spatially and temporally coherent electromagnetic wave through the atmosphere or any random medium without distortion, one must somehow compensate for the random phase and amplitude perturbations induced by the medium. Adaptive optics is the field of physics that attempts to compensate for propagation through the atmosphere, principally by deforming mirrors and unconventionally by using nonlinear optical materials. In order to successfully conjugate the effects of the atmosphere, knowledge of certain atmospheric parameters is crucial. These parameters are the isoplanatic angle (θ_o), the spatial coherence length of the atmosphere, (r_o, ρ_o) and vertical profiles of the refractive turbulence structure parameter, C_n^2. This dissertation deals with the theory and measurement of the isoplanatic angle and the refractive turbulence structure parameter. Currently, reliable systems exist for the measurement of the spatial coherence length of the atmosphere [Refs. 1, 2].

The isoplanatic angle is an angular measure of spatial coherence in the atmosphere. Walters of [Ref. 1] has developed three generations of instruments (known as isoplanometers) to measure the isoplanatic angle. This work

has to do in part with the development and test of a fourth generation isoplanometer having an improved weighting function. This instrument is optimized for night use and provides temporally high resolution data (1 second samples), able for the first time to measure trends with periods less than five minutes. Two fourth generation isoplanometers are currently operating at different locations.

Of the three parameters noted, the most important is the refractive turbulence C_n^2 profile. Both the isoplanatic angle, θ_o, and spatial coherence length, r_o are functions of C_n^2. Hence, knowledge of the C_n^2 profile not only gives a picture of turbulence with altitude, but also gives the measures of spatial coherence, r_o and θ_o. Unfortunately, high vertical resolution profiles of C_n^2 are difficult to measure. Several measurement techniques exist, each having its strengths and weaknesses. These techniques will be discussed later. This research attempts remote measurement of C_n^2 by direct inversion of the stellar scintillation amplitude covariance function. Mathematically, the problem is ill-posed meaning that noise in the data makes inversion impossible. Different regularization techniques exist to make the problem tractable. This work is an extension of [Refs. 3, 4] using the Tikhonov regularization technique [Ref. 5] to invert the covariance function for two finite but arbitrary equal apertures.

II. BACKGROUND

A. GENERAL DESCRIPTION OF TURBULENCE

Turbulence has certain characteristics that differentiate it from other flow patterns. In [Ref. 8], Lumley briefly describes these characteristics as I will do here. The first quality of turbulence almost goes without saying; turbulence is irregular. This "quality" has a profound effect on how one approaches a mathematical model or description of turbulence. Fluid dynamics for years relied on the application of Newton's laws to fluids. With the Navier-Stokes equations in hand, one in principle should be able to solve any problem. However, in the case of irregular flows, the randomness makes this approach impotent and we are left with having to use statistical methods.

Diffusivity is a property responsible for rapidly mixing and spreading basic physical quantities like momentum, mass and heat. This property is present in all turbulent flows.

Turbulent flows are always characterized by large Reynolds numbers. The Reynolds number, Re, is given by

$$Re = \frac{vL}{\nu}$$

where v is the velocity, L is a characteristic dimension of the entire flow and ν is the viscosity. As the Reynolds number moves beyond a certain critical value, Re_c, (nominally $Re_c \approx 100$, for pipe flow) [Ref. 9], the flow becomes unstable giving way to turbulence. The value of the critical Reynolds number depends on the type of flow. Re_c for the atmosphere is approximately 2000 [Ref. 14].

Another important property of turbulence is that it is characterized by three dimensional vorticity fluctuations. The vorticity fluctuations find their origin in the velocity field. In order to support the random vorticity fluctuations, the random velocity field must also be three dimensional. Lumley's example of a two dimensional atmospheric cyclone is worth noting. Large scale cyclonic behavior responsible for weather patterns is itself not turbulent. This does not mean, however, that the cyclone is not made up of smaller scale turbulent bodies.

Within every turbulent flow is a mechanism that dissipates energy. The dissipation occurs at small scale sizes and is a function of the viscosity of the fluid. The dissipated energy is internalized into the fluid typically as heat. Clearly, if one increases the rate at which energy is added to a fluid, the dissipation rate, ε, must also rise proportionately to conserve energy. This occurs after the energy increase has reached the smallest scale sizes.

The last two properties in Lumley's list are rather obvious but still should be noted. First, turbulence lies within the continuum model of fluid mechanics. The scale sizes in turbulence are typically much larger than molecular sizes. Thus, molecular diffusion does not significantly affect turbulent flows. And lastly, turbulent flows in fluids are indeed flows. In principle, as I mentioned previously, the Navier-Stokes equations provide the general equations for fluid flows. For turbulence, one is concerned with the statistics of the Navier-Stokes equations. Unfortunately, the solution to this set of equations is not known since the number of unknowns exceeds the number of equations. This is known as the "closure" problem of the Navier-Stokes equations [Ref. 10].

As was mentioned earlier, turbulence is an irregular or random process. Finding exact scale sizes, dissipation rates, etc., is virtually impossible. However, it is possible to extract order of magnitude values by dimensional analysis. This technique is used in the turbulence field to mathematically model the phenomenon. Other techniques include asymptotic invariance (the model should behave properly as the Reynolds number approaches infinity) and local invariance (depending on the time and length scales in the turbulence, one may be able to assume that the turbulence is everywhere similar). These three techniques,

in varying degrees, find their way into the treatment of turbulence.

All mechanical processes must have an energy source. In turbulence, the source is principally shear flows within the mean flow. This is true for turbulence outside the atmospheric boundary layer. The boundary layer is formed by the interaction of the flow and the earth's surface given the no slip condition [Ref. 8]. Buoyancy can also be an energy source. With an energy source available, a laminar flow can become turbulent. The laminar portion of the flow is modeled by the linearized theories valid for small perturbations much like the classical or quantum harmonic oscillator. The turbulent portion of the flow is mathematically treated using an asymptotic theory valid for high Reynolds numbers. This inevitably leads to chaos in the transition region.

In turbulence there are a number of different length scales. A description of all the different length scales is a key component of similarity theory [Ref. 10]. However, two important ones are covered now. First, the outer scale, typically noted as L_o, is the size of the turbulence at onset (on the order of meters). The outer scale, given by $L_o = Re\ \nu/v$, is a function of the Reynolds number, viscosity and velocity of the fluid as mentioned earlier. In the outer scale, viscosity does not play a role in the

dissipation of energy since inertial terms dominate the equations of motion. However, at the inner scale or microscale (on the order of millimeters), viscosity internalizes the energy of the turbulence as heat. Clearly, from what has already been said, the key parameters at the inner scale are the dissipation rate and viscosity. Using dimensional analysis, Kolmogorov formed length, time and velocity scales valid at the microscale [Ref. 11]. These are called the Kolmogorov microscales and their exact expressions can be noted in [Ref. 8].

Now, we can construct a physical picture of the formation and dissipation of turbulence. The onset of turbulence occurs at the outer scale. If the Reynolds number at the outer scale is again greater than the critical Reynolds number for turbulence formation, the turbulence at the outer scale will again break down. The formation of continually smaller eddies occurs until $Re < Re_c$ and the turbulence is at the inner scale. Hence, energy from the ordered flow moves through the turbulence "cascade" to the inner scale where it is dissipated in random processes. The region of scale sizes between the inner and outer scale is known as the inertial subrange. The energy transfer from one scale size to the next is adiabatic in the inertial subrange. Hence, the entropy increase occurs at the inner scale. This view of turbulence is appealing since it is so

closely related to the second law of thermodynamics. We might expect that the inertial subrange has a well defined spectrum. It does, and this will be covered later.

B. STATISTICAL DESCRIPTION OF TURBULENCE

1. Random Variables

Since turbulence is irregular and random, it is most effectively described statistically. Hence, variables like the velocity $\vec{v}(t)$, become random variables having a mean and higher statistical moments. In many stochastic processes, the statistical moments do not change with time or are stationary. However, with atmospheric turbulence this is not the case. The nonstationarity of turbulence makes the meaning of long term averages, etc., questionable. In addition, the replacement of ensemble averages by time averages (ergodic assumption) presents additional difficulties. This complicates the description of turbulence considerably.

2. Homogeneity and Isotropy

Along with stationarity, most well-behaved random variables are homogeneous and isotropic. Homogeneity means that statistical quantities do not change with a Galilean transformation of coordinates. This implies that mathematically, functions describing statistics at $\vec{r}_1$ and $\vec{r}_2$ depend only on the difference $\vec{r}_{12} = \vec{r}_1 - \vec{r}_2$. Isotropy implies a symmetry in rotations of $\vec{r}_1$ and $\vec{r}_2$. Hence, if the

statistics are homogeneous and isotropic, functions depending on $\vec{r}_1$ and $\vec{r}_2$ can be represented by $|\vec{r}_1 - \vec{r}_2|$.

Unfortunately, the atmosphere provides neither homogeneous nor isotropic random variables. However, Tatarski in [Ref. 6] adopts the idea of local homogeneity and isotropy. Over some region R, comparable to the outer scale L_o, the statistics of the random variables do not change with translations and rotations.

In a similar manner, Tatarski handles the non-stationary problem. He notes that the functions can be stationary over time increments or stationary increments. Hence, it is possible to tolerate slow drifts in the mean and other moments.

3. Structure Functions

Another way to cope with the non-stationary problem is to define a function in terms of a difference. Tatarski defines the structure function for temperature as

$$D_T(\vec{r}_1,\vec{r}_2) = < [T(\vec{r}_2) - T(\vec{r}_1)]^2 > \quad . \tag{2.1}$$

< > denotes an ensemble average. We should note that the structure function depends upon the vectors $\vec{r}_1$ and $\vec{r}_2$. If we assume homogeneity and isotropy, this reduces to

$$D_T(r) = < [T(r_2) - T(r_1)]^2 > \quad , \tag{2.2}$$

where $r = |\vec{r}_2 - \vec{r}_1|$. Also, in differencing $T(r_1)$ and $T(r_2)$, effects of a changing mean are removed.

Kolmogorov showed [Refs. 6, 8] by dimensional analysis that the structure function for temperature fluctuations in the inertial subrange is given by

$$D_T(r) = C_T^2 r^{2/3} \quad , \tag{2.3}$$

where C_T^2 is the temperature structure parameter. In EM propagation, one is more concerned with index of refraction than temperature. So, we can define an index of refraction structure function, $D_n(r)$, similar to (2.2) and (2.3),

$$D_n(r) = C_n^2 r^{2/3} \quad , \tag{2.4}$$

where C_n^2 is the refractive turbulence structure parameter.

In order to model the turbulence correctly, one must use quantities that are not affected by position in the fluid. We refer to such quantities as "passive additives". Temperature is not a passive additive since it changes with vertical displacements. However, potential temperature, θ, given by $\theta = T - \Gamma z$ where Γ is the adiabatic lapse rate and z is altitude, is a passive additive since it is corrected for changes in altitude.

Figure 2.1 taken from [Ref. 14] shows the behavior of $D_T(r)$ as a function of log(r). Clearly, if $r < l_o$ the

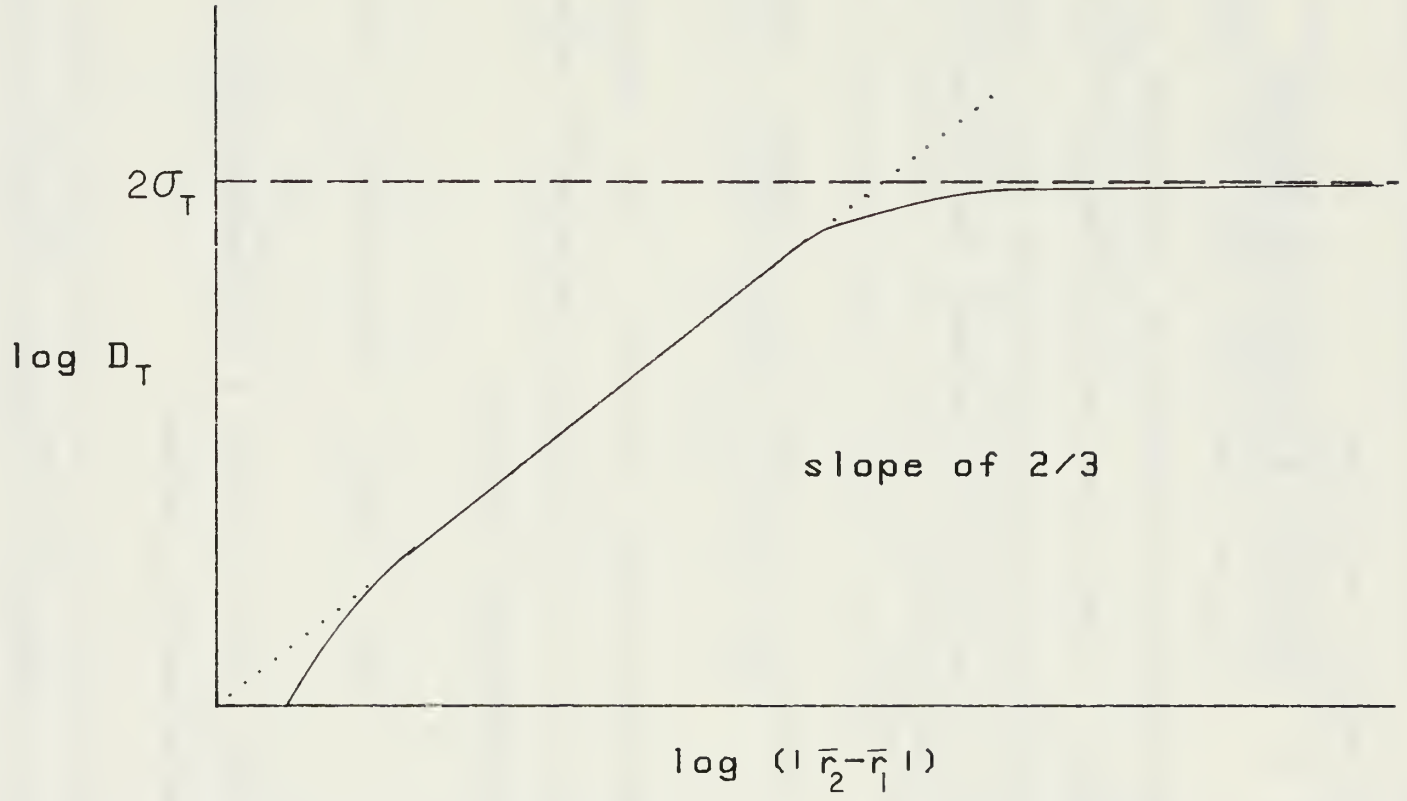

Figure 2.1 Temperature Structure Function, D_T, as a Function of Separation Between Two Vectors

inner scale, $D_T(r) = 0$ and for $r > L_o$, $D_T(r)$ approaches $2\sigma_T^2$ asymptotically as the fluctuations become uncorrelated. Hence, the structure function has a well defined slope in the inertial subrange.

4. Covariance Functions and Spectra

Along with structure functions, covariance functions (or correlation functions if normalized) and spectra are useful in describing random processes. Conveniently, covariance functions and spectra form a Fourier transform pair. The covariance between two random variables S and T is given by

$$B_{ST} = \langle [T(r_1) - \langle T(r_1) \rangle][S(r_2) - \langle S(r_2) \rangle] \rangle, \quad (2.5a)$$

where the average value of T, $\langle T(r) \rangle$ has different definitions if T is continuous or discrete. Often one uses the autocovariance function

$$B_{TT} = \langle [T(r_1) - \langle T(r_1) \rangle][T(r_2) - \langle T(r_2) \rangle] \rangle. \quad (2.5b)$$

If the random variable T is homogeneous or locally homogeneous B_{TT} becomes

$$B_{TT} = \langle T(r_1)T(r_2) \rangle - \langle T(r_1) \rangle^2 \quad . \quad (2.6)$$

If we choose <T>=0 this reduces to

$$B_{TT} = \langle T(r_1)T(r_2)\rangle \quad . \tag{2.7}$$

There is a relationship between structure functions and covariance functions given by, [Ref. 6],

$$D_T(r) = 2[B_{TT}(0) - B_{TT}(r)] \quad . \tag{2.8}$$

As mentioned earlier, the covariance function and the power spectral density form a Fourier transform pair. The power spectral density gives one insight into how different frequency components contribute to the variance. For one dimensional spectra, the transform pair is

$$W(K) = \int_{-\infty}^{\infty} e^{-irK} B(r)\, dr \tag{2.9}$$

and

$$B(r) = \frac{1}{2\pi} \int_{-\infty}^{\infty} e^{irK} W(K)\, dK \quad . \tag{2.10}$$

But, before these relations hold, we must realize again that the functions involved are random. A random function

f(r) can be decomposed using Fourier-Stieltjes integrals given by

$$f(r) = \int_{-\infty}^{\infty} e^{iKr}\, d\phi(K) \tag{2.11}$$

where $d\phi(K)$ is a random complex amplitude. The Fourier-Stieltjes integral must be used since the random fluctuations are uncorrelated over non-overlapping intervals [Ref. 12]. Hence, f(r) does not have a derivative and is non-Riemann integrable.

With the substitution of the Fourier-Stieltjes integral, the covariance function is

$$B(r_1+r, r_1) = \iint e^{[i(K[r_1+r] - K'r_1]} \langle d\phi(K) d\phi^*(K') \rangle \,. \tag{2.12}$$

If the medium is homogeneous, $B(r_1+r, r_1) = B(r)$, since an average must not depend on the location within the medium. For the double integral to only depend on r, the following must be true,

$$\langle d\phi(K) d\phi^*(K') \rangle = \delta(K-K')W(K)dKdK' \,. \tag{2.13}$$

We note that $\langle d\phi(K) d\phi^*(K') \rangle$ is in the form of a mutual coherence function (MCF), which represents the overlap of

$d\phi(K)$ and $d\phi^*(K)$. Since the $d\phi$'s are uncorrelated except at $K = K'$, we get the Dirac delta function with the spectrum $W(K)$ giving the amplitude. Substituting (2.13) into (2.12) and integrating over K' gives (2.10).

Since we are dealing with fluctuations of the random variable T, the mean value is assumed zero giving

$$\sigma^2 = \int_{-\infty}^{\infty} W(K)dK \quad . \tag{2.14}$$

From (2.8) and (2.10) we see immediately that

$$D(r) = \frac{1}{\pi} \int_{-\infty}^{\infty} [1 - \cos(rK)]\, W(K)dK \quad , \tag{2.15}$$

since $B(r)$ is an even function.

Tatarski [Ref. 6] develops an expression for $W(K)$ based upon the form of the structure function for turbulence. The one-dimensional spectra $W(K)$ is given by

$$W(K) = \alpha\, \varepsilon^{2/3}\, K^{-5/3} \quad , \tag{2.16}$$

where α is a constant and ε is the dissipation rate.

Vector fields like the velocity, $\vec{v}(\vec{r})$, are expressed in three dimensions. Hence, their spectra are three dimensional. We will let $\Phi(\vec{K})$ denote this power spectral density. $\Phi(\vec{K})$ is given by

$$\Phi(\vec{K}) = \iiint d^3\vec{r} e^{-i\vec{K}\cdot\vec{r}} B(\vec{r}) \quad . \tag{2.17}$$

The covariance function is defined similarly. $B(\vec{r})$ is given by

$$B(\vec{r}) = \frac{1}{(2\pi)^3} \iiint d^3\vec{K} e^{i\vec{K}\cdot\vec{r}} \Phi(\vec{K}) \quad . \tag{2.18}$$

Equation (2.18) is also developed from a Fourier-Stieltjes approach requiring homogeneity. For spherical coordinates,

$$d^3\vec{r} = r^2 \sin\theta dr d\theta d\phi \quad ,$$

and the θ and ϕ integrals in (2.17) can be completed giving

$$\Phi(K) = \frac{1}{2\pi^3 K} \int_0^\infty B(r) \sin(rK) r dr \quad . \tag{2.19}$$

A similar relation for the covariance function can also be found. Tatarski uses the relation

$$\Phi(K) = \frac{-1}{2\pi K} \frac{dW(K)}{dK} \tag{2.20}$$

to evaluate the three dimensional spectrum in terms of the one dimensional spectrum. This gives

$$\Phi(K) = \alpha C_n^2 K^{-11/3} \tag{2.21}$$

for the passive additive, index of refraction, where α is a constant. This is known as the Kolmogorov spectrum (since Kolmogorov did the original work), valid in the inertial subrange. Spectra have also been developed for the production and dissipation regions of turbulence [Ref. 13].

C. EM PROPAGATION THEORY IN TURBULENCE

Clifford [Ref. 15] covers Tatarski's work [Ref. 6] for weak turbulence. This treatment is analogous to any application of first order perturbation theory. The following is Clifford's treatment in a more condensed form.

1. Solving the Wave Equation

Consider a sinusoidal wave of the form $e^{-i\omega t}$ where the atmosphere has zero conductivity and unit magnetic permeability. For these conditions, Maxwell's equation in Gaussian units become:

$$\nabla \cdot \vec{H} = 0 \ , \tag{2.22}$$

$$\nabla \times \vec{E} = ik\vec{H} , \tag{2.23}$$

$$\nabla \times \vec{H} = -ikn^2\vec{E} , \tag{2.24}$$

$$\nabla \cdot (n^2\vec{E}) = 0 , \tag{2.25}$$

where k is the wavenumber of the electromagnetic wave and n is the index of refraction. We generate the wave equation for $\vec{E}$ in the usual way by substituting (2.24) into the curl of (2.23) giving

$$-\nabla^2\vec{E} + \nabla(\nabla \cdot \vec{E}) = k^2n^2\vec{E} . \tag{2.26}$$

We can expand (2.25) and solve for $\nabla \cdot \vec{E}$. Substituting into (2.26) gives

$$\nabla^2\vec{E} + k^2n^2\vec{E} + 2\nabla(\vec{E} \cdot \nabla \log n) = 0 . \tag{2.27}$$

If we assume that depolarization effects are negligible (i.e. assume isotropy), the last term of (2.27) can be neglected. Clearly, one need only consider a single scalar equation, since all the components follow in the mathematics. Thus, the scalar wave equation becomes

$$\nabla^2E + k^2n^2E = 0 . \tag{2.28}$$

Clifford now applies the method of small perturbations. This means that E can be expressed as a series of decreasing values,

$$E = E_0 + E_1 + E_2 + \ldots \quad . \tag{2.29}$$

E_0 corresponds to the unscattered wave, E_1 to single scattering, E_2 to double scattering and so on. In some situations the series may diverge, particularly if C_n^2 is large or the path length long. This leads to the phenomenon of saturation. Clifford uses the first order approximation giving

$$\nabla^2 E_0 + k^2 E_0 = 0$$

and

$$\nabla^2 E_1 + k^2 E_1 + 2k^2 n_1 E_0 = 0 \quad . \tag{2.30}$$

All terms of order two have been neglected. Clifford like Tatarski assumes a unit amplitude wave propagating in the z direction. This allows us to use the standard Green's function solution for $E_1(\vec{r})$,

$$E_1(\vec{r}) = \frac{1}{4\pi} \int_{Vol} d^3\vec{r}' \, \frac{e^{ik|\vec{r}-\vec{r}'|}}{|\vec{r} - \vec{r}'|} \, [2k^2 n_1(\vec{r}') e^{ikz'}] \quad . \tag{2.31}$$

For laser propagation, most of the monochromatic light will be scattered into a small forward cone. Hence, backscatter is negligible. Clifford now applies the Fresnel approximation to $E_1(\vec{r})$ giving

$$E_1(\vec{r}) = \frac{k^2 e^{ikz}}{2\pi} \int_{Vol} d^3\vec{r}' \exp\left\{\frac{ik[(\vec{\rho}-\vec{\rho}')^2]}{2(z-z')}\right\} \frac{n_1(\vec{r}')}{(z-z')} , \quad (2.32)$$

where $\vec{\rho}$ are the coordinates transverse to the propagation direction z.

2. The Rytov Approximation

At this point both Clifford and Tatarski apply the Rytov approximation which assumes that the solution of the stochastic wave equation is of the form

$$E = Ae^s , \quad (2.33)$$

where A is an amplitude and s is a complex phase. The Rytov solution involves the perturbed wave equation (2.30) divided by E_0. Tatarski gives this equation as

$$\frac{\nabla^2 E}{E} + k^2 n^2(\vec{r}) = \nabla^2 \log E + (\nabla \log E)^2 + k^2 n^2(\vec{r}) . \quad (2.34)$$

This combination of solution and wave equation is known as the method of smooth perturbations. The name comes from the

fact that we require the perturbations to be small over the distance of a wavelength. This condition is less restricting than those for the method of small perturbations.

From (2.33), the ratio of E/E_0 where $E = E_0 + E_1$ is

$$\frac{E}{E_0} = 1 + \frac{E_1}{E_0} = \frac{A}{A_0} \exp[i(S - S_0)] \quad . \tag{2.35}$$

Taking the natural logarithm of (2.35) and expanding in a power series gives Clifford's result,

$$\frac{E_1}{E_0} \simeq \frac{A_1}{A_0} + i(S - S_0) \quad . \tag{2.36}$$

Thus, the Rytov approximation has allowed us to obtain amplitude and phase information from the Green's function solution to the wave equation. Tatarski and others have developed the convention

$$\chi = \ell n(A/A_0) \simeq \frac{A_1}{A_0} \tag{2.37}$$

and

$$S - S_0 = S_1 \quad .$$

This is convenient since an experiment measures the log amplitude χ. It is trivial to obtain the forms for A_1/A_0 and $(S - S_0)$ from (2.32). But it is not so trivial to move

on from there. The problem is completing the integral over the random function $n_1(\vec{r})$. If one considers the plane wave propagating in a layered media, where at a given z, there exists statistical homogeneity, we can expand $n_1(\vec{r})$ in a two-dimensional Fourier-Stieltjes integral. We also assume that each layer is uncorrelated so that an integral along the path is a sum of incoherent additions. In the notation of Clifford, $n_1(\vec{r}_1')$ becomes

$$n_1(\vec{r}') = \int d\nu(\vec{K},z')e^{i\vec{K}\cdot\vec{\rho}} \quad , \tag{2.38}$$

where $d\nu(\vec{K},z')$ is the complex Fourier-Stieltjes amplitude. Substituting this into the relations for A_1/A_0 and $(S - S_0)$ gives

$$\begin{bmatrix} \chi(\vec{r}) \\ S_1(\vec{r}) \end{bmatrix} = \frac{k^2}{2\pi} \int_0^z dz' \frac{d\nu(\vec{K},z')}{(z-z')} \int d^2\vec{\rho}' e^{i\vec{K}\cdot\vec{\rho}'} \begin{Bmatrix} \cos \left[\frac{k(\vec{\rho}-\vec{\rho}')^2}{2(z-z')}\right] \\ \sin \left[\frac{k(\vec{\rho}-\vec{\rho}')^2}{2(z-z')}\right] \end{Bmatrix} , \tag{2.39}$$

where $d^3\vec{r}' = dz'd^2\vec{\rho}'$. $\chi(\vec{r})$ refers to the cosine of the bracketed quantity while $S_1(\vec{r})$ to the sine. One can perform the $\vec{\rho}'$ integrations leaving the Fourier-Stieltjes integration and the z' integration. Now we can construct the two-dimensional covariance functions exactly as before. $B_\chi(\vec{\rho},z)$ is

$$B_\chi(\vec{\rho},z) = \langle \chi(\vec{\rho}_1 + \vec{\rho}, z)\ \chi^*(\vec{\rho}_1,z) \rangle \quad . \tag{2.40}$$

Tatarski finds the spectrum from (2.40) to be

$$F_\chi(K,z'-z''=0) = F_\chi(K,0) = 2\pi k^2 \int_0^L \Phi(K) \sin^2\left[\frac{K^2(L-z)}{2k}\right] dz \tag{2.41}$$

and

$$F_s(K,0) = 2\pi k^2 \int_0^L \Phi(K) \cos^2\left[\frac{K^2(L-z)}{2k}\right] dz \quad ,$$

where L is the path length and $\Phi(K)$ is the three-dimensional Kolmogorov spectrum.

3. The Huygens-Fresnel Approach

As we have seen, Tatarski and Clifford use the differential equations approach to solving the turbulence problem. Since we have linear operators, etc., the identical problem can be formulated in terms of integral equations. This is Huygens-Fresnel theory applied to propagation in turbulence. Lutomirski and Yura [Refs. 16, 17] develop an extended Huygens-Fresnel theory by adding a random phase term to the Huygens-Fresnel integral. In fact, it is equivalent to applying the Rytov approximation to the integral equation. After applying the paraxial approximation, the extended integral equation becomes

$$E(\vec{r}) = \frac{-ik}{2\pi} \int_S \frac{e^{(ik|\vec{r}-\vec{r}'|)}}{|\vec{r}-\vec{r}'|} E(\vec{r}')e^{[\psi(\vec{r})]} d^2\vec{r}' \quad , \tag{2.42}$$

where ψ is a complex phase (equivalent to S_1, Yura's notation), the primes denote aperture coordinates and the non-primes denote image plane coordinates. The Huygens-Fresnel integral is developed in standard texts like [Ref. 18]. We should note that (2.42) reduces to the Green's function solution of Tatarski and Clifford in the geometrical optics limit (i.e., $\psi = k\int n_1(z)dz$). This is not surprising since the kernal of the Huygens-Fresnel integral is a Green's function.

Yura now finds the average intensity $\langle I(r)\rangle$,

$$\langle I(r)\rangle = \left\langle \frac{k^2}{2\pi} \int\int \frac{e^{[ik(|\vec{r}-\vec{r}'|-|\vec{r}-\vec{r}''|)]}}{|\vec{r}-\vec{r}'|\ |\vec{r}-\vec{r}''|} E^*(\vec{r}'')E(\vec{r}') \right.$$

$$\left. \times\ e^{(\psi'+\psi''^*)}\ d^2\vec{r}'d^2\vec{r}'' \right\rangle \quad . \tag{2.43}$$

The only functions in (2.43) that depend on time are the complex phases ψ' and ψ''. Hence, evaluating the ensemble average, if we assume ergodicity, becomes an effort in evaluating the average of the ψ's. We now change variables to those of Yura [Ref. 17] and Walters [Ref. 14],

$$\rho^+ = (\vec{r}'+\vec{r}'')/2 \ , \quad \vec{\rho}^- = \vec{r}'-\vec{r}'' \ , \quad \vec{r} = \vec{\rho} \quad .$$

With this change of variables, the Fresnel approximation becomes

$$(|\vec{r}-\vec{r}'| - |\vec{r} - \vec{r}''|) = \frac{1}{z}(\vec{\rho}^{+} \cdot \vec{\rho}^{-} + \vec{\rho} \cdot \vec{\rho}^{-}) \quad , \quad (2.44)$$

where $z' = z'' = 0$. This gives a very physical result for the average intensity

$$\langle I(r) \rangle = \left(\frac{k}{2\pi z}\right)^2 \int d\vec{\rho}^{-} \; M_L(\vec{\rho}^{-}) M_S(\vec{\rho}^{-}, z) e^{\left(\frac{-ik\vec{\rho}\cdot\vec{\rho}^{-}}{z}\right)} \quad , \quad (2.45)$$

where

$$M_L(\vec{\rho}^{-}) = \int E(\vec{\rho}^{+} + \frac{\vec{\rho}^{-}}{2}) E^{*}(\vec{p}^{+} - \frac{\vec{\rho}^{-}}{2}) e^{\left(\frac{ik}{2}\vec{\rho}^{+}\cdot\vec{\rho}^{-}\right)} d^2\vec{\rho}^{+} \quad (2.46)$$

and

$$M_S(\vec{\rho}^{-}, z) = \langle e^{[\psi'(\vec{r}', \vec{r}) + \psi''(\vec{r}'', \vec{r})]} \rangle \quad . \quad (2.47)$$

Since $z >> r'$ or r'', the exponential in (2.46) can be approximated as unity. This makes M_L the autocovariance of the aperture (or if normalized, the aperture mutual coherence function (MCF)). M_S is the atmospheric mutual coherence function. This allows us to treat the propagation problem in two distinct parts; the effects of the atmosphere and the effects of the receiver optics.

The trick now is to find the atmospheric mutual coherence function. Yura assumes that the amplitude fluctuation, χ, and phase fluctuation, s, that compose ψ are Gaussian variables, which implies that $\exp(\psi'+\psi'')$ is log-

normally distributed. Using a property of log-normally distributed random variables and some results of Fried's work in [Ref. 19], Yura represents the atmospheric MCF in terms of the wave structure function $D(\rho)$, giving

$$\langle e^{(\psi'+\psi''^*)} \rangle = \exp(-D(\rho)/2) \quad , \tag{2.48}$$

where $D(\rho) = D_\chi(\rho) + D_s(\rho)$. Now we can apply the results of Tatarski's work, since we have forms for $F_\chi(K,0)$ and $F_s(K,0)$ which can be related back to their structure functions. From this, $D(\rho)$ becomes

$$D(\rho) = 3.44k^2 \ell_0^{-1/3} \rho^2 \int_0^L C_n^2(z)dz \; ; \; \rho < \rho_0 \tag{2.49}$$

and

$$D(\rho) = 2.91k^2 \rho^{5/3} \int_0^L C_n^2(z)\, dz \; ; \; \rho > \sqrt{\lambda L} \; , \tag{2.50}$$

where ℓ_0 is the inner scale and $\sqrt{\lambda L}$ is the Fresnel zone size. Based upon (2.49) and (2.50), Yura represents (2.48) as

$$\langle e^{(\psi'+\psi''^*)} \rangle = MCF(\rho) = \exp\left(\frac{-\rho}{\rho_0}\right)^{5/3} \quad , \tag{2.51}$$

where ρ_0 is the transverse distance for the MCF to decline by e^{-1}. Yura has developed forms for ρ_0 including inner and outer scale effects [Ref. 17]. We should remember that ρ_0 is a distance in the aperture of the optical system. It is nominally on the order of a few centimeters during the day.

4. The Modulation Transfer Function Approach

Fried in [Refs. 19, 20] uses the modulation transfer function (MTF) rather than the MCF. This application of the MTF and MCF are closely related since both represent the effects of the atmosphere in different planes (i.e., aperture and image planes). The MTF is the modulus of the complex optical transfer function from the linear systems approach to optics. This points to the fundamental difference between Fried and Yura's approach. Fried's work is done in the coordinates of the image plane, i.e., spatial frequencies, while Yura works in the aperture. Both are equivalent by the Wiener-Khintchine theorem since a lens produces the Fourier transform of the incident electric field in the image plane. The transformation between the two planes is

$$\rho \rightarrow \lambda R K \quad ,$$

where R is the focal length of the optics and K is the spatial frequency of the scintillations. This allows us to move between the aperture and image planes. Thus, the MTF(K) is

$$MTF(K) = \exp[-3.44^{(\lambda RK/r_0)^{5/3}}] \quad , \tag{2.52}$$

where r_0 is the 1/e distance of the MTF and is given by

$$r_0^{-5/3} = (\frac{2.905}{6.88})\ k^2\ \sec(\phi) \int_0^{\infty} dz C_n^2(z) \quad , \tag{2.53}$$

where ϕ is the zenith angle [Ref. 21].

Explicitly in the MTF and implied in the MCF is a low pass filtering of the scintillation spatial frequencies by the atmosphere and optics. This linear systems view is extremely powerful. It allows us to decompose the turbulent propagation problem into a product of atmospheric and optical system filtering functions. We will use this idea and the Wiener-Khintchine theorem later to our advantage.

5. Measures of Spatial Coherence

As mentioned in the introduction, ρ_0 and r_0 represent two measures of the atmosphere's ability to maintain the spatial coherence of a propagating wave. Nominal values for r_0 are approximately 3-10 cm for ground to space measurements. From (2.53), we see that turbulence close to the aperture of an optical system contributes most to r_0 since C_n^2 is largest in the boundary layer [Ref. 2].

Fried in [Ref. 21] derives the theoretical equation for another measure of spatial coherence in the atmosphere.

This is the isoplanatic angle, θ_0. Isoplanatism is the dependence of the optical transfer function of a system on the position of the source. Since, Yura and Fried's approaches break the propagation problem into MCF's and MTF's for the atmosphere and optics, the atmospheric turbulence does not affect the OTF of the optical system. It affects the OTF of the atmospheric part, hence the term anisoplanatism. This means the atmospheric OTF is dependent on the particular propagation path through the turbulence.

The isoplanatic angle is an angular measure of spatial coherence. If we consider two paths through turbulence in the atmosphere, the isoplanatic angle relates the mutual coherence e^{-1} point between the two paths. Fried defines the function $S(\vec{r},\vec{\theta})$ given by

$$S(\vec{r},\vec{\theta}) = 2.905\, k^2 \int_{\text{path}} dv C_n^2 \left(\left| r\left[1-\left(\frac{v}{L}\right)\right] \right|^{5/3} + [\theta v]^{5/3} \right.$$

$$\left. - \frac{1}{2}\left| \{ r\left[1-\left(\frac{v}{L}\right)\right] \}^2 + 2r\theta\left[1-\left(\frac{v}{L}\right)\right] vc + \{\theta v\}^2 \right|^{5/6} - \frac{1}{2}\left| \{ r\left[1-\left(\frac{v}{L}\right)\right] \}^2 \right.\right.$$

$$\left.\left. - 2r\theta\left[1-\left(\frac{v}{L}\right)\right] vc + \{\theta v\}^2 \right|^{5/6} \right) , \qquad (2.54)$$

where L is the path length, v is a position along the path and c is the cosine of the angle between r and θ. In the limit as $r/\theta \to \infty$ (or two rays crossing at infinity),

$$\lim_{r/\theta \to \infty} S(\vec{r},\vec{\theta}) = 2.905\, k^2 \int_{\text{path}} dv C_n^2 (\theta v)^{5/3} \quad . \tag{2.55}$$

Fried defines θ_0 as

$$\theta_0^{-5/3} = 2.905\, k^2 \int_{\text{path}} dv C_n^2\, v^{5/3} \quad . \tag{2.56}$$

Interestingly, r_0 is given by the other limit of the function $S(\vec{r},\vec{\theta})$,

$$\lim_{r/\theta \to 0} S(\vec{r},\vec{\theta}) = 2.905\, k^2 \int_{\text{path}} dv C_n^2 \{r[1 - (\tfrac{V}{L})]\}^{5/3} \tag{2.57}$$

where

$$r_0^{-5/3} = (\tfrac{2.905}{6.88})\, k^2 \int_{\text{path}} dv C_n^2 [1 - (\tfrac{V}{L})]^{5/3} \tag{2.58}$$

and the $(1 - V/L)^{5/3}$ term is a spherical wave weighting function. Clearly, we can change variables from v to z by correcting for zenith dependencies, i.e.,

$$v \to z \sec \phi \quad ,$$

where ϕ is the zenith angle. Now one can immediately see the relationship between r_0 and θ_0. The isoplanatic angle measurement looking up is the same as the r_0 or MTF measurement looking down from space.

Walters has shown θ_0 relates back to ρ_0 and the Huygens-Fresnel picture. The relationship is given by

$$\theta_0 = \rho_0/L \quad . \tag{2.59}$$

Using the Huygens-Fresnel picture, one can gain a physical insight into r_0 and θ_0 measurements. Consider a source on the earth propagating spherical waves into space. θ_0 is the angle such that the MCF of the field at two different points on the wavefront is e^{-1} its original value. This picture can be reversed where two points in space emit spherical waves that sum at a point on the earth. This gives the corresponding r_0 measurement. One of the advantages to the Huygens-Fresnel approach is this reciprocity.

Based upon the isoplanatic angle weighting function, turbulence between 8-15 km is weighted heavily. Hence, turbulence near the tropopause tends to make the isoplanatic angle small (i.e., 3-5 μrad). Large isoplanatic angles are in the neighborhood of 13-20 μrad. The largest isoplanatic angles (20 μrad) are very small, consequently adaptive optics concepts that compensate for the atmosphere have a monumental task since the correction is only good for an angle θ_0.

6. Intensity Fluctuations

Tatarski in [Ref. 6] obtains the variance of the intensity fluctuations from

$$\sigma^2 = B_\chi(0) \quad , \tag{2.60}$$

where $B_\chi(0)$ is the covariance function at $\rho = 0$. He evaluates the integral over K in $B_\chi(0)$ for point sources and point receivers giving results for plane and spherical waves. In reality, we do have point sources, stars. However, real point receivers do not exist. Fried [Ref. 22], obtains σ^2 for finite apertures. He finds that the aperture averaged variance is

$$\sigma^2 = \frac{2\pi}{\alpha(\frac{\pi D^2}{4})^2} \int_0^D \rho d\rho \; MTF(\rho) B_\chi(\rho) \quad , \tag{2.61}$$

where D is the diameter of the optics and α is a constant depending on the type of aperture. $B_\chi(\rho)$ can be represented by the two-dimensional Hankel transform of the spectrum because isotropy imposes cyclindrical symmetry. Substituting this into (2.61) gives

$$\sigma^2 = \frac{2\pi}{\alpha}(\frac{4}{\pi D^2})^2 \int_0^D \rho d\rho \; MTF(\rho)[2\pi \int_0^\infty J_0(K\rho) F_\chi(K,0) K dK]. \tag{2.62}$$

The ρ integration is trivial since we have the Hankel transform of an MTF or autocorrelation. This transform

yields the intensity spectrum for the finite aperture involved, I(K). Hence, the normalized variance is

$$\frac{\sigma_s^2}{S^2} = 2\pi \int_0^\infty KdKF_\chi(K,0)I(K) \quad , \tag{2.63}$$

where

$$S^2 = \alpha \left(\frac{\pi D^2}{4}\right)^2 I_0^2 \quad .$$

Again we see the filtering of spatial frequencies by the atmosphere in $F_\chi(K,0)$ and by the optics in I(K). Aperture averaging is the filtering done by the optical system. Equation (2.63) has limits for point apertures and infinite apertures. In [Ref. 6], Tatarski shows that for point apertures, (2.63) behaves as $z^{5/6}$, while for infinite apertures it behaves as z^2. This implies that all other apertures fall between these two z dependencies.

Over the years, research has modified and shown the limits of Fried's initial aperture averaging work [Ref. 22]. Yura [Ref. 24] suggests a form for the covariance function for arbitrary z. This modified Fried's results slightly. However, a more serious problem was found by Dunphy and Kerr [Ref. 25] and by Homstad, et. al [Ref. 26], if turbulence is very strong. Experimental work has failed to show the theoretical aperture averaging effects in strong turbulence.

The trend is towards less aperture averaging than expected in strong turbulence. Azar, et. al. [Ref. 27] and Clifford, et. al. [Ref. 28] explain that the covariance function for strong turbulence is governed by two transverse scale sizes. The short size determines the initial fast drop in the covariance function, while a second scale characterizes the long tail. The long tail of the covariance function reduces the effects of aperture averaging. The aperture averaging controversy will arise again when we look at isoplanometer data.

7. Problems in the Theory

The theory for wave propagation presented so far has been for weak turbulence or single scattering. We have neglected the effects of multiple scattering. When the path lengths are long or the turbulence is strong, the linear theory breaks down. Experiments show that for intensity variances of $\sigma^2 \approx .3$, the normalized variance saturates to 1 [Ref. 28]. Multiple scattering destroys the spatial coherence of the wave. The linear theory assumes a coherent wave incident on the perturber whose strength is dependent on C_n^2 (or the temperature gradient). If the spatial coherence is degraded such that it is less than the Fresnel zone size, $\sqrt{\lambda L}$, the wave is partially coherent across the perturber. This implies that interference can no longer completely modulate the wave. Hence, the variance of the

fluctuation intensity tends to saturate or approach a constant. Other theories have evolved to handle propagation in strong turbulence or multiple scattering. Many of the theories find their basis in techniques developed for quantum mechanics. Stroebehn in [Ref. 29] reviews iterative Green's function solutions that give an exact answer to the multiple scattering problem. But the solution, in practice, cannot be computed. He also summarizes the concept of Feynman diagrams originally developed for quantum electrodynamics, and other more sophisticated theories developed for strong turbulence.

III. REMOTE MEASUREMENTS OF THE ISOPLANATIC ANGLE

A. TECHNIQUE

Loos and Hogge [Ref. 23] extend Fried's work of [Ref. 22] by completing the Hankel transform of the MTF for a "top hat" aperture function. Loos and Hogge [Ref. 23] and Walters [Ref. 30] realized that by measuring the normalized variance of the intensity fluctuations of stars one could obtain the isoplanatic angle to within a constant. Walter's technique is as follows. The normalized variance of intensity fluctuations is

$$\frac{\sigma_s^2}{S^2} = 4(4\pi^2)(.033k^2) \int_0^L C_n^2(z)dz \int_0^\infty KdK\Phi(K)\sin^2(\frac{K^2z}{2k})I(K) \quad , \tag{3.1}$$

where K is the spatial frequency of the amplitude scintillations, L is the path length over which C_n^2 is non-zero, I(K) is the intensity spectrum of the receiver optics and $\Phi(K)$ is the $K^{-11/3}$ portion of the Kolmogorov spectrum for turbulence in the inertial subrange. The similarity to the isoplanatic angle given by

$$\theta_0^{-5/3} = 2.905\, k^2[\sec\phi]^{8/3} \int_0^L dzC_n^2(z)z^{5/3} \quad , \tag{3.2}$$

is obvious. The trick is to make the weighting function W(z),

$$W(z) = \int_0^\infty KdK\Phi(K)\sin^2(\frac{K^2z}{2k})I(K) \quad , \tag{3.3}$$

behave as $z^{5/3}$. Mathematically this means that

$$z^{5/3} \approx AW(z) \quad , \tag{3.4}$$

where A is a proportionality constant. Hence, the isoplanatic angle becomes

$$\theta_0^{-5/3} = A'(\frac{\sigma_s^2}{S^2}) \quad , \tag{3.5}$$

where A' is a new proportionality constant taking account the four's and Pi's, etc. of (3.1).

Previously we noted that the weighting function integral behaves as z^2 for infinite apertures and $z^{5/6}$ for point apertures [Ref. 6]. Luckily, the isoplanatic angle weighting function, $z^{5/3}$, lies within these two limits. Hence, theoretically it should be possible to mimic this behavior.

The power of this isoplanatic angle measurement technique is that no explicit knowledge of the C_n^2 profile is

required. C_n^2 in the free atmosphere is difficult to measure remotely with high vertical resolution (as we shall see later). Hence, integrated parameters like r_0 and θ_0 depending on C_n^2 are usually measured independent of a C_n^2 profile. Another important advantage that naturally evolves from this technique is the filtering done by the aperture averaging. The averaging aids in suppressing the high spatial frequency scintillations that are most affected by passage through the atmosphere and are most liable to cause saturation.

B. THE FIRST ISOPLANOMETERS

Walters developed the first isoplanometers to operate during the day and night [Ref. 30]. The optical receiver is an Celestron 14 Schmidt-Cassegrain telescope obscured so that a 11 cm diameter clear aperture remains. The theory at the time of instrument development was based on a "top hat" aperture function. Walters found that the 11 cm aperture gave a good approximation to the $z^{5/3}$ weighting function.

Since these instruments are designed to operate at both day and night, they have a very small field of view to suppress the Rayleigh scattered background encountered in daytime viewing. Hence, high quality telescope drives and mounts are required for accurate tracking. In short, the first three generations of isoplanometers require full-time support. In [Ref. 30], Walters shows that these instruments operate properly within the weak turbulence limits.

C. APERTURE APODIZATION FOR WEIGHTING FUNCTION IMPROVEMENT

1. Weighting Functions for the Top Hat Aperture

One can compute numerically the integral over K in (3.3) giving the theoretical weighting function for a certain I(K). In reality, the limits to the K integral are not zero and infinity. The spatial frequencies of the scintillations are truncated by the inner and outer scales of turbulence. Hence, the upper and lower limits of integration become

$$K_{max} = \frac{2\pi}{\ell_0}$$

and

$$K_{min} = \frac{2\pi}{L_0} \quad ,$$

where ℓ_0 is the inner scale and L_0 is the outer scale. For the following computer simulations, ℓ_0 = 5 mm and L_0 = 10 m. The integration over K is done by a brute force application of Simpson's rule over 512 points for a given value of z. The z stepsize is log (Δz) = .05.

Figure 3.1 shows the error from $z^{5/3}$ for a 10 cm top hat aperture as a function of z for a 500 nm electromagnetic wave. I(K) for the 10 cm top hat is the Airy pattern,

$$I(K) = \left[\frac{2J_1(\frac{KD}{2})}{(\frac{KD}{2})}\right]^2 \quad , \qquad (3.6)$$

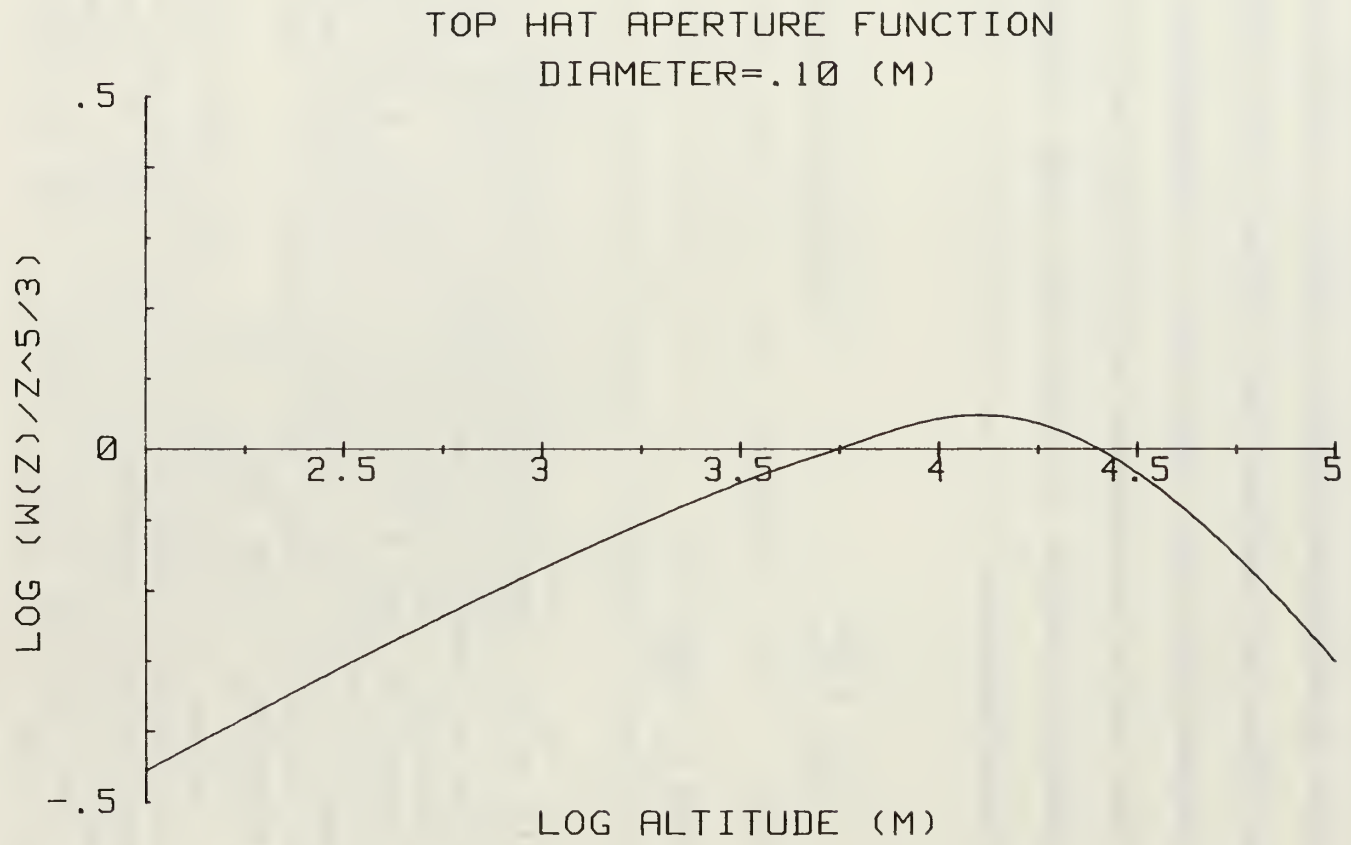

Figure 3.1 Error from $z^{5/3}$ for a Top Hat Aperture

where D is the diameter of the receiver optics. The curve in Figure 3.1 is normalized so that the integrated error between 2 and 20 km is zero. This ensures that the error is not consistently above or below $z^{5/3}$ giving erroneous results when this weighting function is integrated into a measurement system. The normalization interval 2 to 20 km results from the fact that turbulence, hence C_n^2, is large enough in that region to contribute to the isoplanatic angle integral given the $z^{5/3}$ dependence. Clearly, C_n^2 is largest in the boundary layer [Ref. 2], however the weighting is very small there causing little change in the isoplanatic angle. Actual profiles of C_n^2, like that provided by Dr. E. Good from the Air Force Geophysics Laboratory, Hanscom AFB, MA in Figure 3.2, bear out this assumption. The particular profile shown will be used extensively in Chapters IV and VIII of this dissertation. A more complete description of the profile will be provided at that time.

In [Ref. 24], Loos and Hogge plot the two theoretical limits for point and infinite apertures as a function of z. They also plot the aperture averaged weighting function for a 35 cm telescope. They note that the large aperture is on the z^2 side of $z^{5/3}$. In Figure 3.1 we see two different slopes present. If $W(z) = z^2$, the slope would be +1/3, while if $W(z) = z^{5/6}$, the slope would be -5/6. At low z, the slope in Figure 3.1 is 0.26, while

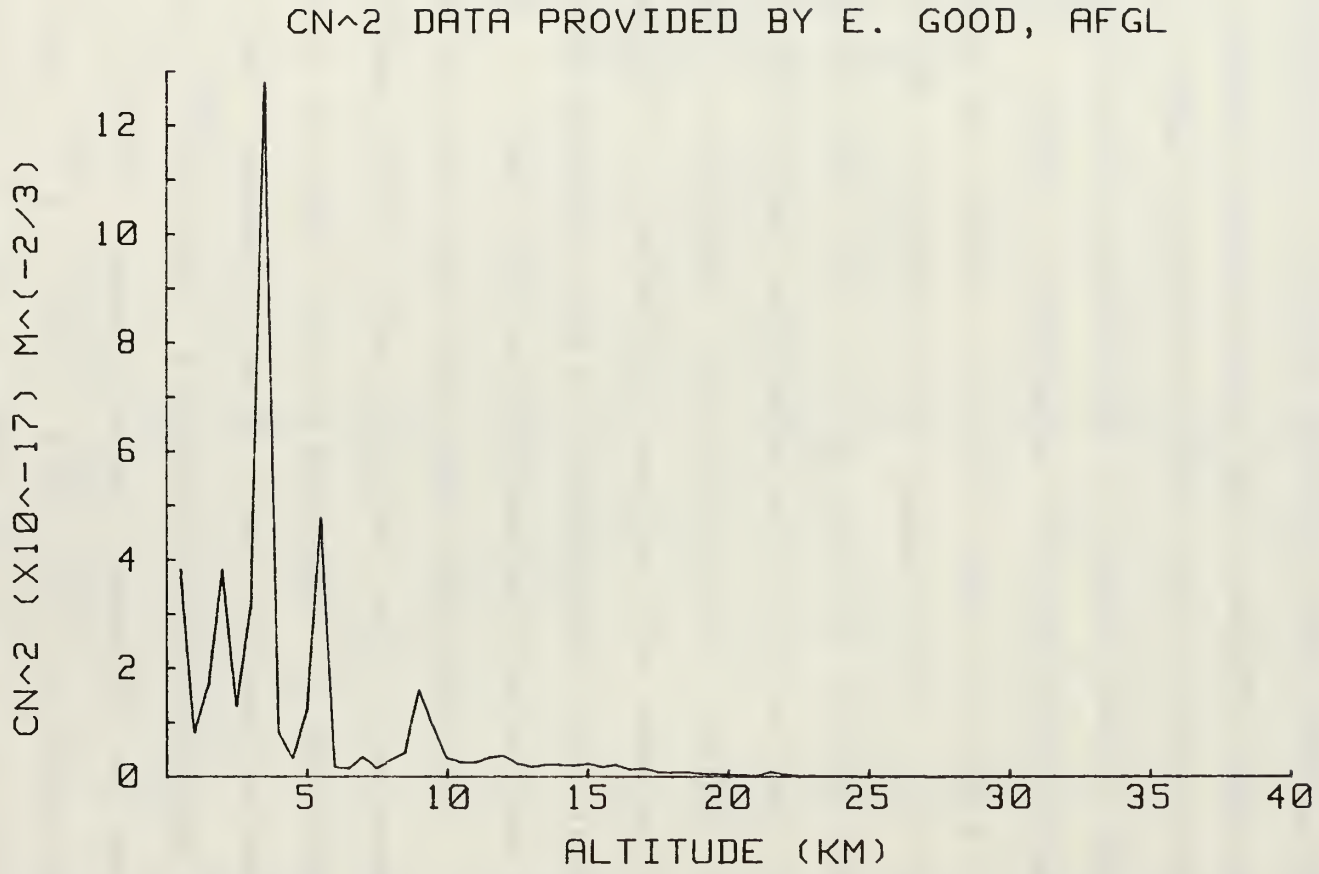

Figure 3.2 Balloon Data Provided by Dr. E. Good at the Air Force Geophysics Laboratory

at high z the slope is -0.63. As the diameter gets larger the slope of the low z portion moves closer to 1/3. Clearly, these figures only show the general influence of the limits. Figure 3.3 shows the movement of the peak towards higher z with increasing aperture size. Thus, we see more z^2 behavior as expected.

The question arises as to why, with increasing aperture size, one sees more z^2 behavior. The answer is straightforward. From [Ref. 23], we see that as D, the diameter of the optics goes to infinity, $I(K) = \delta(K-0)$. As finite D increases, the width of the Airy disk narrows due to the Hankel transform. Eventually, the Airy disk becomes a good approximation to the δ-function, hence, the z^2 behavior.

Figure 3.4 shows the wavelength dependence of the weighting function. To first order, the normalized variance given by (3.1) is wavelength independent. This can be shown by expanding $\sin^2(K^2z/2k)$ in a Maclaurin series giving

$$f(z) = \sin^2\left(\frac{K^2z}{2k}\right) \approx \left(\frac{K^4z^2}{4k^2}\right) + \ldots \qquad (3.7)$$

The k^2 cancel in (3.1) removing the wavelength dependence. We also see from (3.7) how the z^2 weighting function mentioned above comes about. The weighting function, (3.3),

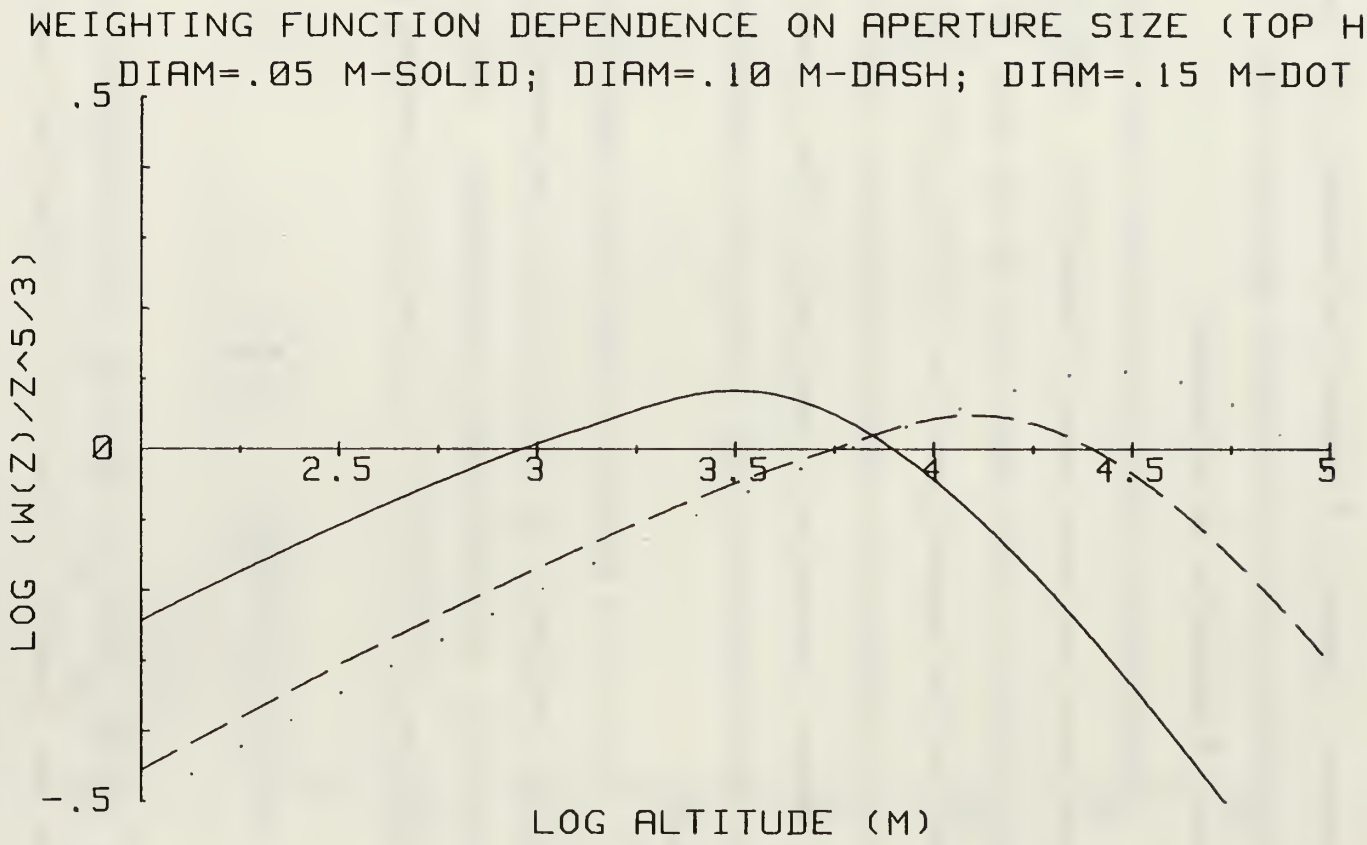

Figure 3.3 Error from $z^{5/3}$ for Varying Top Hat Aperture Sizes

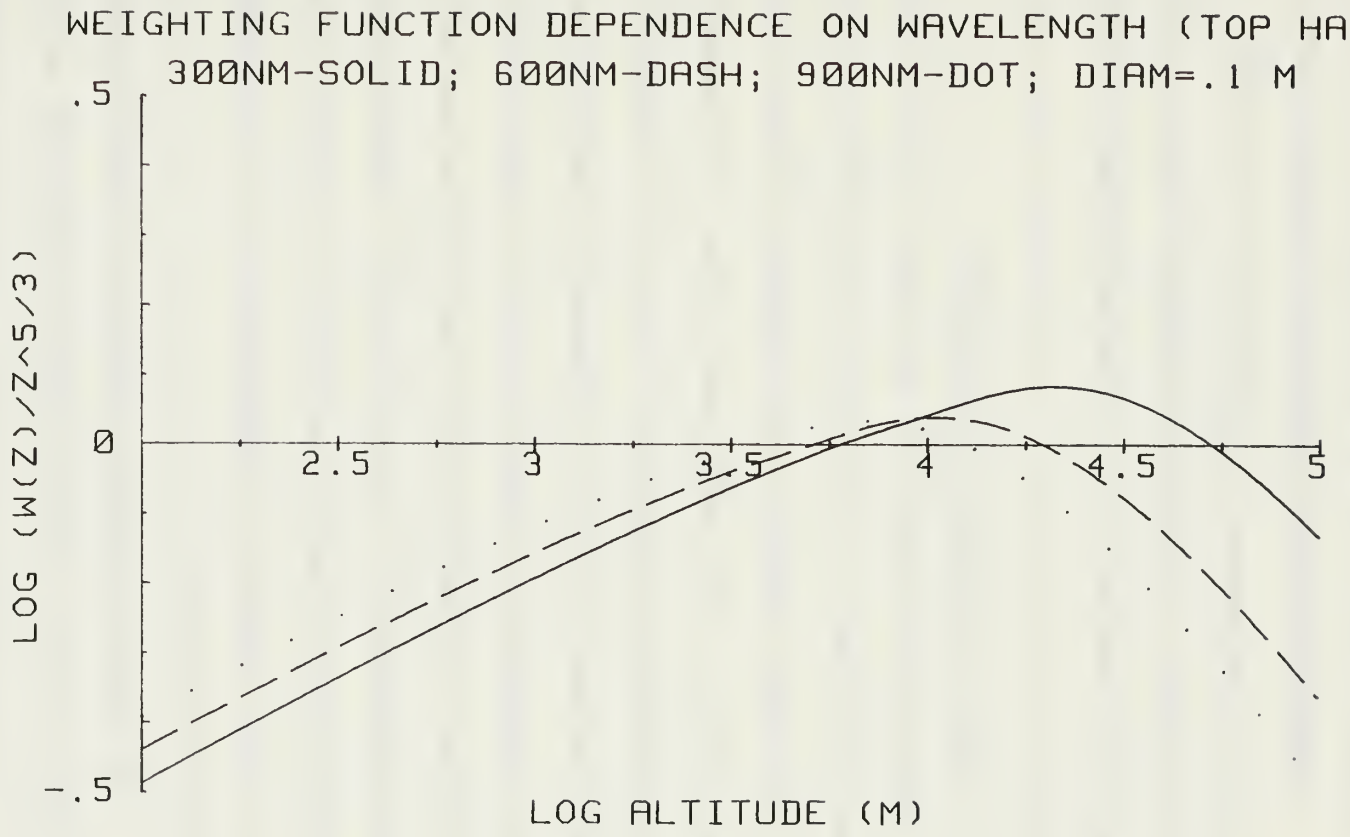

Figure 3.4 Wavelength Dependence of the Error from $z^{5/3}$ for the Top Hat Aperture

is itself not wavelength independent, hence we see the behavior persent in Figure 3.4. As the wavelength increases the weighting function moves laterally towards lower z.

The calibration constant, A', from (3.5), for the 10 cm top hat aperture is nominally 1.0×10^{10}. We would expect that this constant should get larger as more aperture averaging is included since the normalized variance will decrease.

2. Improved Weighting Functions

The error from $z^{5/3}$ in Figure 3.1 at 100 m is about a factor of three. In the weighting function given by (3.3), the only variable that depends on the measurement system is I(K). The remainder is due to the amplitude fluctuation spectra $F_\chi(K,0)$. For some time, different groups have been modifying telescope apertures or image planes to measure C_n^2 profiles [Refs. 31, 32, 33]. The modification of aperture functions by masks, etc., is called aperture apodization. Since the $z^{5/3}$ weighting function lies between the theoretical limits, we hope that through aperture apodization we might improve the isoplanometer weighting function.

To obtain intensity spectra from different aperture functions, one can Hankel transform the MTF or autocorrelation of the aperture or Hankel transform the aperture function and square the resultant amplitude spectra. The

results are equivalent by the Wiener-Khintchine theorem. Bateman [Ref. 34] compiled many different Hankel transform pairs. Using this list and different combinations of Bessel functions, I began constructing different weighting functions. Appendix A is a synopsis of the some apertures, spectra and resultant weighting functions. We found that combinations of Bessel functions are most desirable for spectra, since they represent apertures that can be implemented easily on a telescope.

Before moving on to the aperture function that approximates the $z^{5/3}$ quite well, it is interesting to look at the error from $z^{5/3}$ produced by a simple annulus aperture. Figure 3.5 is an error plot for an annulus with a 10 cm outer diameter and a 4 cm obscuration diameter. The two peaks correspond to the influence of the inner (lower z peak) and outer (higher z peak) diameters of the two Bessel functions involved. This leads one to believe that by using combinations of Bessel functions the $z^{5/3}$ dependence could be mimicked. Figure 3.6 is the error for a Celestron C8 telescope aperture. It is interesting to note that the inner diameter affects the weighting function at high z, while the outer diameter affects performance at low z. We saw this before with the two theoretical limits of the weighting functions.

After some effort, an aperture function was identified for a 8" Schmidt-Cassegrain telescope that

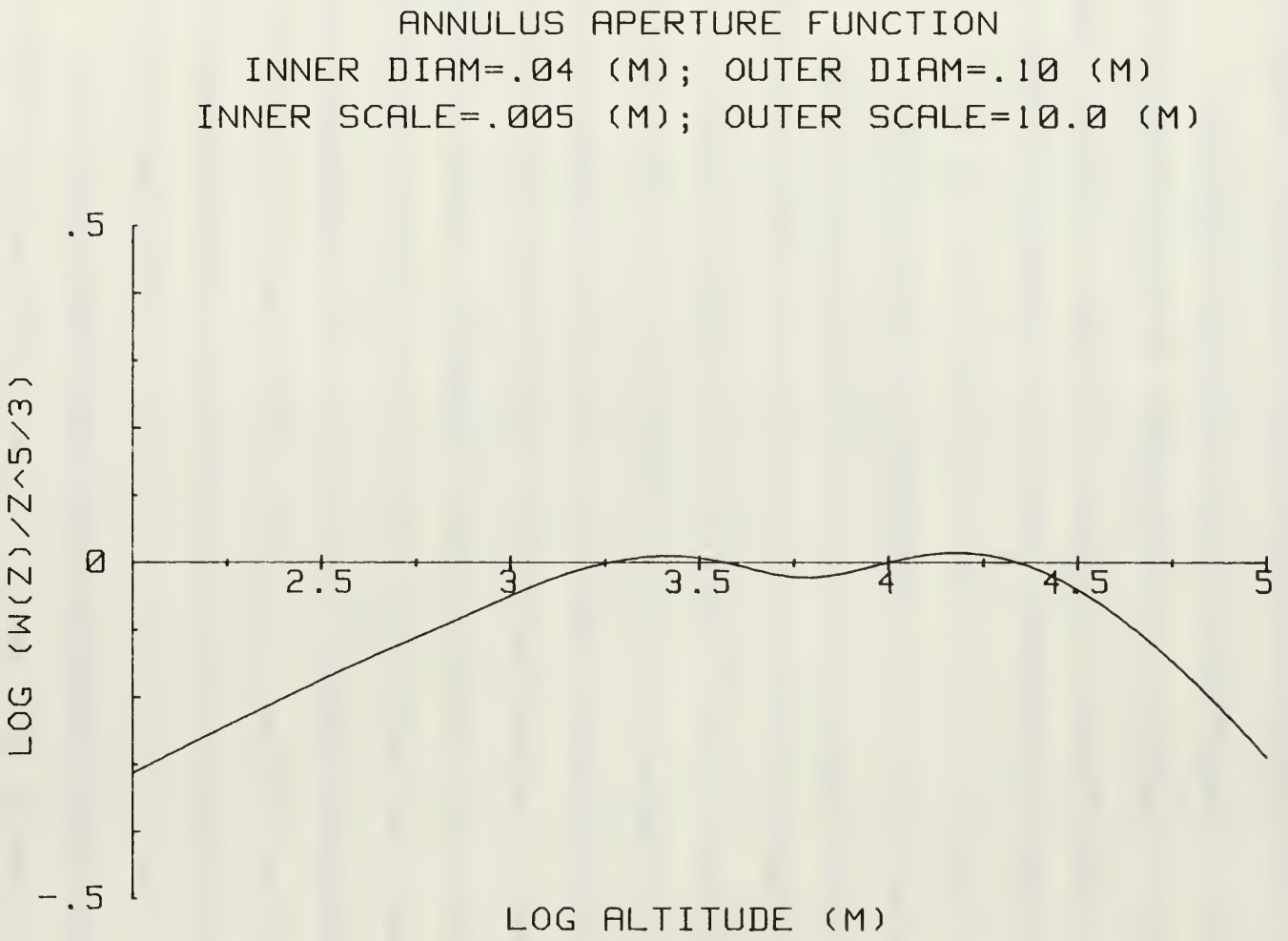

Figure 5.3 Error from $z^{5/3}$ for a Simple Annulus Aperture Function

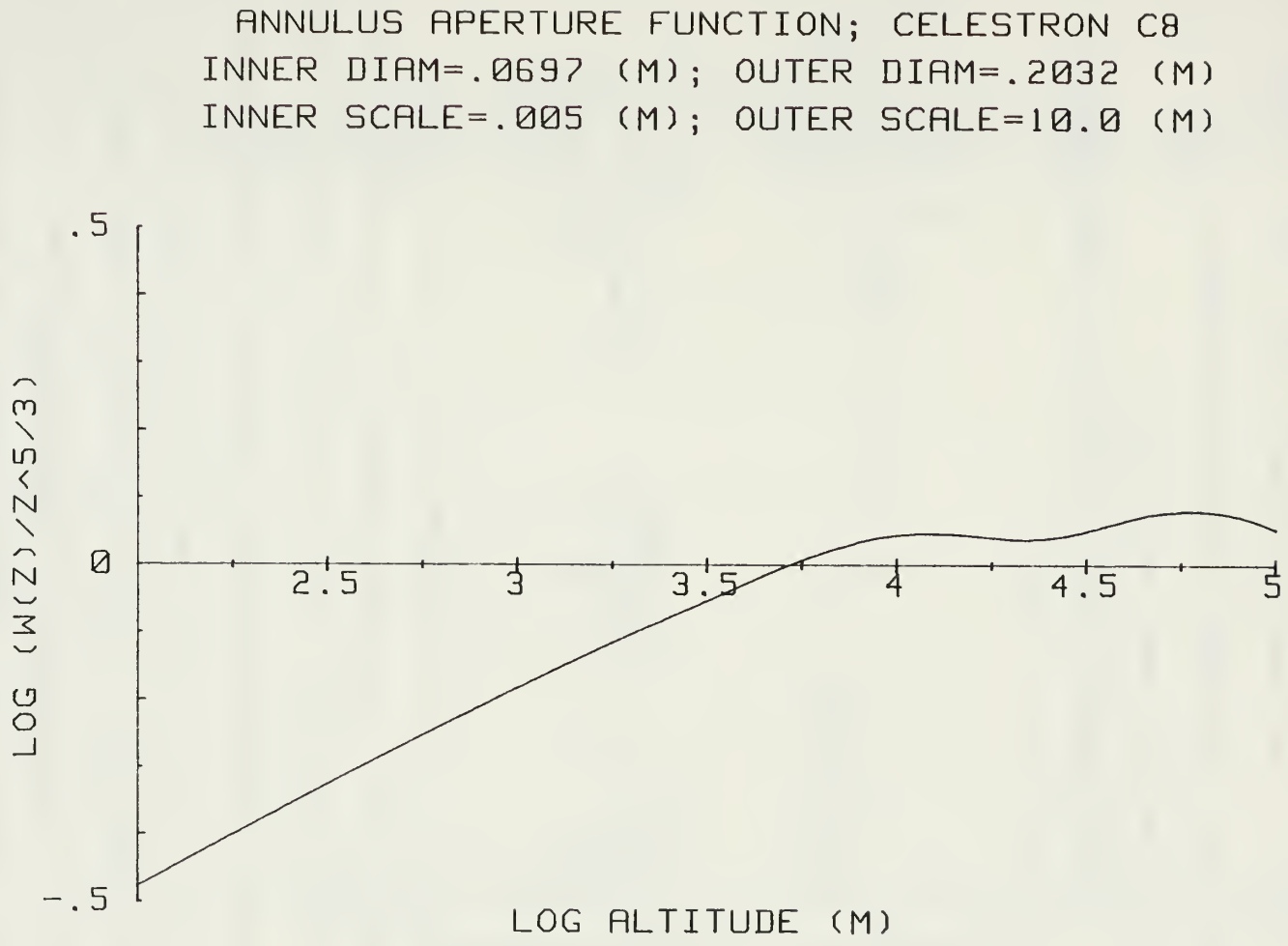

Figure 3.6 Error from $Z^{5/3}$ for the Celestron C8 Aperture

produces a weighting function that approximates the $z^{5/3}$ dependence. The aperture is the double annulus shown in Figure 3.7 producing the error from $z^{5/3}$ shown in Figure 3.8 for a 500 nm electromagnetic wave. Over the altitude range critical for isoplanatic angle measurements (2-20 km), this weighting function does very well.

The weighting function for the double annulus aperture function is given by

$$W(z) = \frac{1}{(1-\varepsilon_1^2+\varepsilon_2^2-\varepsilon_3^2)^2} \int_0^\infty K dK \Phi(K) \sin^2\left(\frac{K^2 z}{2k}\right) \left[\varepsilon_2^2 \left(\frac{2J_1\left(\frac{\varepsilon_2 KD}{2}\right)}{\frac{\varepsilon_2 KD}{2}} \right) - \varepsilon_1^2 \left(\frac{2J_1\left(\frac{e_1 KD}{2}\right)}{\frac{\varepsilon_1 KD}{2}} \right) + \left(\frac{2J_1\left(\frac{KD}{2}\right)}{\frac{KD}{2}} \right) - \varepsilon_3^2 \left(\frac{2J_1\left(\frac{\varepsilon_3 KD}{2}\right)}{\frac{\varepsilon_3 KD}{2}} \right) \right]^2 , \quad (3.8)$$

where ε_1, ε_2, ε_3 are constants that ratio the inner diameters to D, the outer diameter of the optics. $\Phi(K)$ is the $K^{-11/3}$ dependence of the Kolmogorov spectrum. Figure 3.9 shows a comparison of the amplitude spectra squared (intensity spectra) for the 20 cm double annulus and a 20 cm top hat aperture. It is interesting to note that the increased higher spatial frequencies present in the double annulus spectrum are responsible for the improvement in the weighting function.

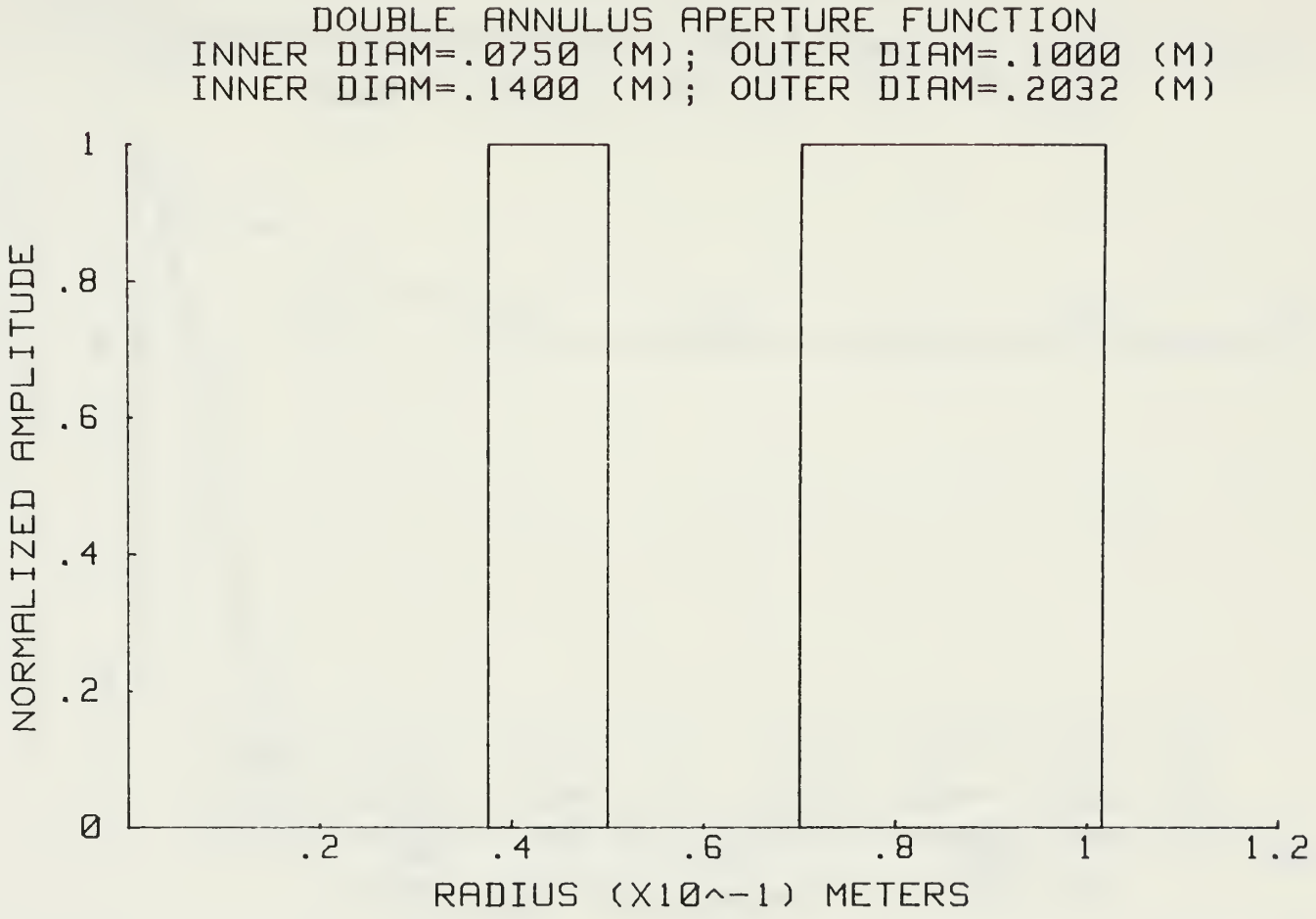

Figure 3.7 Double Annulus Aperture Function

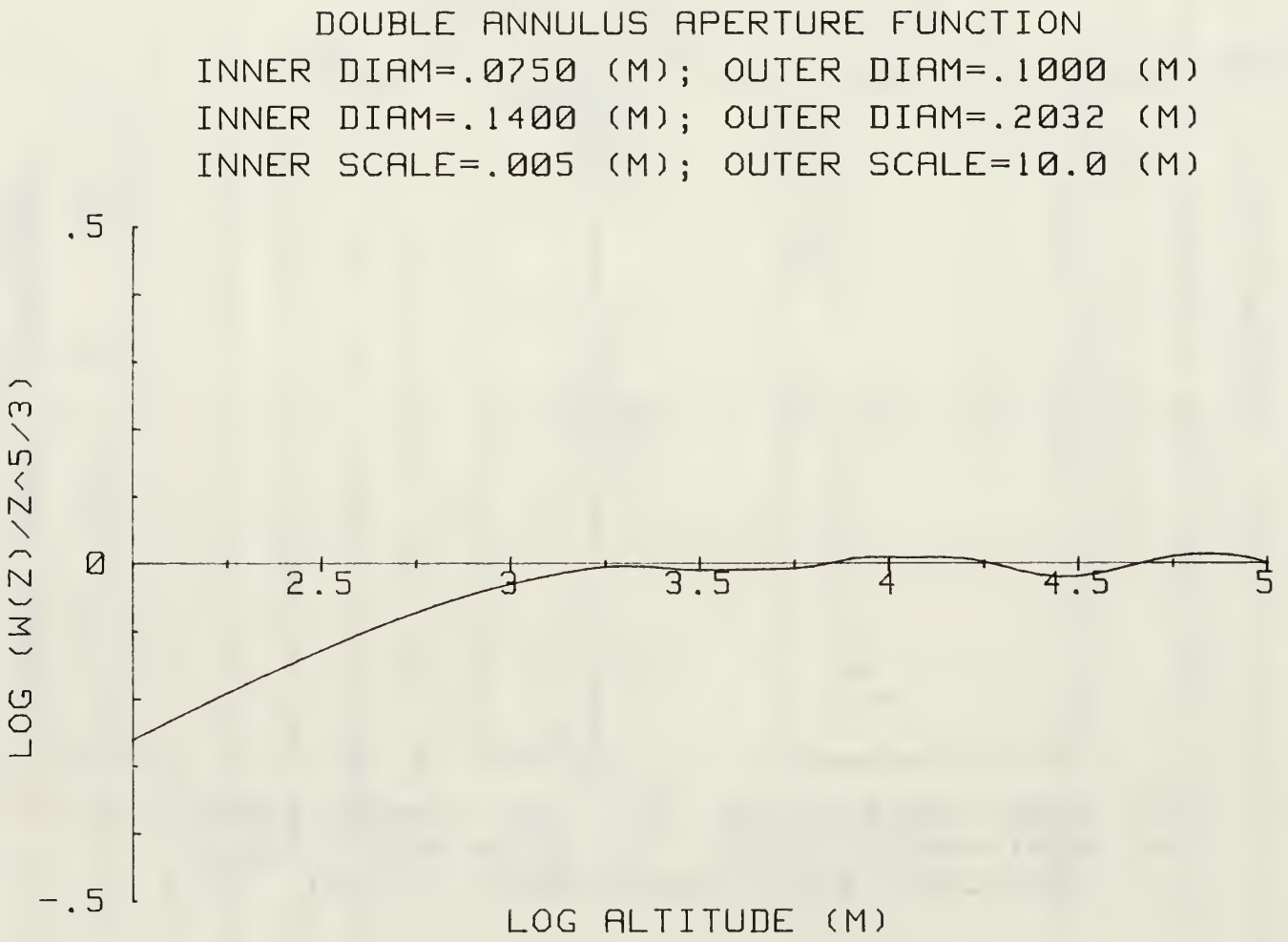

Figure 3.8 Error from $z^{5/3}$ for a Double Annulus Aperture Function

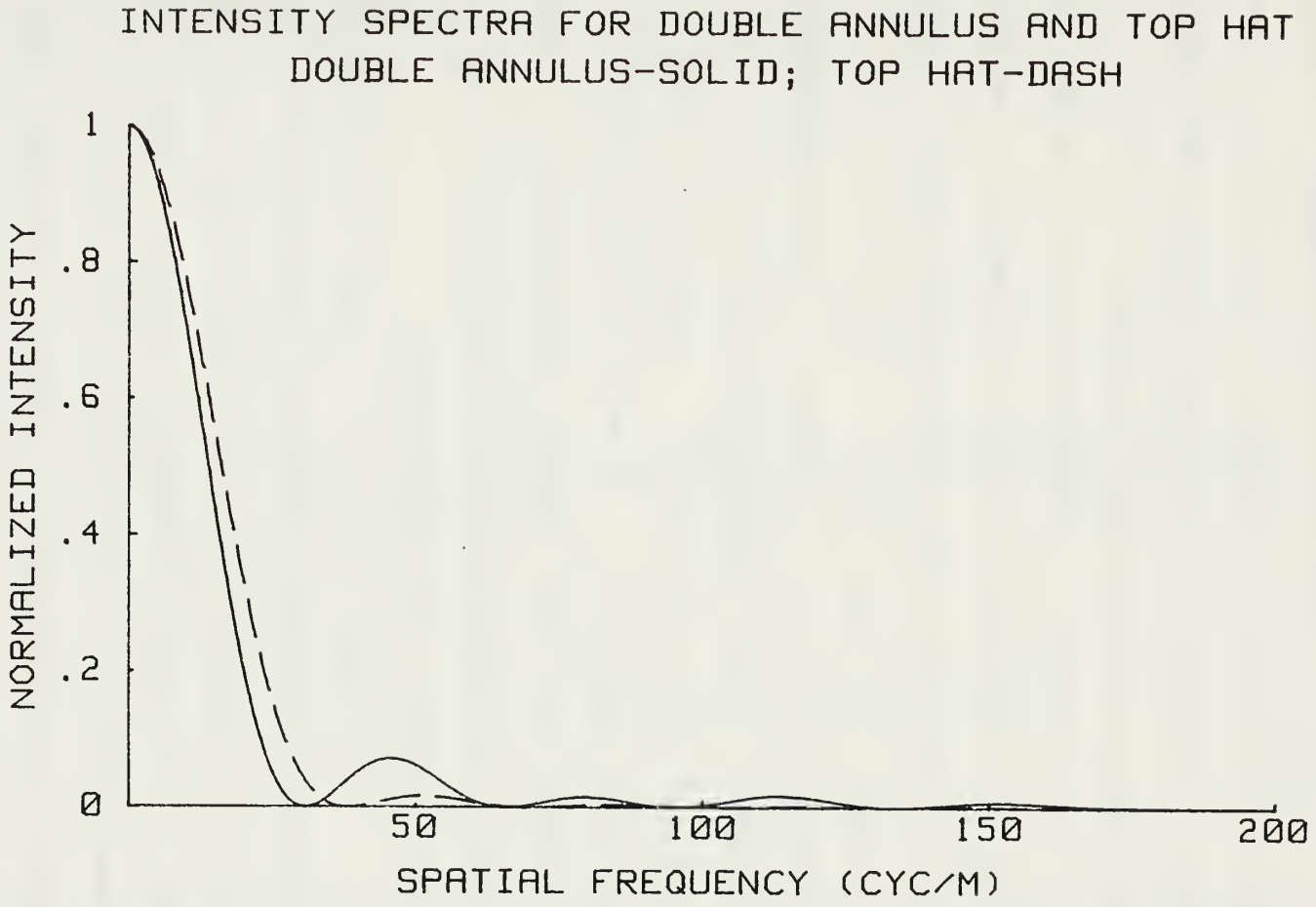

Figure 3.9 Comparison of 20 cm Double Annulus and 20 cm Top Hat Aperture Spectra

3. Double Annulus Calibration

The calibration constant, A', for the 20 cm double annulus aperture function is approximately a factor of four larger than the 10 cm top hat. This is due to the increased aperture averaging. The double annulus weighting function shows the same wavelength dependence as the top hat, Figure 3.10. An increase in the wavelength of the EM radiation shifts the weighting function to lower z. One interesting point is that the normalized variance has no wavelength dependence as we have shown. However, the isoplanatic angle certainly does (3.2). Clearly, all the wavelength dependence for the isoplanatic angle is in A' and it should behave, to first order as k^2. Figure 3.11 shows the A' wavelength dependence. At wavelengths greater than 800 nm, A' behaves as k^2 but diverges below 800 nm. Clearly, this is important depending on the temperature of the stars used for isoplanatic angle measurement.

Based upon the factor of four increase in the calibration constant, one might expect that an instrument with this weighting function would be able to withstand a factor of four more turbulent intensity before saturating. However, [Refs. 25, 26, 27] show that the aperture averaging effects may be degraded in strong turbulence making the 10 cm and 20 cm devices saturate at the same relative normalized variance. This issue will be resolved later by experiment.

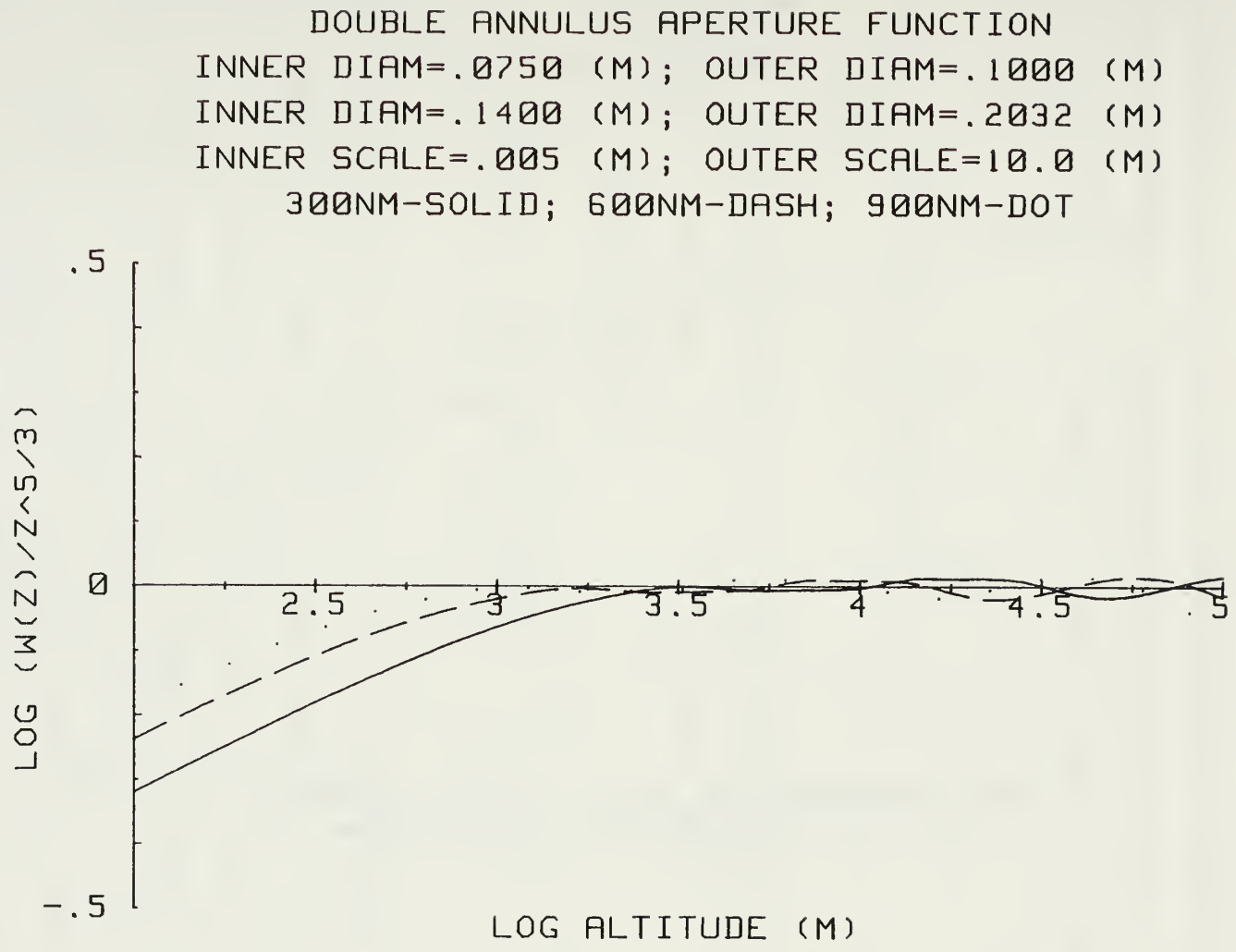

Figure 3.10 Wavelength Dependence of the Error from $z^{5/3}$ for a Double Annulus Aperture

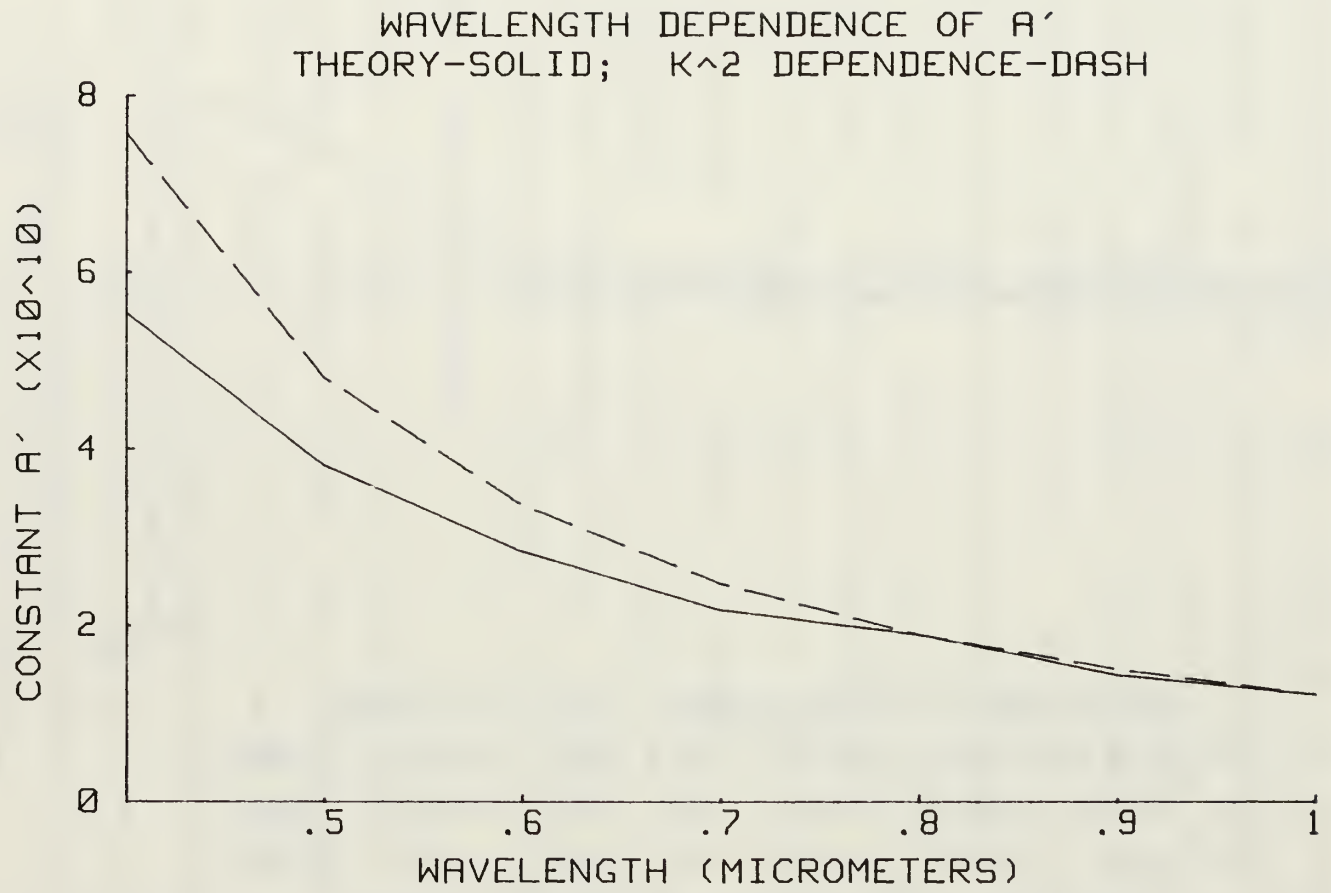

Figure 3.11 Wavelength Dependence of the Isoplanatic Angle Proportionality Constant A'

The 20 cm double annulus has approximately twice the area of the 10 cm top hat. This implies that the telescope will collect twice the photons increasing the average intensity by a factor of two. The variance of the shot noise current will also increase by a factor of two. Mathematically, the isoplanatic angle for the 10 cm system is

$$\theta_o^{-5/3} = A'_{10} \left[\frac{\sigma_s^2 + \sigma_n^2}{I^2} \right]$$

where σ_s^2 is the variance of the signal and σ_n^2 is the variance of the noise. For the 20 cm double annulus system, this same equation becomes

$$\theta_o^{-5/3} = 4A'_{10} \left[\frac{\sigma_s^2 + 2\sigma_n^2}{4I^2} \right] .$$

The proportionality constant, A', for the 20 cm system is approximately a factor of four larger than for the 10 cm system. In practice, we measure the shot noise experimentally and remove it from the variance in software. Hence, its effect is negligible at night. The 10 cm isoplanometer uses a pellicle to split the light beam in the detector subassembly. This reduces the average intensity by a factor of two. The 20 cm system, without the pellicle, is equivalent to the 10 cm system.

4. Double Annulus Improvements

The single greatest advantage the double annulus aperture function isoplanometer would have over the previous systems is that the 35 cm telescope is no longer required. This fact alone means saving approximately $8000.00 per system, not to mention that an isoplanometer based on an 8" telescope can be set up and operated by a single individual. The weighting function itself is a significant improvement over that of the top hat. We will see in the next chapter just what this improvement means in terms of isoplanatic angle measurement.

IV. APODIZED ISOPLANOMETER SENSITIVITY ANALYSIS

Two questions might be asked based on the double annulus weighting function of Figure 3.8. First, at 100 m there remains a factor of 1.75 error. C_n^2 at low altitudes is large, so deviations from $z^{5/3}$ may cause significant errors in the isoplanatic angle measurement. Second, in the numerical calculations of the weighting functions, a fixed inner scale was used for all z. Clearly, the inner scale is a function of altitude which may drastically change the weighting function. These two issues are addressed in this chapter.

A. WEIGHTING FUNCTION PERFORMANCE IN STRONG TURBULENCE

Consider an isoplanometer viewing a star directly through a convective plume. Clearly, the values of C_n^2 will be very large; on the order of 10^{-12} $m^{-2/3}$ near the ground. From Figure 3.8, one can immediately see that the weighting function for the double annulus has its greatest error in this region. Even though the $z^{5/3}$ weighting is low near the earth, the C_n^2 values in strong turbulence may be large enough to cause significant error in isoplanatic angle measurements. Based on this concern, I performed a sensitivity analysis on both the 10 cm top hat and double annulus aperture weighting functions.

1. The C_n^2 Profile

The most realistic way to test the weighting functions is to use real C_n^2 data. Figure 3.2 shows Good's C_n^2 data between 500 m and 40 km. Good obtained this profile by differential temperature measurement between two balloon-borne microthermal probes. From these differences one can construct the temperature structure function D_T and obtain C_n^2 as a function of z. C_n^2 and C_T^2 are related by the expression, [Ref. 6],

$$C_n^2 = C_T^2(79P/T^2 \times 10^{-6})^2, \tag{4.1}$$

where P is the pressure in millibars and T is the temperature in Kelvin. Direct measurement of C_n^2 in this manner yields very high vertical resolution, on the order of tens of meters. AFGL averaged raw data to give the 500 m resolution in Figure 3.2.

For purposes of this analysis, the region of greatest interest lies below 500 m. Walters [Ref. 2], plots C_n^2 versus altitude for 1 to 1000 m. Walters measured this particular data set at midday in a desert location and it represents very strong turbulence conditions. To account for convective plumes in low altitude turbulence, I doubled the Walters C_n^2 values. This gives one C_n^2 profile from 1 m to 40 km.

2. The Analysis

For convenience, I segmented the profile into four regions, 1 to 10 m, 10 to 100 m, 100 to 500 m, and 500 m to 40 km. Over each of these regions, I numerically evaluated three integrals,

$$\begin{aligned} \text{Theoretical} &= \int C_n^2(z) z^{5/3} dz \quad , \\ \text{Top Hat Aperture} &= \int C_n^2(z) W_{TH}(z) dz \quad , \\ \text{Double Annulus Aperture} &= \int C_n^2(z) W_{DA}(z) dz \quad . \end{aligned} \tag{4.2}$$

Based on Figures 3.1 and 3.8, we would expect the weighting function integrals to be smaller than theoretical at low z. Table 1 shows the results of this analysis. Table 2 contains the relative errors for each segment and the total path. The integrated values in Table 1 show that even the strongest turbulence at low z accounts for only a small percentage (about 2%) of the integrated path effect. Clearly, the errors over the total path for both the top hat aperture and the double annulus are within the limits of the theory. As one might expect, this analysis is extremely sensitive to the choice of A, a proportionality constant, where

$$z^{5/3} \approx AW(z) \quad . \tag{4.3}$$

TABLE 1

CONTRIBUTIONS TO THE ISOPLANATIC ANGLE INTEGRAL FOR STRONG TURBULENCE ANALYSIS

	Theoretical	Top Hat	Double Annulus
1-10 m	2.61×10^{-11}	3.44×10^{-12}	5.80×10^{-12}
10-100 m	8.19×10^{-10}	2.28×10^{-10}	3.77×10^{-10}
100-500 m	1.18×10^{-8}	5.50×10^{-8}	8.67×10^{-9}
500 m-40 km	3.89×10^{-7}	3.88×10^{-7}	3.91×10^{-7}

TABLE 2

RELATIVE ERROR FROM THEORETICAL FOR STRONG TURBULENCE ANALYSIS

	Top Hat	Double Annulus
1-10 m	.87	.78
10-100 m	.72	.54
100-500 m	.69	.26
500 m-40 km	7×10^{-4}	6×10^{-3}
1 m-40 km	.02	3×10^{-3}

In building an isoplanometer, the better one can define A or A', the better the instrument should operate.

This analysis shows that an isoplanometer should perform well, based on its weighting function in strong turbulence. However, we must note that in very strong turbulence, saturation has already reduced the reliability of the isoplanatic angle measurements.

B. INNER SCALE EFFECTS

The inner scale, η, is given by

$$\eta = \left(\frac{\nu^3}{\varepsilon}\right)^{1/4} , \qquad (4.4)$$

where ν is the kinematic viscosity and ε is the energy dissipation rate. Clearly, the kinematic viscosity and the dissipation rate are both functions of altitude. In completing the weighting function integral (3.3) numerically, I used the same inner scale for all values of z. This could mean that the weighting function does not accurately model the $z^{5/3}$ behavior required for isoplanatic angle measurement.

1. Constructing the Inner Scale as a Function of Altitude

From (4.4), we see that the inner scale depends strongly on the kinematic viscosity ν, given by

$$\nu = \frac{\theta}{\rho} ,$$

where θ is the viscosity coefficient and ρ is mass density. The U.S. Standard Atmosphere [Ref. 35] has vertical profiles of the kinematic viscosity. Hence, this portion of the inner scale is well understood.

The dissipation rate is another story entirely. Turbulence in the free atmosphere is intermittent, temporally and spatially, unlike boundary layer turbulence. This is compounded by the fact that measurements in the free atmosphere are difficult to make. Using [Refs. 36-41], I constructed what might be called a "nominal" dissipation rate profile. This profile, by no means, represents the output of any theoretical model on my part. It is a synopsis of the data and model results given in [Refs. 36-41]. The "nominal" dissipation rate profile is shown in Figure 4.1. Some controversy exists as to the behavior of the dissipation rate at higher altitudes [Ref. 38]. It is generally agreed that ε can reach values comparable to that observed in the surface layer. My profile shows light-moderate turbulence near the surface, $\varepsilon = 40$ cm^2/sec^3 (or $\log \varepsilon = 1.6$) at 100 m and decreases to .38 cm^2/sec^3 (or $\log \varepsilon = -0.42$) at 55 km. As a point of reference, we might note that the dissipation rates in convective storms are on the order of 10^3-10^4 cm^2/sec^3 [Ref. 40]. The units on

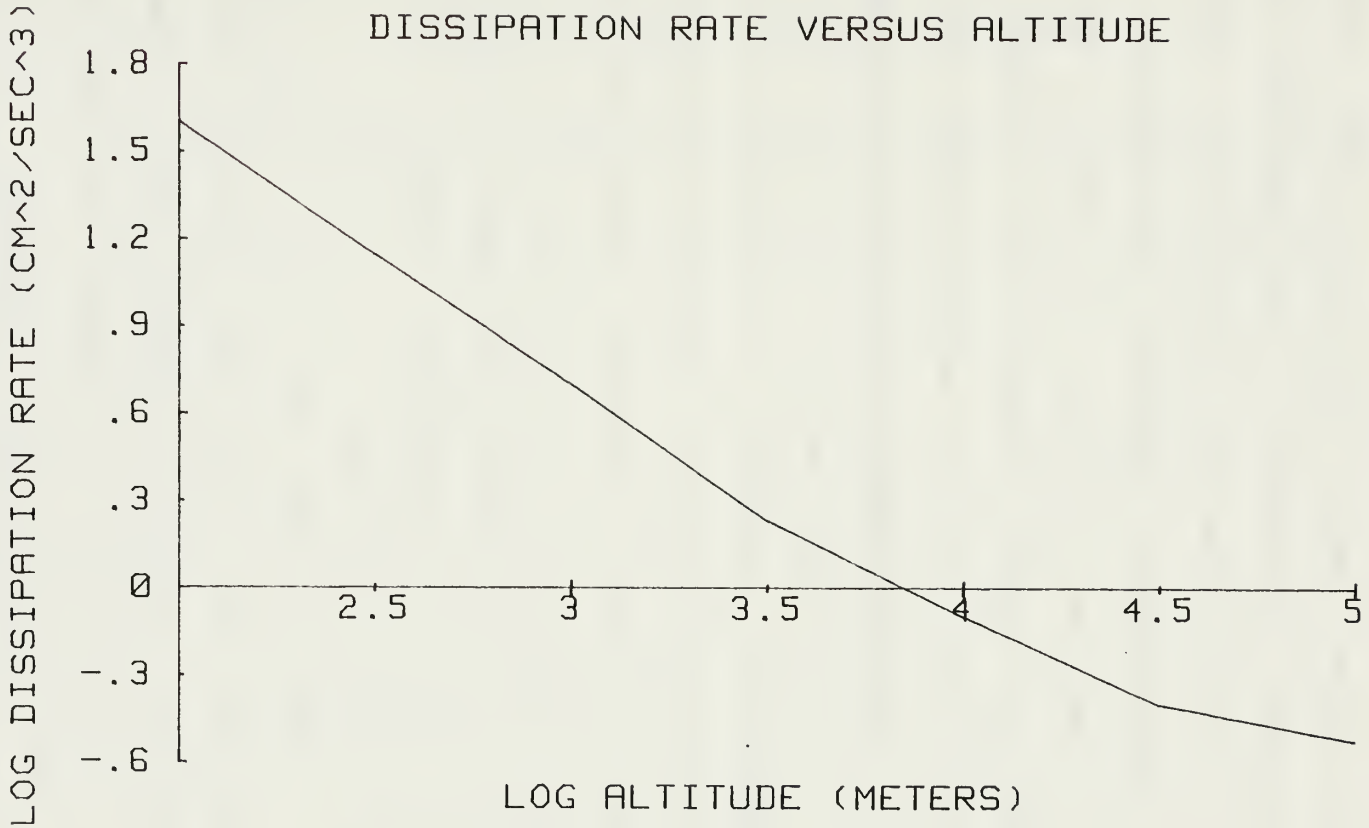

Figure 4.1 Dissipation Rate as a Function of Altitude

dissipation rate indicate a "specific" dissipation rate where system mass is removed.

Based on the Standard Atmosphere kinematic viscosity profile and my "nominal" dissipation rate profile, one can now construct the behavior of the inner scale with altitude. Figure 4.2 shows the inner scale profile. Clearly, the inner scale changes dramatically with altitude. At 55 km, η is on the order of a meter. As expected, the inner scale follows the kinematic viscosity since kinematic viscosity increases three orders of magnitude between 100 m to 50 km.

2. Weighting Function Dependence on the Inner Scale

A crude approximation to the inner scale effect can be obtained by increasing the inner scale for all z while numerically evaluating the weighting function integral. Figure 4.3a shows how the double annulus aperture weighting function changes with an inner scale of 10 cm. The deviation in W(z) caused by the change in inner scale from 5 mm to 10 cm is not catastrophic, however, a more complete analysis needs to be done.

Since the upper limit of the K integration depends on the inner scale, we see that increasing inner scale size corresponds to lowering the upper limit of integration. We expect that W(z) will not change significantly at lower z, due to the modest increase in the inner scale. However, as the inner scale increases, the upper limit of integration

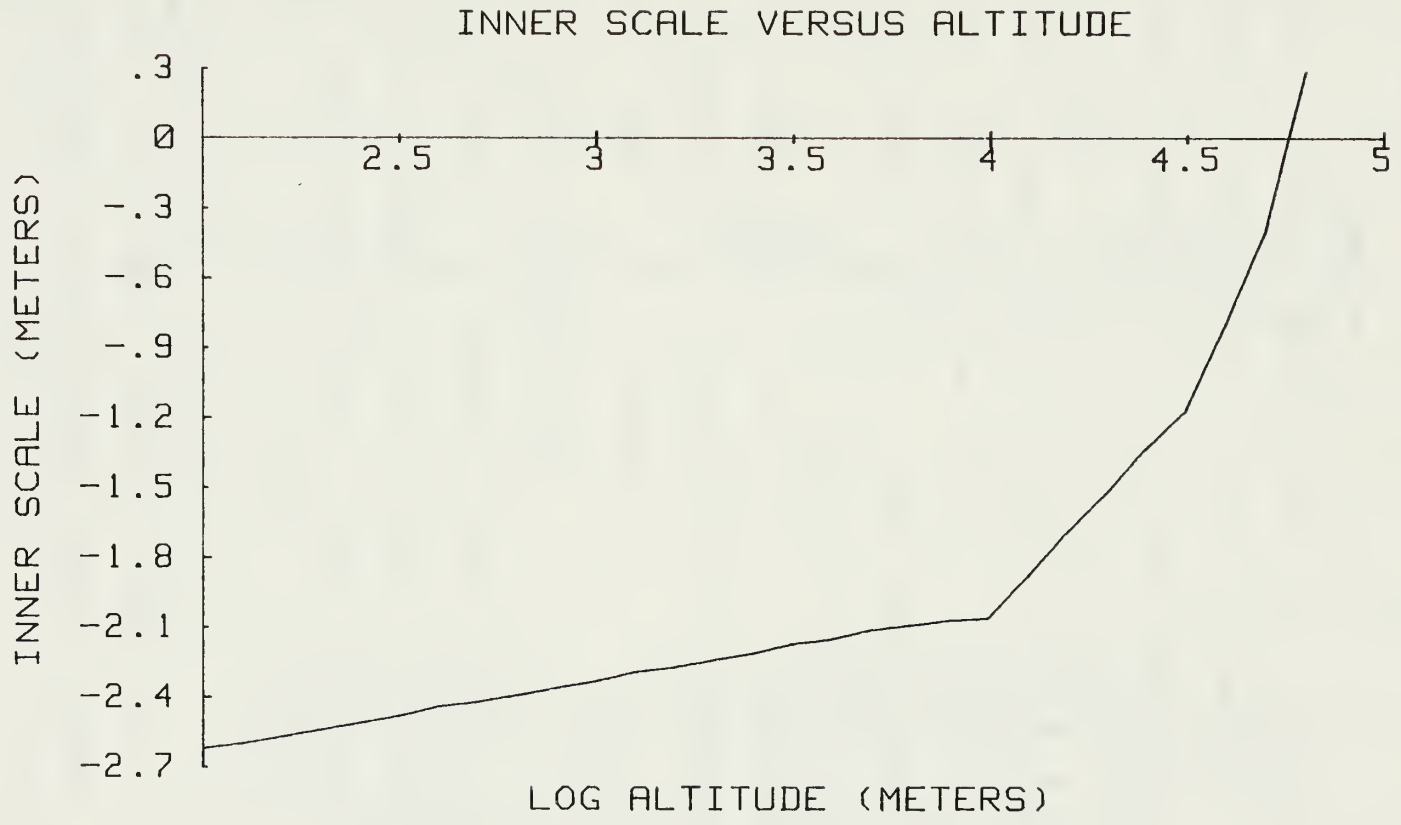

Figure 4.2 Inner Scale Change with Altitude

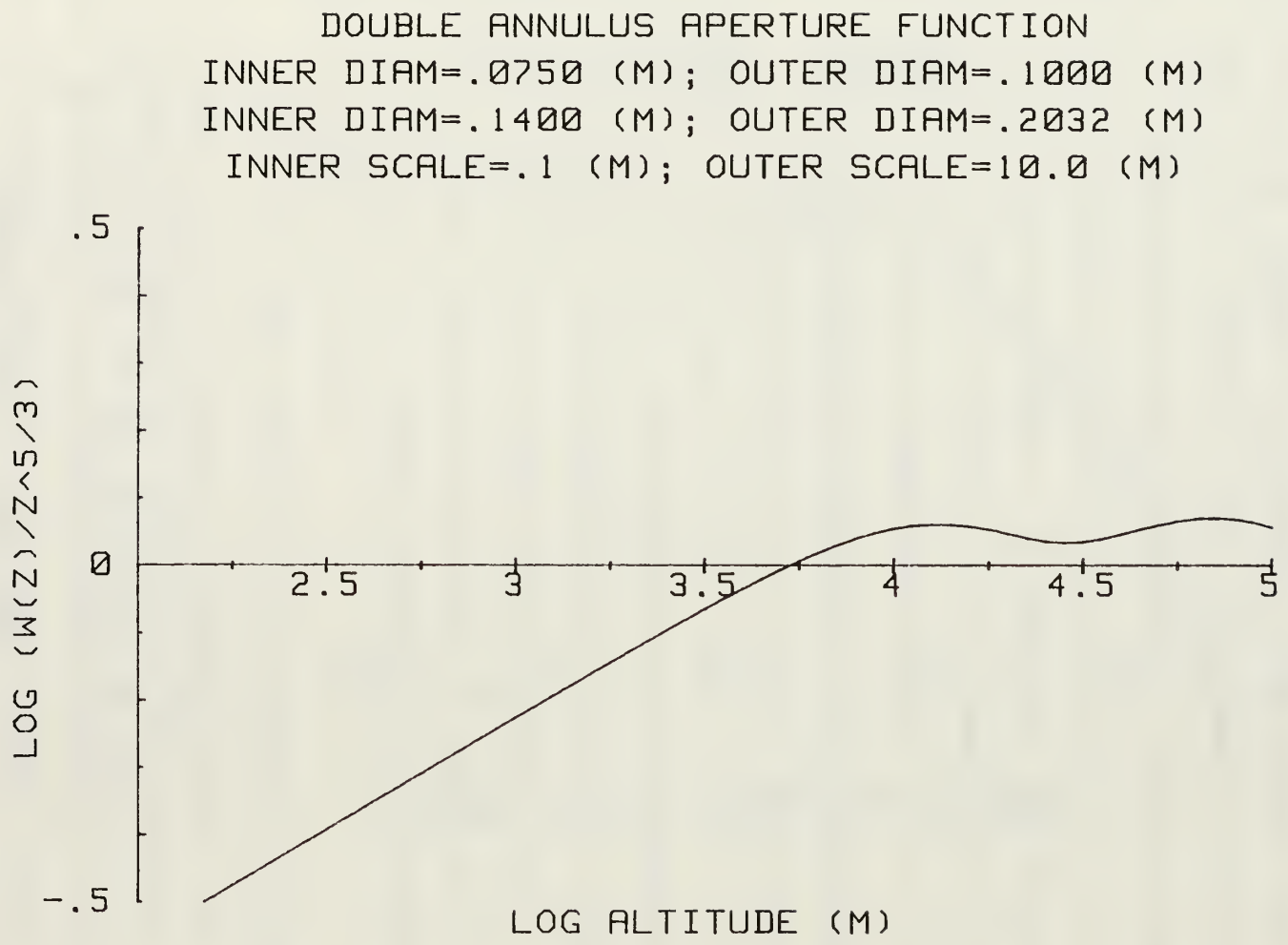

Figure 4.3a Error from $z^{5/3}$ for an Inner Scale of .1 m

will decrease. At some critical K_{max}, the upper limit will begin eliminating integrand producing a dramatic change in the weighting function.

Figure 4.3b shows the error from $z^{5/3}$ for the double annulus aperture weighting function with the z dependence in the upper limit of integration. As expected, we see little change at lower altitudes. At 40 km, the inner scale is now large enough to begin removing part of the integrand. The deviation from $z^{5/3}$ begins when the inner scale reaches 15 cm, and by 25 cm, the error from $z^{5/3}$ is a factor of three.

The inner scale behavior of the weighting function is not a problem in a measurement system, since values of C_n^2 at 40 km are approximately 10^{-22} $m^{-2/3}$. Disturbances to the electromagnetic wave propagating through the medium occur at lower z where C_n^2 is larger.

C. SENSITIVITY ANALYSIS CONCLUSIONS

Based on the results of sections A and B, the isoplanatic angle weighting function appears very robust. The only real theoretical problem, in terms of measurement, is saturation of the normalized variance. One might ask about outer scale effects. Nominally, the outer scale, except very near the surface, remains on the order of 10 m [Ref. 42]. This can be seen from the Reynolds number. The Reynolds number is, (as shown in the Background section),

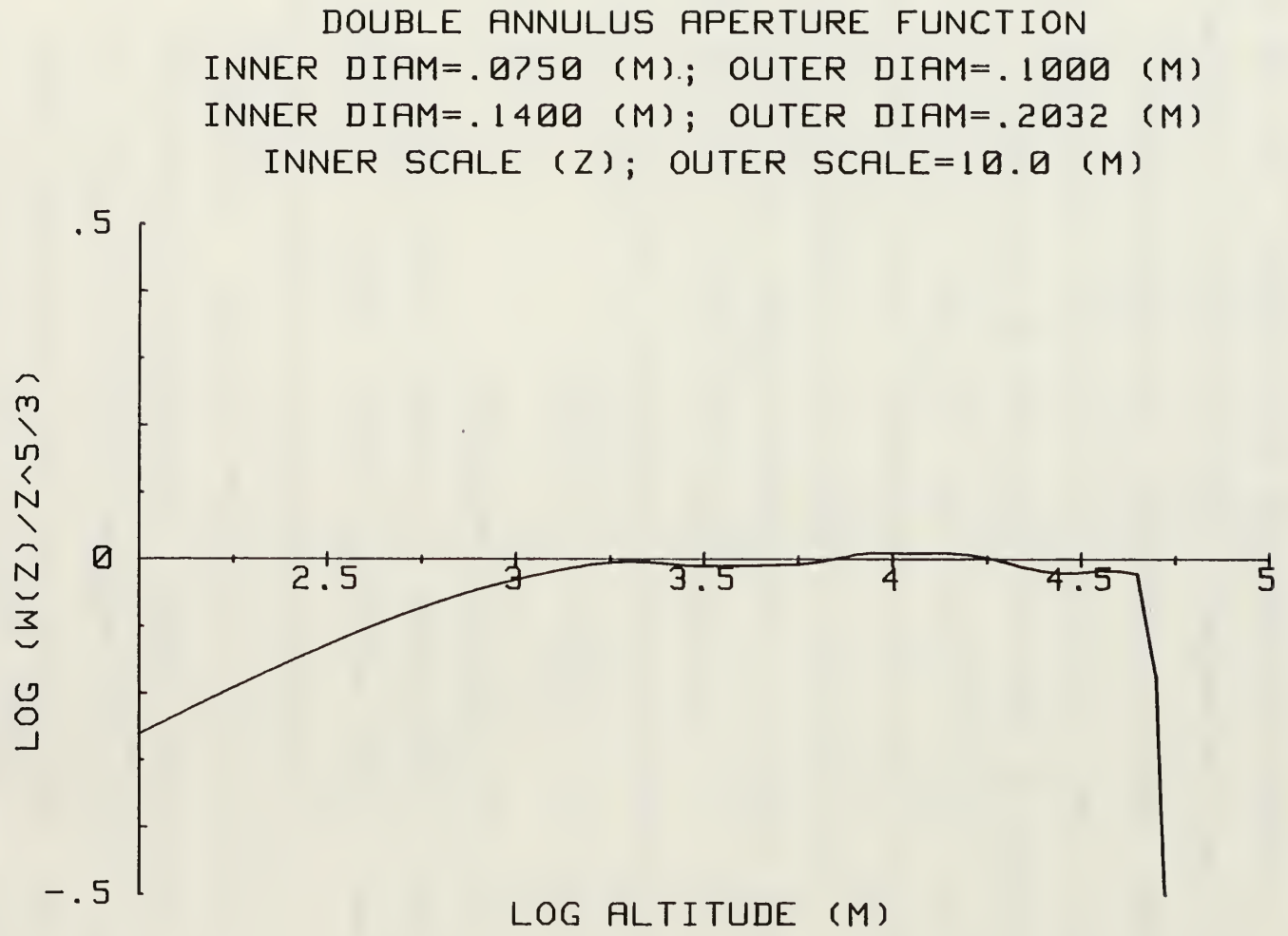

Figure 4.3b Error from $z^{5/3}$ for a Double Annulus Aperture with the Inner Scale Changing with Altitude

$$Re = \frac{vL}{\nu}$$

where v is the velocity, L is a characteristic size of the flow and ν is the kinematic viscosity. The onset of turbulence occurs at Reynolds numbers of 2000 or greater. L in the free atmosphere remains about the same and ν increases with altitude. Thus, velocity is the parameter responsible for large Re. Since L does not vary considerably, L_0, the next scale size smaller, should not vary considerably either. Near the earth, L has an immediate fixed boundary condition that reduces its size.

V. INSTRUMENT QUALIFICATION

Currently, many DoD agencies require isoplanatic angle measurements at night. Based on this need, we fabricated a fourth generation isoplanometer. What follows is a brief description of the hardware, detailed analysis of instrument qualification and a comparison with the 10 cm "top hat" isoplanometer.

A. HARDWARE

1. Telescope

The double annulus aperture function of Figure 3.8, was developed for use on an 8" Schmidt-Cassegrain telescope. The Celestron C8 is a reasonably priced and readily available Schmidt-Cassegrain telescope with a high quality worm-gear drive for star tracking. The choice of Bessel functions as a spectral basis set has the advantage of simple obscuration implementation. The aperture obscuration is two disks made of flat black rubber adhered to the Celestron corrector plate with rubber cement. This allows removal at a later date without damage to the optics or coatings. With the exception of the obscuration, all of the equipment associated with the telescope (tripod, mount, etc.) is furnished by Celestron.

2. Detector

The detector subassembly is a modification of the already existing 10 cm "top hat" isoplanometer detector developed by Walters [Ref. 30]. Walters engineered and implemented the modifications to the fourth generation detector subsystem, associated signal conditioning hardware and software. The detector subassembly screws into the rear of the telescope. Incident radiation is directed over one of two paths. To acquire stars and focus the telescope, the light enters a wide angle eyepiece. Otherwise, the light passes through a pupil (on the order of millimeters), and is incident on a photomultiplier tube that senses the intensity fluctuations (stellar scintillations). The image is slightly defocused to remove the effects of any inhomogeneities on the surface of the photomultiplier. The photomultiplier is chosen to have good red response, which causes a slight improvement in the weighting function at low altitudes, Figure 3.10 and suppresses any Rayleigh backgound.

We should note that the pupil in this instrument can be much larger than the previous isoplanometer, since it is intended for night use only. The 10 cm isoplanometers use a chopper to make reference background measurements necessary for daytime operation. This feature is not required on the fourth generation system for the same reason as above. A schematic diagram of the detector subassembly is shown in Figure 5.1.

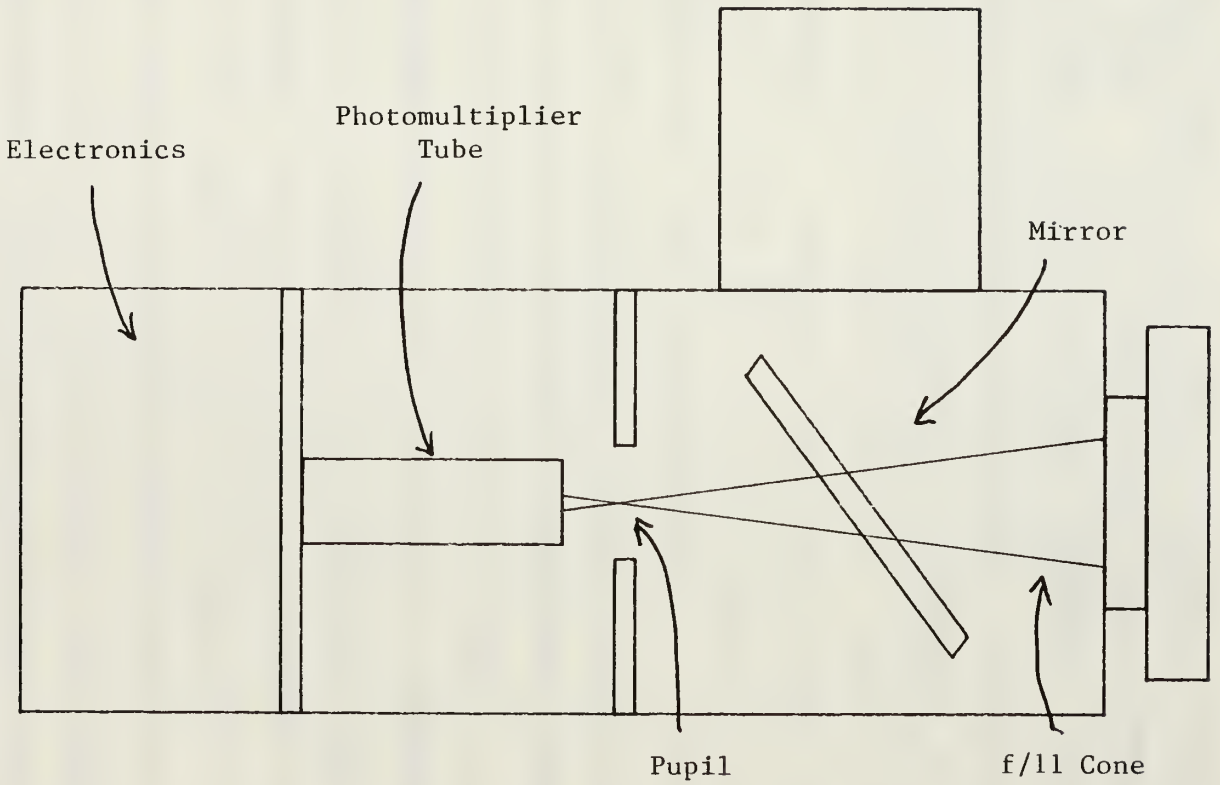

Figure 5.1 Fourth Generation Isoplanometer Detector Schematic

3. Signal Conditioning and Isoplanatic Angle Extraction

The first fourth generation isoplanatic angle measurement system (A system), uses a Hewlett-Packard HP 3421 Data Acquisition unit to sample the output of a signal conditioning unit. The signal conditioning unit performs two functions. It low pass filters the incoming signal below 500 Hz and calculates the mean and rms values of the input voltage data from the photomultiplier. The Data Acquisition Unit, with an internal voltmeter, detects the voltage on each channel once/second and relays the information to a Hewlett-Packard 217 Computer.

Once the data is in the computer, the normalized variance of the signal is calculated from the mean and rms values of the voltage. Obtaining the isoplanatic angle is then a simple matter of applying the constant A' to the normalized variance. The average intensity (in volts) and isoplanatic angle (in μrads) are plotted on a graphics monitor. A real-time plot of the average intensity can be very helpful during data acquisition in determining the occurrence of clouds and monitoring stellar tracking errors. The isoplanatic angle is very robust to drifts in the average intensity since we normalize the variance.

On later systems (B systems), the HP 3421 is replaced by an Infotek A-D converter that resides within the HP computer. The computer samples the A-D converter so that

one isoplanatic angle measurement is made per second. The computer does not store all the isoplanatic angle data. Instead, the computer calculates ten second averages and stores the averages every 15 minutes.

The fourth generation isoplanometer uses software that has evolved and become more "friendly" with each field experiment. Currently, the zenith angle dependence of the isoplanometer angle is removed within the main program.

B. ZENITH ANGLE QUALIFICATION TESTS

It is an interesting problem to know if your instrument is really measuring the isoplanatic angle. One could fly balloons and obtain a direct measurement of the C_n^2 profile and integrate with $z^{5/3}$ weighting, however, Walters [Ref. 30], has developed a much less costly and simpler technique. The isoplanatic angle is

$$\theta_0^{-5/3} = [\sec \phi]^{8/3} A' \left(\frac{\sigma_s^2}{S^2}\right) , \qquad (5.1)$$

including the zenith angle dependence. For increasing path length (higher zenith angles), the normalized variance will increase since the light is encountering more integrated turbulence. Hence, a plot of σ_s^2/S^2 versus log (sec ϕ) should have an 8/3 slope if the instrument is truly measuring the isoplanatic angle to within a multiplicative constant.

Walters used this technique to qualify the 10 cm "top hat" isoplanometer (really 11 cm) [Ref. 30]. The following is an application of the above technique to the fourth generation system, but first a caution. Clearly, if the atmosphere is horizontally homogeneous (i.e., composed of onionskin layers), the technique should be effective. However, if the atmosphere is irratic and the turbulence is not uniform over the night sky, this technique will not be as reliable.

We (D. L. Walters and myself) obtained qualification measurements for the fourth generation system at two different locations. The first data set is from McDonald Observatory in western Texas. The night was ideal for instrument qualification using the zenith angle technique. The isoplanatic angles were on the order of 15μ rad. In Figure 5.2 each point represents one 10 sec average of the normalized variance, while each group of points is 400 seconds of data on a given star. Figure 5.2 shows very good agreement with theory on this test. The least-squares fit has a slope of 2.60, which is not a significant error from 8/3. The least-squares fit does not include the two data sets at high zenith angles since the normalized variance is saturating.

The second set of data is from Albuquerque, New Mexico, acquired when atmospheric conditions were less than optimal.

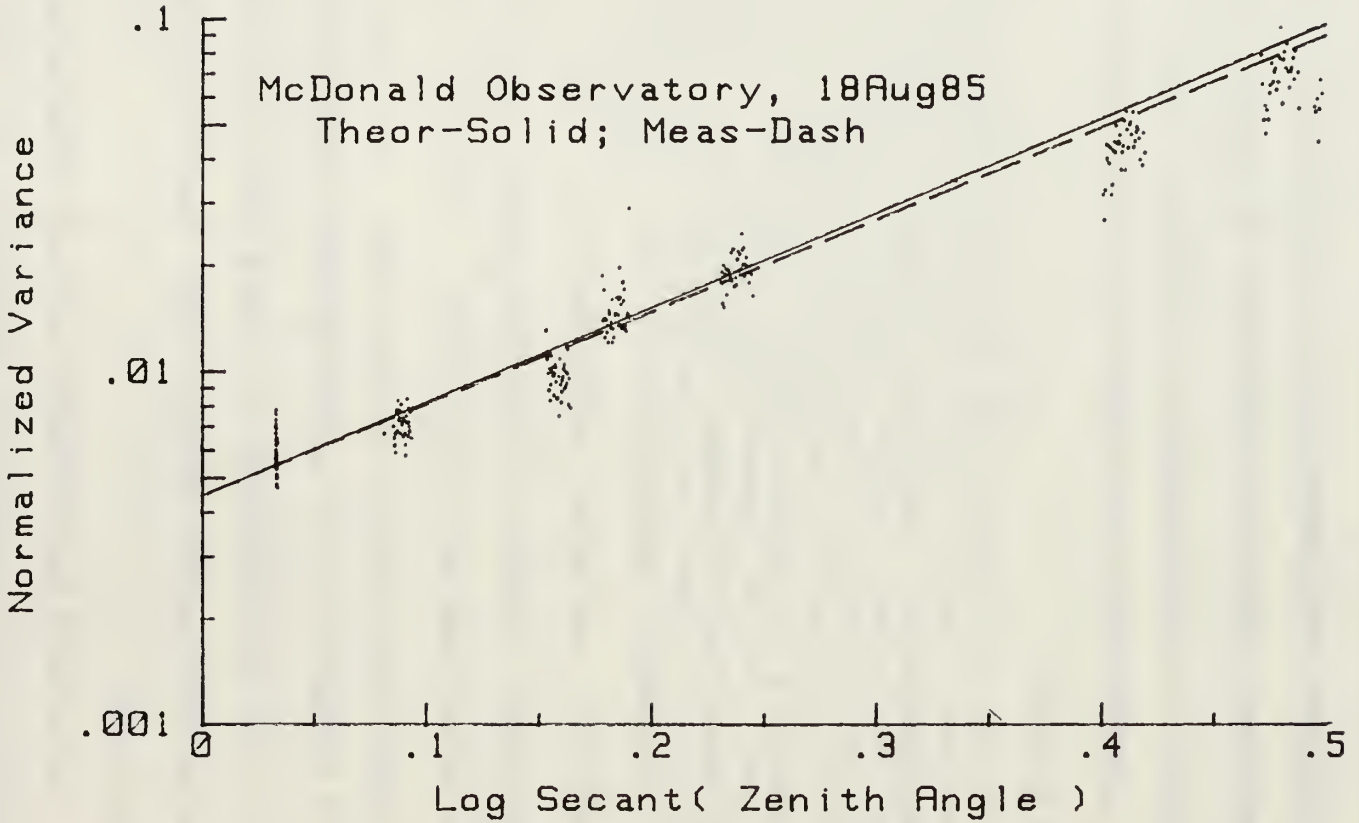

Figure 5.2 Zenith Angle Test for the Fourth Generation Isoplanometer

During the daylight hours, large thunderstorm cells formed, dissipating at night into a layer of cirrus. About 0200, the cirrus cleared and we obtained the data set in Figure 5.3. The least-squares fit includes the three observations at lower zenith angles. The slope of the least-squares fit is 2.48, less than the 8/3 theoretical. Based on the conditions that night, the results are very good.

More interesting in Figure 5.3 is the behavior of the normalized variance at large zenith angles (last two data sets). We note that the normalized variance is no longer changing for these data sets. Clearly, the path is long enough to induce saturation in the normalized variance. For the fourth generation isoplanometer this occurs at normalized variances of about .06 to .07. The 10 cm isoplanometer saturates at normalized variances of .2 to .3. The aperture averaging has lowered the normalized variance between the two instruments the predicted amount. Remember, the calibration constant A' for the 10 cm isoplanometer is approximately 1×10^{10}, while A' for the fourth generation isoplanometer is 4×10^{10}. Hence, for a given isoplanatic angle, the normalized variance for the new system will be a factor of four lower than the 10 cm system. Thus, the double annulus system is saturating at an equivalent normalized variance. We still have not resolved whether the increased aperture averaging aids in forestalling

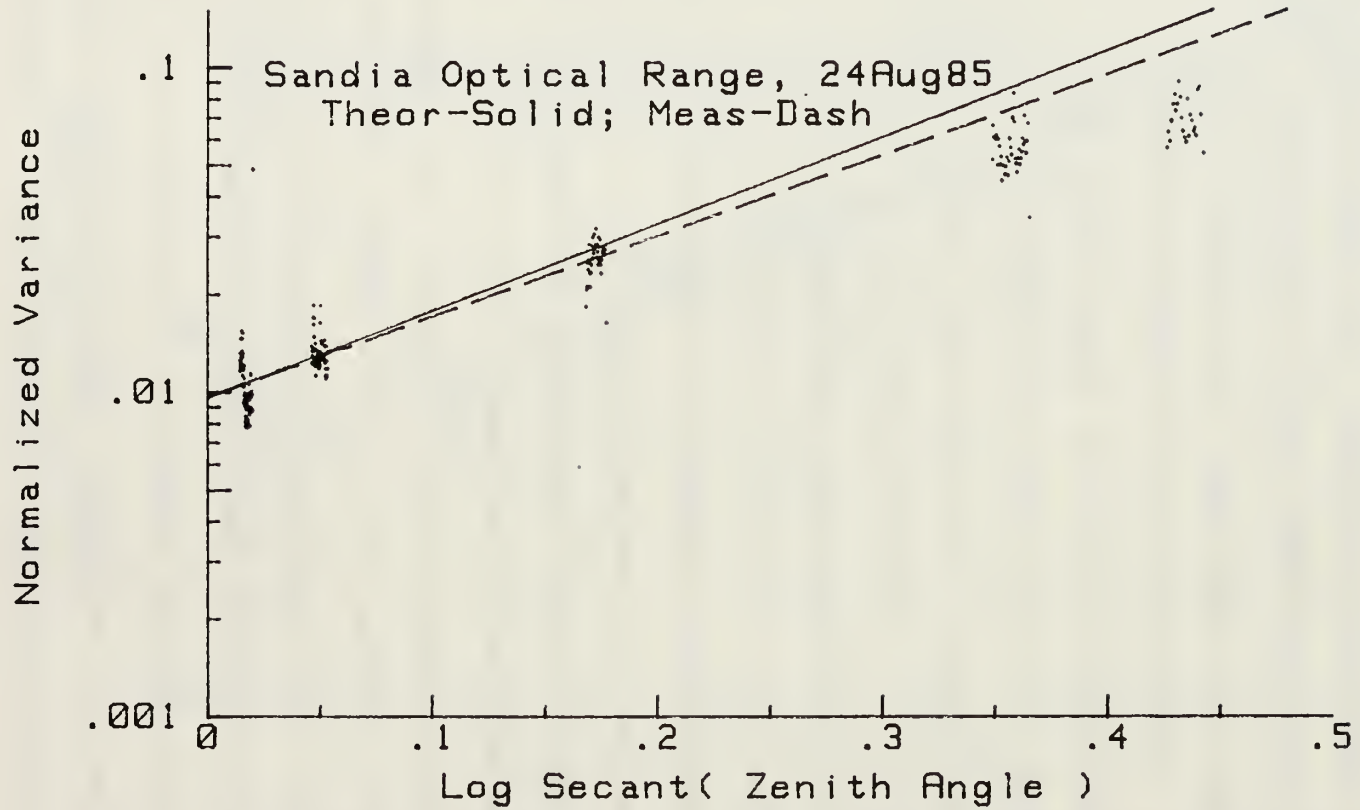

Figure 5.3 Zenith Angle Test for the Fourth Generation Isoplanometer

saturation. The fourth generation system saturates at its nominal "saturation" normalized variance, however, it may take four times the turbulence to make it saturate. The fourth generation system seems to take reliable data at slightly larger zenith angles than the 10 cm system. Resolving this question requires simultaneous observations with both instruments on the same stars for a zenith angle check. This test has not been possible due to instrument availability.

C. APODIZED AND 10 cm ISOPLANOMETER COMPARISON

Even though simultaneous zenith angle tests were impossible in Albuquerque due to instrument availability and atmospheric conditions, we did obtain simultaneous data on Vega on August 25, 1985. The data is contained in Table 3. The mean isoplanatic angle for the 10 cm isoplanometer data is 6.7 $\pm$ .17; while the double annulus averaged 6.8 $\pm$ .15. This shows very good agreement between the two instruments and removes the ambiguity of the multiplicative constant in the zenith angle test. Table 3 also shows an unstable night. The isoplanatic angles range from 4.5 μrad to 9.0 μrad over a one hour period.

D. ISOPLANATIC ANGLE MEASUREMENTS WITH SUPPORTING METEOROLOGICAL DATA

During September, 1985, the fourth generation system was in use on Haleakalea crater, Maui, HI. One night, our data

TABLE 3

10 cm AND DOUBLE ANNULUS COMPARISON

Time (Local Standard)	10 cm (μrad)	Double Annulus (μrad)
2211	7.5	7.8
2212	9.0	8.9
2213	8.3	8.9
2214	8.3	7.9
2216	7.6	---
2219	6.6	6.3
2220	6.9	7.3
2222	6.9	6.7
2224	5.4	5.8
2226	4.7	6.1
2228	6.9	6.5
2229	5.7	7.0
2230	7.7	7.3
2231	7.3	7.1
2233.00	6.5	6.8
2233.41	6.9	6.8
2234	6.4	6.5
2235	6.6	6.6
2237	6.4	7.3
2238	7.4	6.6

TABLE 3 (CONTINUED)

Time (Local Standard)	10 cm (μrad)	Double Annulus (μrad)
2240	6.3	6.9
2241	6.3	7.4
2242	8.3	7.5
2243	6.7	6.6
2246	7.0	7.1
2247	6.9	6.9
2249	7.2	7.0
2250	6.5	6.5
2252	6.2	6.4
2253	6.0	6.0
2255	6.4	5.9
2256	4.5	4.7
2257	4.9	5.3

collection overlapped a meteorological balloon flight. The balloon provided altitude, pressure, temperature, dewpoint depression, relative humidity, wind speed, and direction. Figure 5.4 shows the real-time computer output on 17 Sep 1985 (Star 17=Vega). The solid line is the time history of the average intensity, while the points represent 1 second measurements of the isoplanatic angle. The spikes in the average intensity occurred when the telescope dome lights were turned on. Figure 5.4 shows a small isoplanatic angle. However, no zenith angle correction has been applied to this data. Figure 5.5 contains this 15 minute set of data after application of the zenith angle dependence. The isoplanatic angles are in fact fairly large, approximately 13 μrad. These large isoplanatic angles indicate low turbulence between 8-15 km. Hence, the wind profile should show low wind speeds and small shears. The complete set of meteorological data is contained in Appendix B, the wind shear data is as follows. The balloon data indicates three shear layers (2 km, 14 km, 27 km). The wind speed at the 2 and 14 km levels is approximately 4 knots, while at 27 km is 47 knots. These wind speeds are very low and indicate that very little shear driven turbulence is present. Hence, the large isoplanatic angles agree with the observed wind profile data.

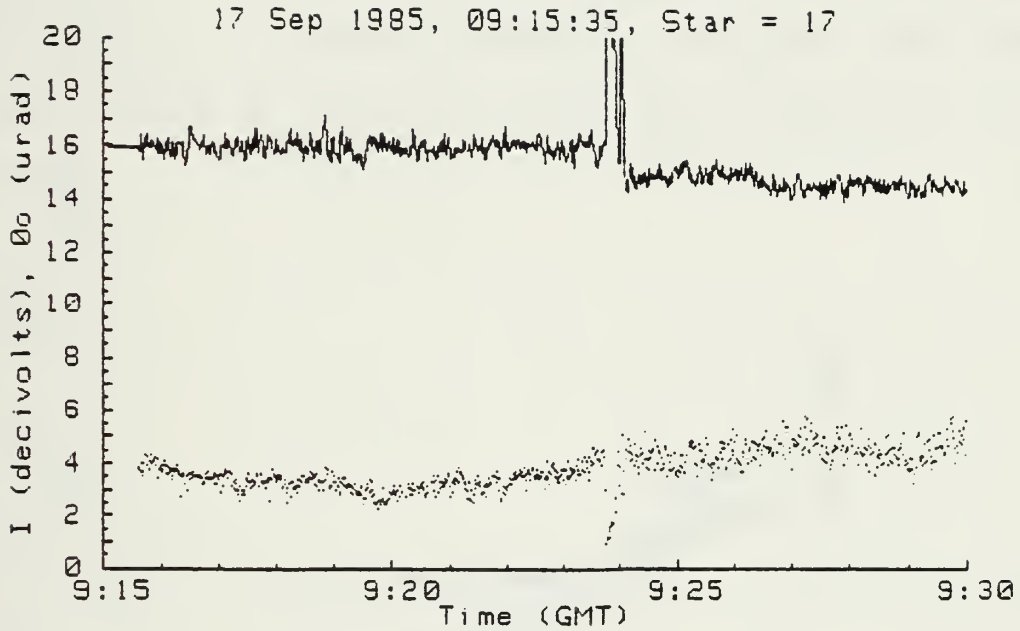

Figur 5.4 Real-Time Output of the Fourth Generation Isoplanometer at Maui, HI

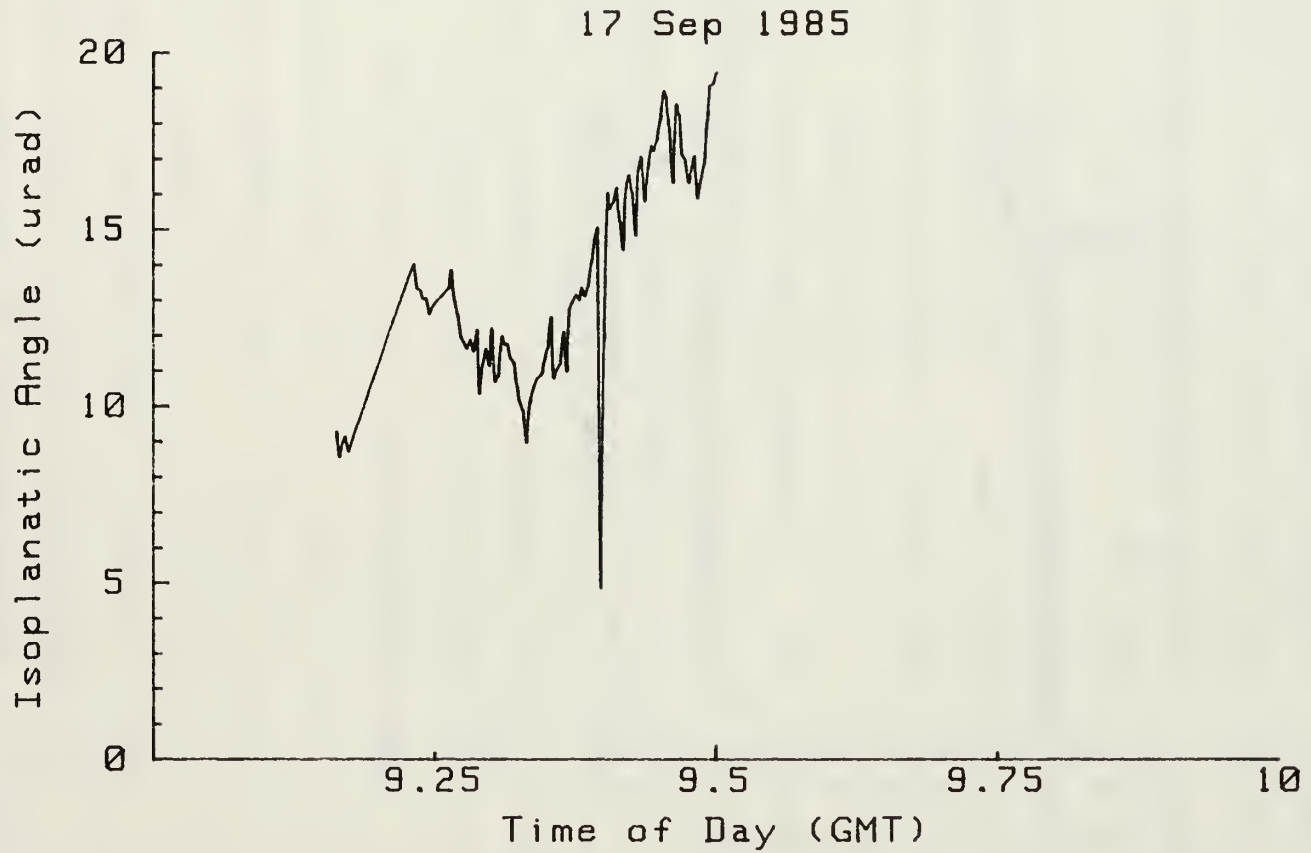

Figure 5.5 Maui Data of Figure 5.4 after the Zenith Angle Dependence has been Removed

E. QUALIFICATION CONCLUSIONS

Based on the zenith angle tests, the simultaneous measurements with the 10 cm device and the measurements with supporting meteorological data, we conclude that the instrument is indeed measuring the isoplanatic angle correctly. Currently, two fourth generation instruments are in operation at different locations worldwide. This data is being archived at the Naval Postgraduate School by D. L. Walters.

VI. DATA COLLECTED IN MAUI

As mentioned previously, we conducted a trip to Maui, HI supplying an isoplanometer to the AMOS facility. During this trip, weather prohibited acquisition of large amounts of data, however, we did obtain that data mentioned in Chapter V, along with what I will present here.

In this section, we will see one of the greatest assets of the fourth generation isoplanometer. That is its ability to make isoplanatic angle measurements effortlessly each second. The following plots show trends in isoplanatic angle data that have not been observed before.

Figures 6.1-6.7 are real-time computer output of each 1 second isoplanatic angle measurement. As in Figure 5.4, the solid line is the average stellar intensity and each point is an isoplanatic angle measurement. We might note that the average intensity is much more steady than in Figure 5.4. This is due to the lack of high thin cirrus clouds. Also, in Figure 6.2, the steps are caused by changing the voltage to the photomultiplier. Note that these changes do not affect the isoplanatic angle measurements. In Figure 6.7, the deviations in the average intensity are due to the star beginning to move out of the telescope field-of-view.

In these data sets, we see isoplanatic angles ranging from 16 μrad to 5 μrad. This, of course, indicates a very

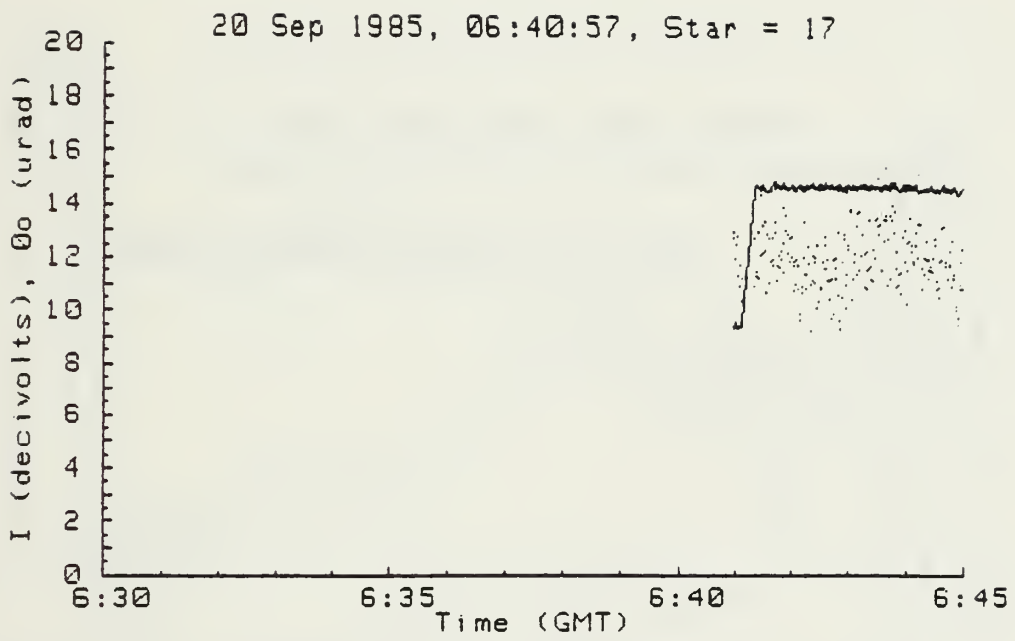

Figure 6.1 Real-Time Isoplanometer Output from Maui, HI

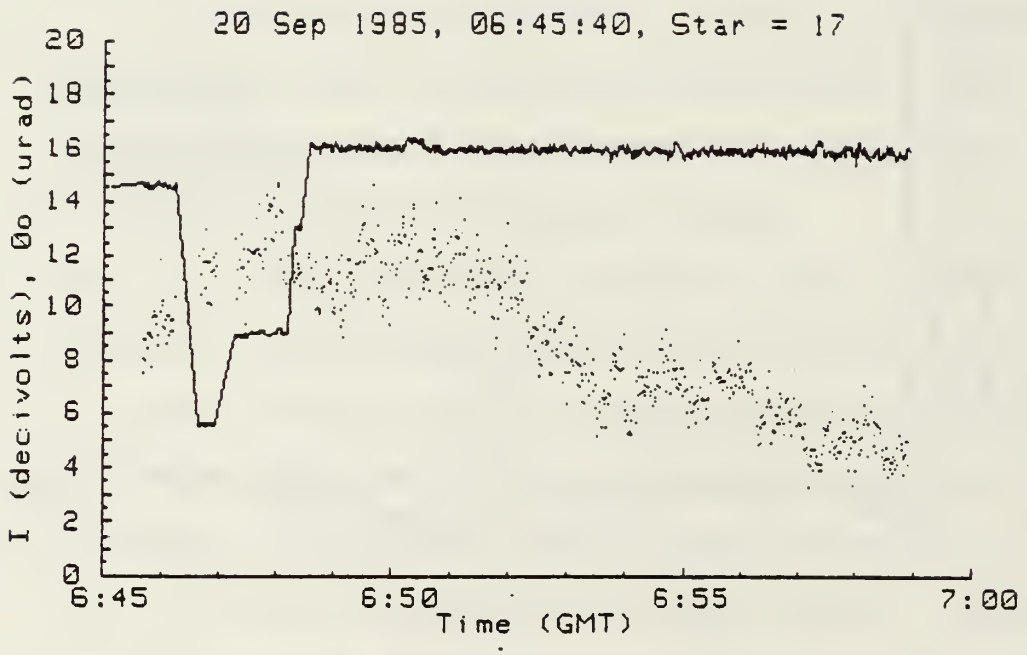

Figure 6.2 Real-Time Isoplanometer Output from Maui, HI, Showing Voltage Changes to the Photomultiplier and a Rapid Decrease in the Isoplanatic Angle

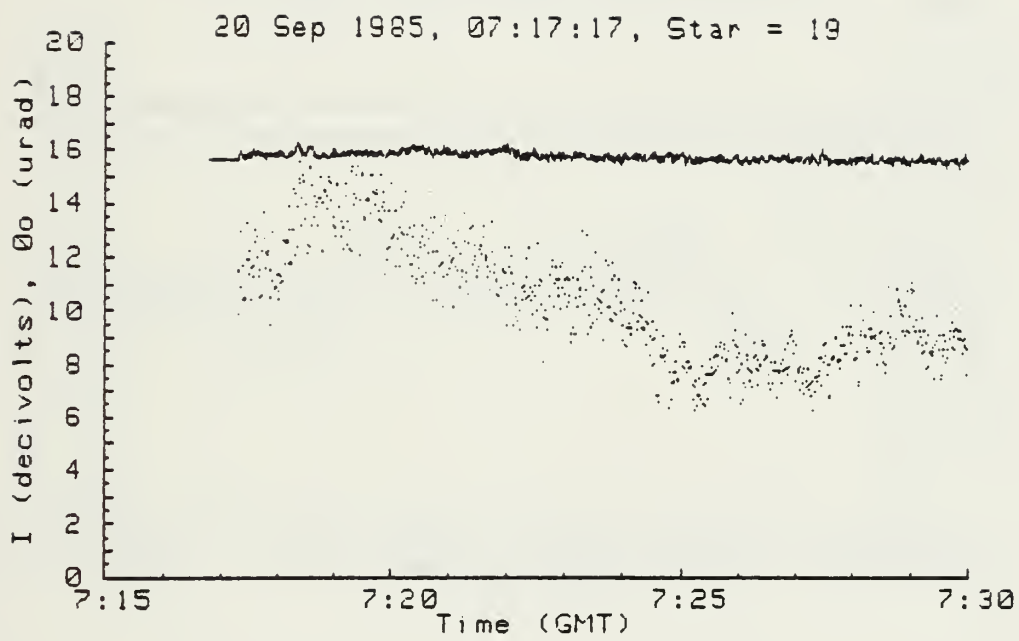

Figure 6.3 Real-Time Isoplanometer Output from Maui, HI, Showing a Rapid Decrease in the Isoplanatic Angle

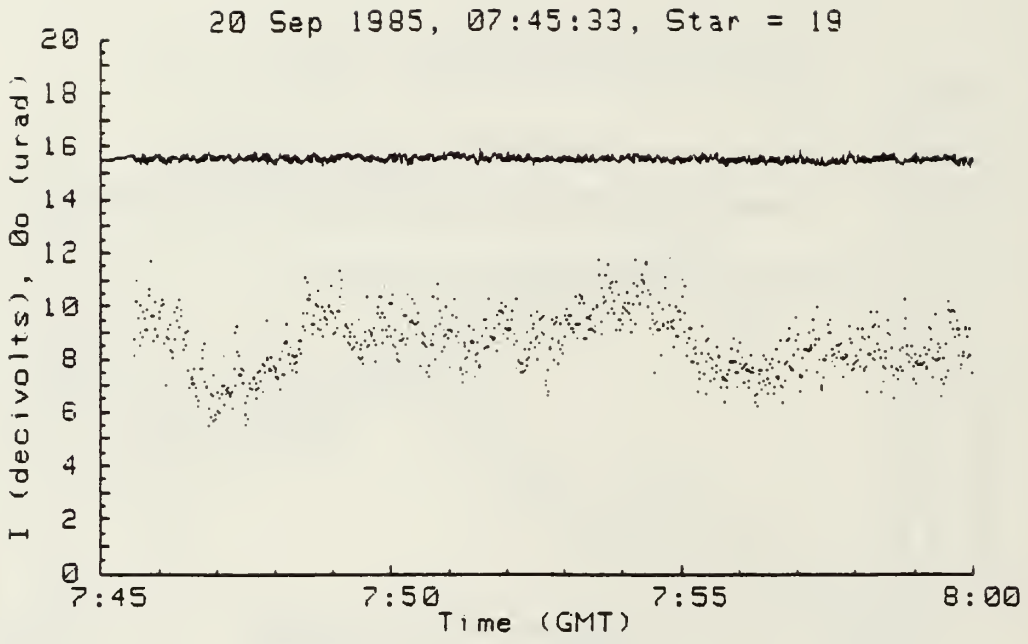

Figure 6.4 Real-Time Isoplanometer Output from Maui, HI, with Oscillations of 90 Seconds

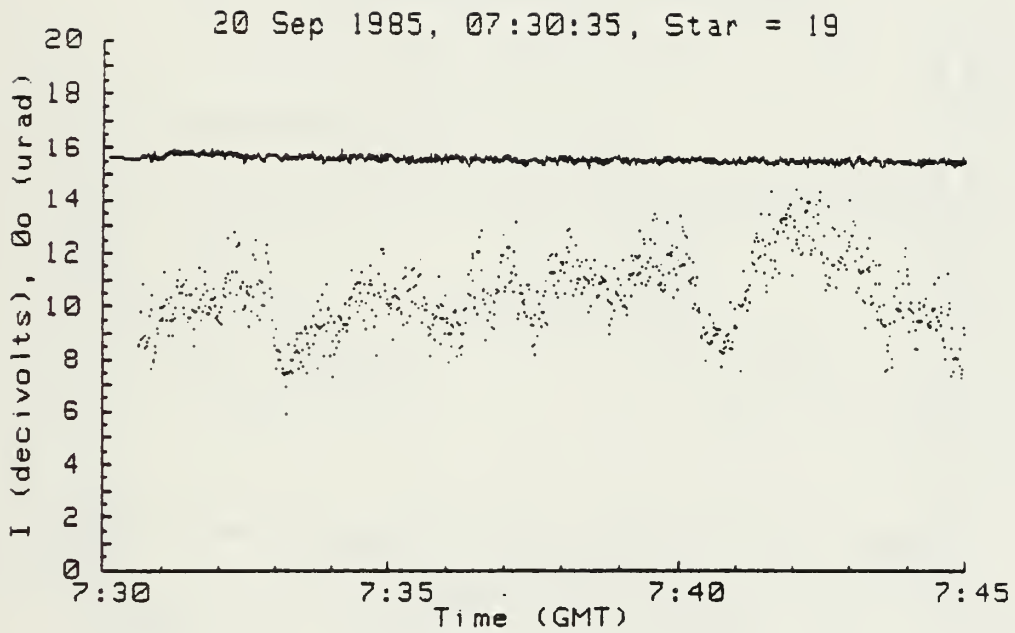

Figure 6.5 Real-Time Output of the Isoplanometer in Maui, HI, Showing Oscillations with 1 Minute Periods

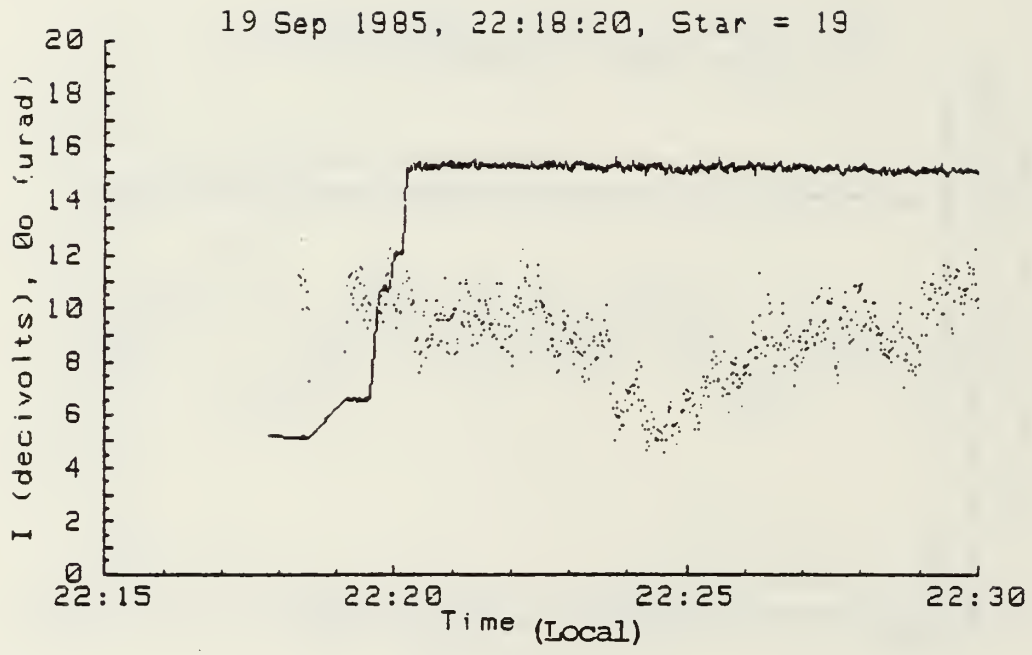

Figure 6.6 Real-Time Output of the Isoplanometer in Maui, HI, Showing Oscillations

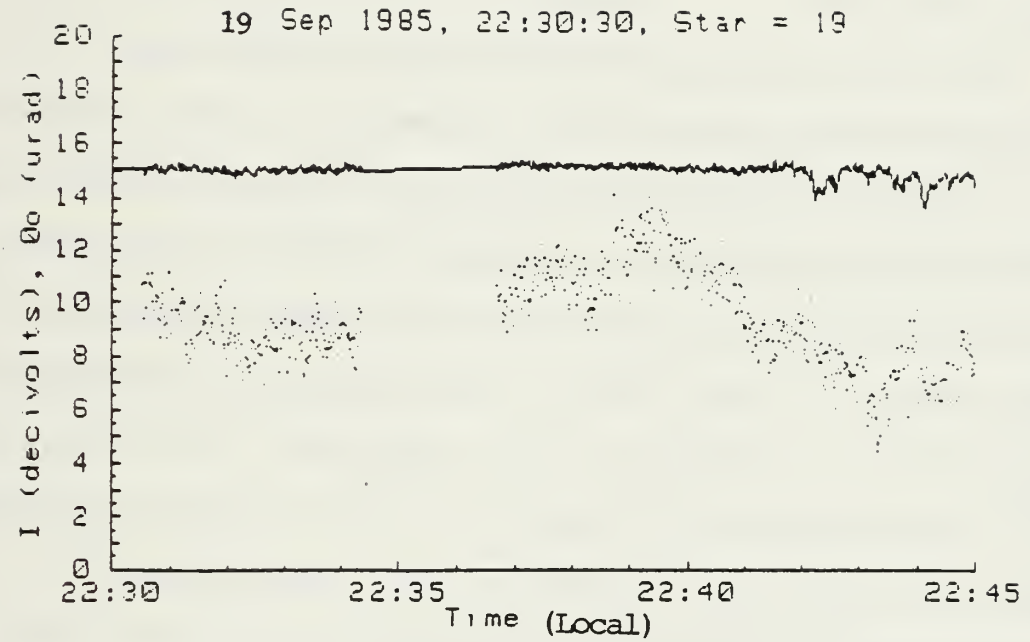

Figure 6.7 Real-Time Isoplanometer Output from Maui, HI, Showing the Star Moving from the Telescope Field of View

unstable night. But, what is most interesting are the low frequency oscillations present in the data. Figure 6.4 has oscillations with periods on the order of a one minute, while Figure 6.5 shows oscillations on the order of three minutes. Unfortunately, no balloon measurements of meteorological data were performed on 20 September. Without supporting meteorological data, it is impossible to ascertain exactly the mechanism responsible for producing data like this.

Based on the isoplanometer weighting function, it is possible to make some general comments on the location of the turbulence that could produce this type of oscillation. Since the isoplanometer is weighted $z^{5/3}$, low altitude turbulence (boundary layer to 2 km) is not responsible for this behavior. Most likely, the turbulence producing the oscillations is located in the tropopause. At 10 km, the $z^{5/3}$ weighting and C_n^2 values are large enough to produce the lower isoplanatic angles we see. Researchers in Albuquerque, NM, indicate that they observe oscillatory data, with the second fourth generation isoplanometer, when the jet stream is moving into the area. As the jet stream approaches, wind speeds in the tropopause begin to increase. Periodically, the gradient Richardson number (ratio of potential temperature gradient to velocity gradient), will fall below the critical Richardson number (about $R_i = 1/4$),

and the flow will give way to shear driven turbulence. The jet stream is not close enough to supply the energy necessary to maintain the turbulence. Hence, after a short period of time, the flow becomes stable and the isoplanatic angles increase. Once the jet stream has completely entered the area, the isoplanatic angles no longer oscillate, but remain low due to constant turbulence. Thus, one can surmize that the oscillatory isoplanatic angles are caused by temporally intermittent turbulence.

More research needs to be done in the area of isoplanatic angle measurement with supporting meteorological data. Once trends in isoplanatic angle data have been established for certain atmospheric phenomena, balloon data may no longer be necessary for an accurate picture of turbulence in the tropopause.

VII. REFRACTIVE TURBULENCE PROFILING

In the discussion on the isoplanatic angle, we saw that by measuring the normalized variance, we avoided the unknown C_n^2 profile. Clearly, the integrated parameters like θ_0 and r_0 do not provide direct information on the distribution of turbulence with altitude. Many laser system design analyses require C_n^2 profiles. However, they are difficult to obtain by remote measurements. In Chapters IV and V, I presented a profile measured by microthermal probes on a balloon. This represents a direct measurement of C_n^2, with very high vertical resolution (on the order of meters), along a single vertical path through the atmosphere. Actively, C_n^2 profiles are measured by acoustic sounders (up to approximately 1 km) and pulsed Doppler radars (2-30 km) [Refs. 41, 43]. Active techniques provide good vertical resolution, but the cost of such instruments is quite high.

In this chapter and the next, we will look at profiling C_n^2 passively by direct inversion of the amplitude scintillation covariance equation with application of the Tikhonov regularization technique. But before delving into a rigorous solution, we should make note of the other passive techniques for measuring C_n^2 profiles.

A. PREVIOUS WORK

The time lagged covariance function of amplitude scintillations for a point source and two equal circular aperture receivers is given by [Ref. 44],

$$B_\chi(\rho') = 4\pi k^2 \int_0^\infty dz' C_n^2(z') \int_0^\infty K' dK' \Phi(K') J_0[K'|\rho' - v(z')\tau|]$$

$$x \sin^2\left[\frac{K'^2 z'}{2k}\right] \left[\frac{2J_1(\frac{K'D}{2})}{\frac{K'D}{2}}\right]^2 , \qquad (7.1)$$

where ρ' is the separation between the detectors, $v(z')$ is a wind profile, τ is the time-lag, $\Phi(K')$ is the $0.033K'^{-11/3}$ portion of the Kolmogorov spectrum and D is the diameter of the circular receiving apertures. Often this equation is written for point receivers. In that case the $J_1(x)/x \to 1$. For measuring C_n^2 profiles, we let the time-lag, τ, equal zero, removing the unknown velocity profile. Hence, $B_\chi(\rho')$ is in the form of a Fredholm equation of the first kind,

$$B_\chi(\rho') = A \int Q(z',\rho') C_n^2(z') dz' , \qquad (7.2)$$

where A is a constant and $Q(z',\rho')$ is the kernel given by the integral over K'. Fredholm equations of the first kind are notorious for being ill-posed (i.e., errors or noise in the data make the solution ill-behaved). In fact, Fredholm

equations of the first kind may have no solution at all. Peskoff [Ref. 45] was the first to invert this equation for point apertures. Shen [Ref. 46] realized that the problem was ill-posed and used a least-squares technique to minimize error. As time progressed, other methods for handling the ill-posed problem appeared. Heneghan and Ishimaru [Ref. 47] proposed a statistical inversion technique to compensate for the large errors induced by inversion. However, one should note that none of these techniques evolved into an actual measurement system. People began to realize that if the weighting function, W(z'), (3.3), could be made to peak, C_n^2 could be measured directly without inversion using (3.1).

1. Remote Probing with Apodized Apertures

To make W(z') peak requires filtering in the aperture or image plane [Refs. 31-33]. NOAA [Ref. 32] fabricated a C_n^2 profiling instrument (stellar scintillometer) based upon the filtering technique. By using three optical weighting functions, it measures values of C_n^2 at seven levels between 0-20 km. Unfortunately, the weighting functions, W(z'), are somewhat broad. The structure we observe in Figure 3.2 would not be as pronounced if this profile had been measured by the optical scintillometer. However, the scintillometer does follow the general trends of C_n^2 well.

In Appendix A, I show many weighting functions, W(z), for different apertures and spectra. This was an

effort to find highly peaked weighting functions for an optical scintillometer type instrument. Unfortunately, the quest proved fruitless, but other interesting weighting functions were found.

2. Binary Star Techniques

Several French researchers [Refs. 48-50] have developed a technique for profiling C_n^2 using a spacio-angular correlation function of two stars in a telescope aperture. The maxima in the correlation function correspond to levels of turbulent layers through the relationship,

$$\rho_i = \theta h_i \quad ,$$

where ρ_i is the location of a correlation maxima, θ is the angular separation of the binary stars and h_i is the altitude of the turbulence corresponding to the maxima. The group built instrumentation to measure C_n^2 profiles in this manner. They report vertical resolution on the order of 2 km, which is very good. However, being dependent on binary stars is a significant hinderance, esecially when the C_n^2 profile vertical resolution depends on their angular separation.

B. INVERSION WITH TIKHONOV REGULARIZATION

Jarem [Refs. 3, 4] implemented a regularization technique for handling the ill-posed direct inversion problem on the covariance function for point detectors.

This has been the first "new" attempt at C_n^2 profiling recently. The Tikhonov regularization amounts to filtering the high spatial frequencies of the inverted spectrum. Since aperture averaging also filters high spatial frequencies, it seems reasonable to include this effect in the covariance function to aid in regularization. In the following sections, I will invert the aperture averaged covariance function by Hankel transform and apply the Tikhonov technique. This inversion is a general approach developed by Peskoff [Ref. 45]. The regularization portion follows Tikhonov [Ref. 5] and Jarem [Refs. 3, 4].

1. Inverting the Fredholm Equation

The covariance function of amplitude scintillations for a single point source (star) and two identical but arbitrary apertures at zero time lag is given by [Ref. 44],

$$B_\chi(\rho') = 4\pi^2 k^2 \int_0^\infty dz' C_n^2(z') \int_0^\infty K' dK' \Phi(K') \sin\left(\frac{K'^2 z'}{2k}\right) I(K') \times J_0(K'\rho') \quad , \tag{7.3}$$

where k is the wavenumber of the monochromatic electromagnetic wave, K' is the spatial frequency of the amplitude scintillations, $\Phi(K')$ is the $K'^{-11/3}$ dependence of the

Kolmogorov spectrum, ρ' is the detector separation and $I(K')$ is the intensity spectrum of the receiver optics. We might note that the equation is valid only in the inertial subrange due to the Kolmogorov spectrum. Like Jarem, we will extend the limits of integration over C_n^2 such that

$$C_n^2(z') = C_n^2(-z') \; ; \quad -L < z' < L \quad ,$$

where L is the path length over which C_n^2 is non zero. This equates to making $C_n^2(z')$ an even function.

The two-dimensional Hankel transform of $B_\chi(\rho')$ is the spectrum $F_\chi(K')$ given by

$$F_\chi(K') = 2\pi \int_0^\infty B_\chi(\rho') J_0(K'\rho')\rho' d\rho' \quad . \tag{7.4}$$

Substituting (7.3) into (7.4) gives

$$F_\chi(K') = 4\pi^3 k^2 \int_{-\infty}^{\infty} dz' C_n^2(z') \int_0^\infty dK \Phi(K) I(K) \sin^2\left[\frac{K'^2 z}{2k}\right]$$

$$x \int_0^\infty \rho' d\rho' K J_0(K\rho') J_0(K'\rho') \quad . \tag{7.5}$$

Peskoff points out that

$$\int_0^\infty \rho' d\rho' K J_0(K\rho') J_0(K'\rho') = \delta(K-K') \quad . \tag{7.6}$$

This allow us to complete the K integration giving

$$F_\chi(K') = 4\pi^3 k^2 I(K') \Phi(K') \int_{-\infty}^{\infty} dz' C_n^2(z') \sin^2 \left[\frac{K'^2 z'}{2k}\right]. \tag{7.7}$$

Using the double angle relation $\sin^2\alpha = (1/2)(1-\cos 2\alpha)$, (7.7) becomes

$$F_\chi(K') = 2\pi^3 k^2 I(K') \Phi(K') \int_{-\infty}^{\infty} dz' C_n^2(z') - \int_{-\infty}^{\infty} dz' C_n^2(z')$$

$$\times \cos \left[\frac{K'^2 z'}{k}\right] \quad . \tag{7.8}$$

Jarem notes that $\int_{-\infty}^{\infty} dz' C_n^2(z') = 2\bar{C}_n^2$, where $\bar{C}_n^2$ is the average value of C_n^2 along the path. The second term represents the Fourier transform of $C_n^2(z')$, which we will call $C_n^2(K')$. Substituting these results into (7.8) gives

$$F_\chi(K') = 2\pi^3 k^2 I(K') \Phi(K') [2\bar{C}_n^2 - C_n^2(K')] \quad . \tag{7.9}$$

Jarem defines a set of dimensionless variables for convenience,

$$K = K'^2 \left(\frac{L}{k}\right) \quad , \quad z = \frac{z'}{L} \quad , \quad \rho = \frac{\rho'}{d} \quad ,$$

where d is the maximum separation of the detectors. It is interesting to note that (L/k) is related to the Fresnel zone size since

$$\left(\frac{L}{k}\right)^{1/2} = \left(\frac{\lambda L}{2\pi}\right)^{1/2} = \frac{f}{(2\pi)^{1/2}} \quad ,$$

where f is the Fresnel zone size. With the new variables, $\Phi(K')$ becomes

$$\Phi(K') = .033K'^{-11/3} = .033\left(\frac{k}{L}\right)^{-11/6} K^{-11/6} = \left(\frac{k}{L}\right)^{-11/6} \Phi(K). \tag{7.10}$$

If the receiver aperture is given by a "top hat" function, I(K') becomes

$$I(K') = \left[\frac{2J_1\left(\frac{K'D}{2}\right)}{\frac{K'D}{2}}\right]^2 = \left[\frac{2J_1\left(\frac{K^{1/2}b}{2}\right)}{\frac{K^{1/2}b}{2}}\right]^2 = I(K), \tag{7.11}$$

where b is given by

$$b = D(k/L)^{1/2} \quad .$$

Making these substitutions into (7.8) gives

$$F_\chi(K') = 2\pi^3 k^2 \left(\frac{k}{L}\right)^{-11/6} \Phi(K) I(K) \int_{-\infty}^{\infty} L dz C_n^2(z')$$

$$- \int_{-\infty}^{\infty} L dz C_n^2(z') \cos(Kz)$$

Following Jarem, let

$$C_N^2(z) = \pi^3 k^3 \left(\frac{k}{L}\right)^{-11/6} C_n^2(z') \qquad (7.11b)$$

giving

$$F_\chi(K') = \left(\frac{2L}{k}\right) \Phi(K) I(K) \int_{-\infty}^{\infty} dz C_N^2(z) - \int_{-\infty}^{\infty} dz C_N^2(z) \cos(Kz)$$

$$= \frac{2L}{k} F_x(K) \qquad (7.12)$$

(On C_n^2, lower case n subscript indicates the dimensioned variable, while upper case N subscript indicates the dimensionless variable). Making similar substitutions into $B_\chi(\rho')$ leads to

$$B_\chi(\rho') = B_\chi(\rho) \tag{7.13}$$

where

$$B_\chi(\rho) = \frac{1}{\pi} \int_{-\infty}^{\infty} dz C_N^2(z) \int_0^{\infty} dK I(K) \Phi(K) \sin^2(\frac{Kz}{2})$$

$$\times J_0(aK^{1/2}\rho) \tag{7.14}$$

and

$$a = d(\frac{k}{L})^{1/2} \quad .$$

Another important relation is how the Hankel transform scales under the change of variables. Beginning with (7.4), using (7.12) and (7.13) gives

$$\frac{2L}{k} F_x(K) = 2\pi \int_0^{\infty} B_x(\rho) J_0(aK^{1/2}\rho) d^2\rho d\rho \quad .$$

Hence, $F_x(K)$ is

$$F_x(K) = \frac{\pi k d^2}{L} \int_0^{\infty} \rho d\rho B_x(\rho) J_0(aK^{1/2}\rho) \quad . \tag{7.15}$$

With the relations we have developed, (7.9) becomes

$$F_x(K) = G(K)[2\bar{C}_N^2 - C_N^2(K)] \quad , \tag{7.16}$$

where

$$G(K) = \Phi(K)I(K) \quad .$$

The solution to the integral equation becomes

$$C_N^2(z) = \frac{1}{2\pi} \int_{-\infty}^{\infty} C_N^2(K) e^{iKz} dK \tag{7.17}$$

or

$$C_N^2(z) = \frac{1}{2\pi} \int_{-\infty}^{\infty} \left[\frac{-F_x(K)}{G(K)} + 2\bar{C}_N^2 \right] e^{iKz} dK \quad . \tag{7.18}$$

This is the ill-posed solution of the integral equation. Tikhonov proposes using a low pass filter function q(K) such that the high spatial frequencies contaminated by the inversion process are removed. We should note that this process does nothing to errors at low spatial frequencies. The regularized solution is of the form

$$C_N^2(z) = \frac{1}{2\pi} \int_{-\infty}^{\infty} \left[\frac{-F_x(K)}{G(K)} + 2\bar{C}_N^2 \right] q(K) e^{iKz} dK \quad . \tag{7.19}$$

A profiling system would measure $B_\chi(\rho')$. Using the relations developed, $B_\chi(\rho')$ is scaled to $B_x(\rho)$ and transformed to $F_x(K)$. In (7.19), all the quantities are knowns with the exception of $\overline{C_N}^2$. $\overline{C_N}^2$ is given by

$$2\overline{C_N}^2 = \int_{-\infty}^{\infty} dz C_N^2(z) \quad ,$$

which can be defined as a dimensionless form of Fried's r_0 by

$$R_0 = 2\overline{C_N}^2 \quad ,$$

where

$$R_0 = \frac{4.66\pi^3}{\sec \phi} \left(\frac{k}{L}\right)^{-5/6} r_0^{-5/3} \quad , \qquad (7.20)$$

where ϕ is the zenith angle. Instruments exist to measure r_0 which immediately gives R_0.

Another unknown, in terms of a practical measurement system, is L. In reality, the value of L need only to be known approximately. The C_N^2 profile can be normalized by independent measurements of θ_0 and r_0.

2. Constructing the Filter Function

Clearly, in any measurement, noise will be present. Hence, the spectrum, $F_x(K)$, can be represented by a "true" component and a "noise" component,

$$F_x(K) = F_x^{t}(K) + F_x^{n}(K) \quad , \tag{7.21}$$

where the superscript t and n imply true and noise. Hence, $C_N^2(K)$ is also composed of a "true" and "noise" component. If we let

$$C_{\bar{N}}^2(K) = 2\overline{C}_N^2 - C_N^2(K) \quad ,$$

(7.15) becomes

$$F_x(K) = G(K)C_{\bar{N}}^2(K) \quad . \tag{7.22}$$

The kernel, G(K), is type I to good approximation in Tikhonov's representation. Type I implies that there are no zeros along the real axis and as $K \to \infty$, $B(K) \to 0$.

For type I kernels, the filter function, q(K) can be represented by

$$q(K) = \frac{[G(K)]^2}{[G(K)]^2 + M(K)} \quad , \tag{7.23}$$

where M(K) is a smoothing function. If the spectral characteristics of the noise are known, and the spectrum $C_N^2(K)$ unknown, M(K) becomes

$$M(K) = \alpha K^{2P} \quad , \tag{7.24}$$

where M(K) is a p^{th} order stabilizer with regularization parameter α. If the noise spectra and signal $(C_N^2(K))$ spectra are known, one can construct an optimal Wiener filter with

$$M(K) = \frac{S(K)}{N(K)} , \tag{7.25}$$

where S(K) is the signal spectra and N(K) is the noise spectra.

If the noise process is white, like the shot noise in a measurement system, Tikhonov states that P = 1/2 in (7.24). Following Jarem, we can make an approximation to the optimal Wiener filter, (7.25). Consider an error functional of the form

$$\varepsilon = \int_{-\infty}^{\infty} [C_N^2(z) - C_N^{2t}(z)]^2 dz , \tag{7.26}$$

where $C_N^2(z)$ has both signal and noise components and t in the second term denotes the "true" component of $C_N^2(z)$. By Parseval's theorem, we can rewrite (7.26) as

$$\varepsilon = \frac{1}{2\pi} \int_{-\infty}^{\infty} [C_N^2(K) - C_N^{2t}(K)]^2 dK . \tag{7.27}$$

Now, $C_N^2(K)$ is given by

$$C_N^2(K) = \left[2\bar{C}_N^2 - \frac{F_x(K)}{G(K)}\right] \left[\frac{[G(K)]^2}{[G(K)]^2 + M(K)}\right] \qquad (7.28)$$

and $C_N^{2t}(K)$ is given by (7.16). Substituting (7.16), (7.28) and (7.21) into (7.27) gives

$$\varepsilon = \frac{1}{2\pi} \int_0^\infty \left[\left[2\bar{C}_N^2 - \frac{(F_x^t(K) + F_x^n(K))}{G(K)}\right]\left[\frac{[G(K)]^2}{[G(K)]^2 + M(K)}\right] - 2\bar{C}_N^2 + \frac{F_x^t(K)}{G(K)}\right]^2 dK \quad . \qquad (7.29)$$

Putting (7.29) over a common denominator and performing the appropriate cancellations leaves

$$\varepsilon = \frac{1}{2\pi} \int_{-\infty}^\infty \frac{\left[-G(K)F_x^n(K) - M(K)[2\bar{C}_N^2 + \frac{F_x^t(K)}{G(K)}]\right]^2}{[[G(K)]^2 + M(K)]^2} dK \, , \qquad (7.30)$$

where the second bracket in the numerator is merely $C_N^{2t}(K)$. Squaring the numerator of (7.30) gives

$$\varepsilon = \frac{1}{2\pi} \int_{-\infty}^\infty \left[\frac{[G(K)F_x^n(K)]^2 + 2M(K)G(K)F_x^n(K)C_N^{2t}(K)}{[[(G(K)]^2 + M(K)]^2} + \frac{[M(K)C_N^{2t}(K)]^2]}{[[(G(K)]^2 + M(K)]^2}\right] dK \quad . \qquad (7.31)$$

Jarem notes that the middle term,

$$\frac{2M(K)G(K)F_x^{n}(K)C_N^{2t}(K)}{[[G(K)]^2 + M(K)]^2} = 0 \quad ,$$

since the noise spectra, $F_x^{n}(K)$ and the signal $C_N^{2t}(K)$ are produced by uncorrelated processes. Hence, the error becomes

$$\varepsilon = \frac{1}{2\pi} \int_{-\infty}^{\infty} \left[\frac{[G(K)F_x^{n}(K)]^2 + [M(K)C_N^{2t}(K)]^2}{[[G(K)]^2 + M(K)]^2} \right] dK \quad . \quad (7.32)$$

We want to construct M(K) so that the error is minimized. This implies that the derivative of the error functional with respect to M(K) vanishes or

$$\frac{d\varepsilon}{dM(K)} = 0 \quad . \quad (7.33)$$

After performing the differentiation, we find that the minimizing M(K) is given by

$$M(K) = \left[\frac{F_x^{n}(K)}{C_N^{2t}(K)} \right]^2 \quad . \quad (7.34)$$

Since our noise process is white, $F_x^{n}(K)$ can be approximated by a constant N. Jarem makes an assumption about $C_N^{2t}(K)$

that is invalid for vertical soundings. His data is along a 2 km horizontal path. Hence, $C_N^{2t}(z)$ is basically a constant making $C_N^{2t}(K)$ behave as

$$\frac{A \sin K}{K} \quad .$$

Substituting back into (7.34) gives

$$M(K) = \frac{N^2 K^2}{A^2 \sin^2 K} \quad .$$

The average value of $\sin^2 K$ is 1/2 making M(K)

$$M(K) = \alpha K^2 \quad , \tag{7.35}$$

where

$$\alpha = \frac{2N^2}{A^2} \quad . \tag{7.36}$$

This corresponds to a stabilizer of order p = 1 and represents an optimal Wiener filter. It is interesting to note that M(K) is completely independent of the aperture.

For vertical paths, $C_N^{2t}(z)$ varies over five orders of magnitude. Hence, the assumption of a constant $C_N^{2t}(z)$ is not valid. However, it does represent a first order

approximation and is a starting point for numerical simulation. If problems occur in the inversion, one can model $C_N^{2t}(z)$ as an exponential decreasing in z, giving a new smoothing function M(K). Therefore, we have two stabilizers of order p = 1 and p = 1/2 to attempt successful inversion.

For Jarem's inversions, he finds that the regularization parameter, α, is nominally 10^{-10} for the horizontal paths. Chapter VIII investigates this inversion technique on the 500 m vertical resolution data of Good shown in Figure 3.2. But before moving on to the simulations, I will investigate two analytical results that we will find convenient.

In (7.14), the z integration can be completed analytically. First, interchanging the K and z integrations gives

$$B_x(\rho) = \frac{1}{\pi} \int_0^\infty dK G(K) J_0(aK^{1/2}\rho) \int_{-\infty}^{\infty} dz C_N^2(z) \sin^2\left(\frac{K^2 z}{2}\right) . \tag{7.37}$$

After completing the z integral, we have

$$B_x(\rho) = \frac{1}{\pi} \int_0^\infty dK G(K) J_0(aK^{1/2}\rho) [2\overline{C}_N^2 - C_N^2(K)] , \tag{7.38}$$

where the $\sin^2$ term is expanded using the double angle relation as before. For test purposes, it is convenient to input $C_N^2(z)$ as a cosine wave. Hence, $C_N^2(K)$ becomes a delta function giving

$$B_x(\rho) = \frac{1}{\pi} \int_0^\infty dK G(K) J_0(aK^{1/2}\rho)[2\bar{C}_N^2 - \delta(K-K')] \quad . \quad (7.39)$$

If the cosine wave has no offset, $2\bar{C}_N^2$ is zero and the K integral has an analytic result,

$$B_x(\rho) = \frac{1}{\pi} G(K') J_0(aK'^{1/2}\rho) \quad , \quad (7.40)$$

where K' is the wavenumber of the input cosine wave. Thus, (7.40) is an analytical check for softwave.

3. Noise Computations

Detectors in an instrumentation package that measure $B_x(\rho')$ will add shot noise to the signal. From [Ref. 51], the average, rms shot noise current is given by

$$i_N^2(\nu) = 2e\bar{I}\Delta\nu \quad , \quad (7.41)$$

where $\Delta\nu$ is the frequency bandwidth, $\bar{I}$ is the average current from the detector and e is the electron charge. $\bar{I}$

depends on the intensity of the starlight and quantum efficiency of the detectors. To find the irradiance of a given star on the telescope aperture, we can use the following [Ref. 52] relation,

$$\log \left(\frac{I_1}{I_2}\right) = .4(Mag_1 - Mag_2) \quad , \tag{7.42}$$

where I_1, I_2 are the stellar intensities on earth and Mag_1 and Mag_2 are the magnitudes of the different stars. Using the sun as a reference, we find that the star α Auriga (Capella) has an irradiance of 1.05×10^{-8} W/m^2 on the telescope for Planck radiation between 0.4-0.6 μm (visible). For the apodized aperture, the detector sees 2.15×10^{-10} W.

The quantum efficiency is [Ref. 53]

$$Q.E. = \frac{n_e^-}{n_q} \quad , \tag{7.43}$$

where n_e- is the number of photoelectrons emitted by the detector/second and n_q is the number of incident quanta/second on the detector. Hence, n_q can be found using the following relation,

$$n_q = \frac{P}{h\nu} \quad , \tag{7.44}$$

where P is the power/wavelength interval of the starlight on the detector, h is Planck's constant and ν is the frequency of the incident light. For the illustration of Capella, n_q is 5.4×10^8 quanta/second given $\lambda = 500$ nm. If we consider a detector with a quantum efficiency of 10%, $\bar{I}$ is 8.66×10^{-12} A. Hence, the variance of the current due to shot noise is 1.39×10^{-27} A^2 given a bandwidth of 500 kHz. Thus, we can construct a theoretical signal-to-noise ratio given by

$$SNR = \frac{\bar{I}}{i_n} = \frac{8.66 \times 10^{-12}}{3.72 \times 10^{-14}} = 232.63 \quad . \qquad (7.45)$$

We can use this figure for constructing Gaussian white noise in Chapter VIII. As pointed out earlier, the shot noise increases with $\bar{I}^{1/2}$. Since the signal is proportional to the intensity, the signal-to-noise ratio increases with $\bar{I}^{1/2}$.

4. Inversion Conclusions

The derivation of sections 1 and 2 is completely general in terms of the receiver apertures. Hence, the receiver apertures can be apodized to optimize inversion performance. We hope that the additional spatial filtering done by the aperture averaging will aid in regularizing the ill-posed nature of the inversion process.

VIII. NUMERICAL SIMULATION OF THE AMPLITUDE COVARIANCE FUNCTION INVERSION WITH TIKHONOV REGULARIZATION

In this chapter, we hope to see if C_n^2 profiling by direct inversion of the scintillation amplitude covariance function with Tikhonov regularization is a practical measurement technique. We can accomplish this by numerically modeling the inversion process using the C_n^2 balloon data of Good presented previously. From this data, I construct the covariance function and use Tikhonov regularization to invert the covariance function regaining the original data. What follows is a step-by-step analysis of the numerical simulation.

A. CONSTRUCTING THE C_N^2 AND SCINTILLATION SPECTRA

The first step in obtaining $C_N^2(K)$ is to transform Good's data into the dimensionless set of variables described in Chapter VII. We accomplish this by applying (7.11b) obtaining $C_N^2(z)$ from $C_N^2(z')$. $C_N^2(K)$ is simply the Fourier transform of $C_N^2(z)$. For this test, the path length L is 31.5 km representing the first 63 points of the known C_N^2 profile (500 m to 31.5 km). I obtained the value of C_N^2 at the surface by assuming the -4/3 dependence of C_N^2 at low altitudes described in Chapter IV. Since the balloon data has a vertical resolution of 500 m, $\Delta z = 0.0159$. The spatial

frequency resolution of the Fast Fourier Transform (FFT) is given by [Ref. 54] as

$$\Delta K = \frac{1}{N \Delta z}$$

where N is the number of data points. Hence, ΔK is 0.9843. (We should remember that K and z are dimensionless variables.) The value of ΔK implies that $C_N^2(K)$ should span zero to 63. However, FFT's are based on the Nyquist criteria, [Ref. 55] that requires two points per Δz interval. Therefore, half the frequencies in the FFT are duplicates, implying that K spans zero to 31.5.

The analysis in Chapter VII requires that C_N^2 be an even function. This is convenient since the Fourier transform of an even function is real. Figure 8.1 shows the real part of $C_N^2(K)$. The modulus of $C_N^2(K)$ is simply the absolute value of the real part since the imaginary part is zero. We obtain the scintillation spectrum $F_x(K)$ by applying (7.16).

It is interesting to note that the FFT is very robust in the presence of noise. Using an algorithm from [Ref. 56], I injected Gaussian white noise with poorer signal-to-noise than that described in Chapter VIII, into the real and imaginary parts of $C_N^2(K)$. The real part of $C_N^2(K)$ with noise is shown in Figure 8.2. If we inverse FFT $C_N^2(K)$ with noise, we obtain the $C_N^2(z)$ profile in Figure 8.3. The

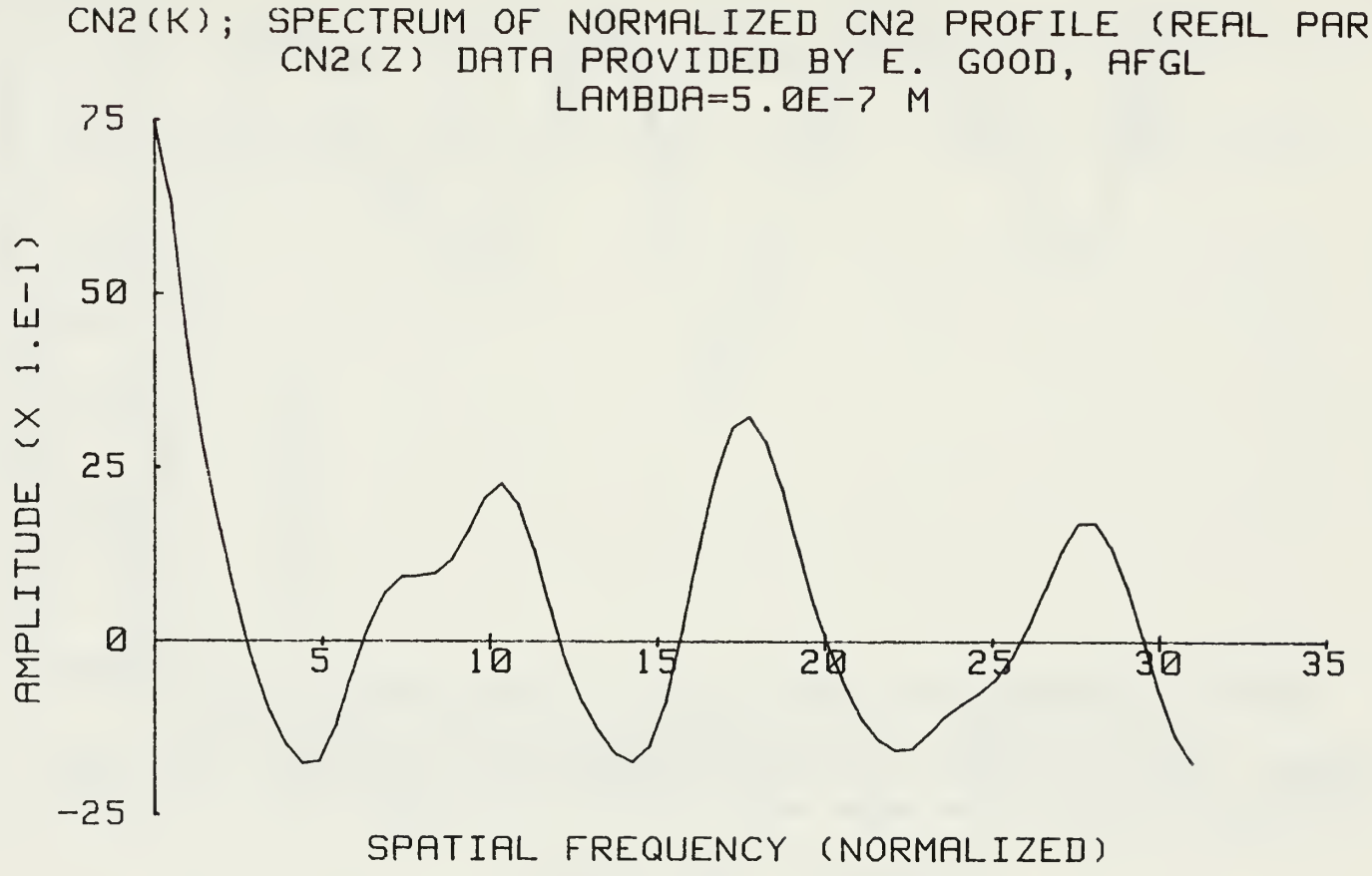

Figure 8.1 The Real Part of the $C_N^2(K)$ Spectrum

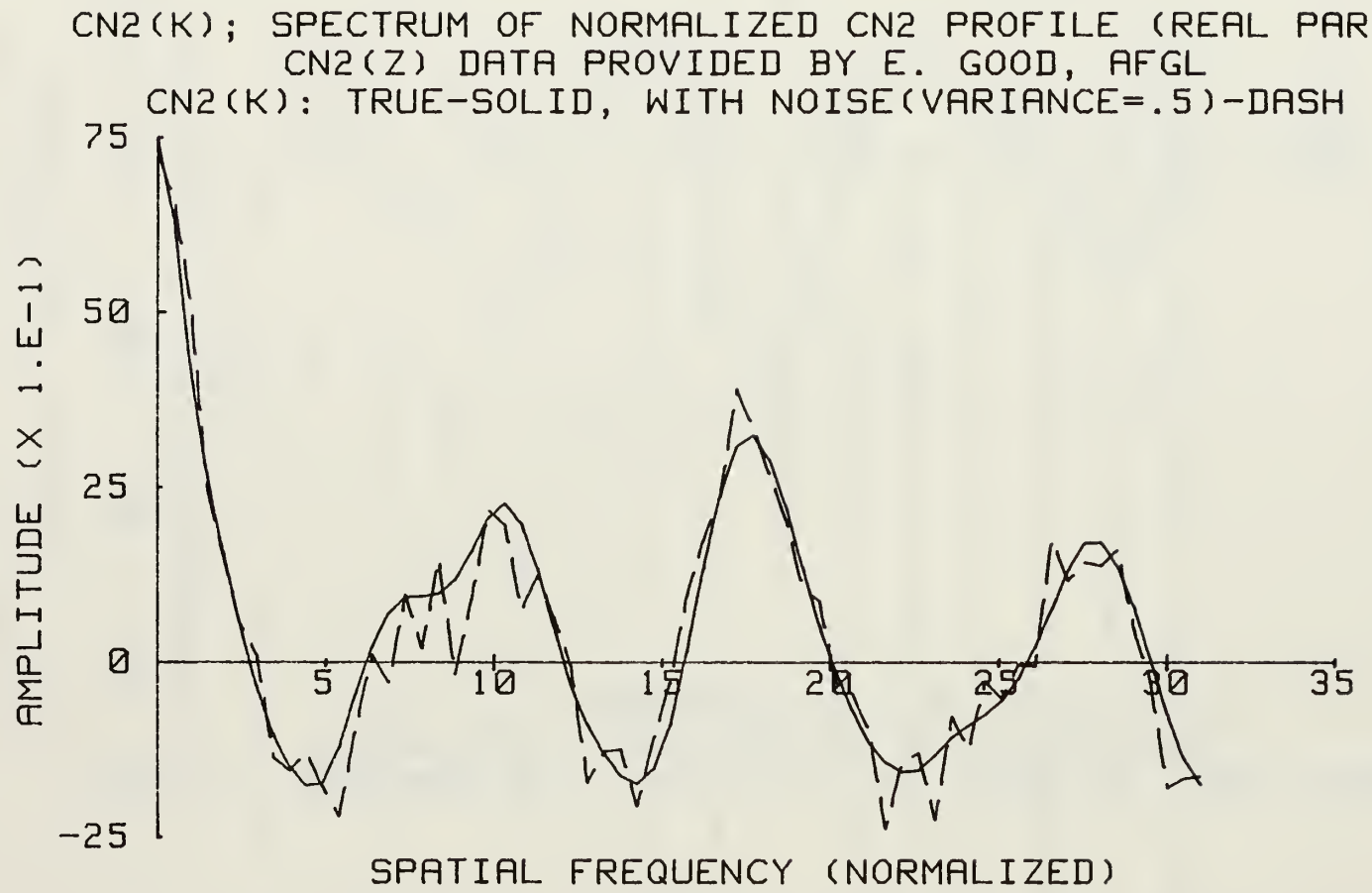

Figure 8.2 The Real Part of the $C_N^2(K)$ Spectrum with and without Noise

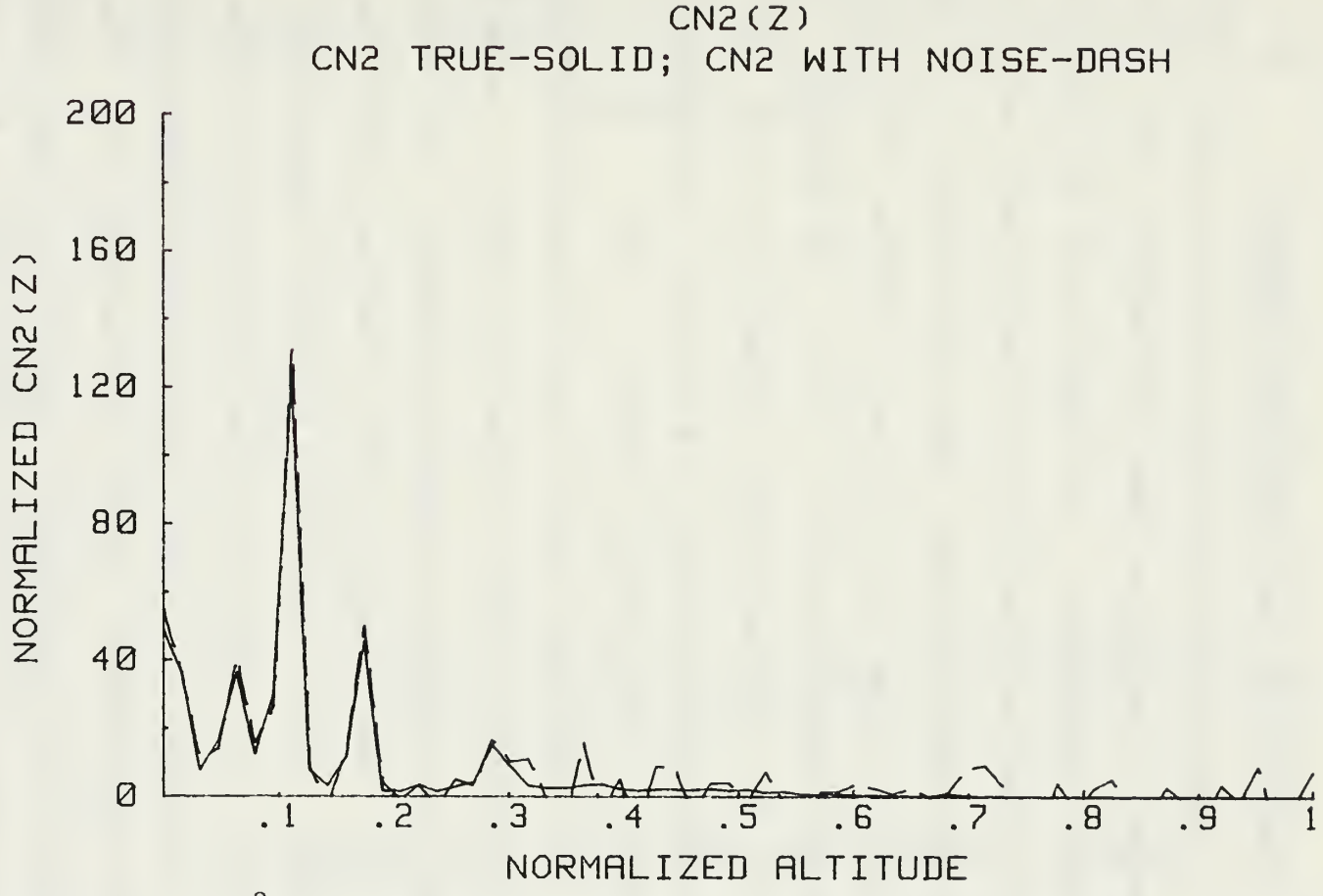

Figure 8.3 $C_N^2(z)$ Profiles Inverse Fourier Transformed with and without Noise

noise has very little affect on the transform. We will find that very small amounts of noise produce drastic results in the inversion of the covariance equation.

B. CONSTRUCTING THE COVARIANCE FUNCTION

I determine the covariance function using (7.38). The numerical integration uses the Trapezoid rule at each detector separation ρ. We should note that the Trapezoid rule integrates functions with noise quite well since it does not require higher order derivatives in the data. Figure 8.4 shows the covariance function for a maximum detector separation of d = 0.5 m. The detector optics have a "top hat" aperture with a diameter of 1 cm. The form of the covariance function in Figure 8.4 is consistent with theoretical calculations [Refs. 6, 15].

The analytical form of the covariance function for a delta function $C_N^2(K)$ is given by (7.40). I used this to check the covariance function software. The relative error is .02. Hence, the covariance function calculations have "noise" (errors) due to the numerical computations. We will use this as a source of noise for ill-conditioning.

We should note that the covariance function has the proper dependence on optics aperture size and electromagnetic wave wavelength. Figure 8.5 is the dependence of the covariance function on aperture size. As expected, the covariance function becomes wider with larger apertures.

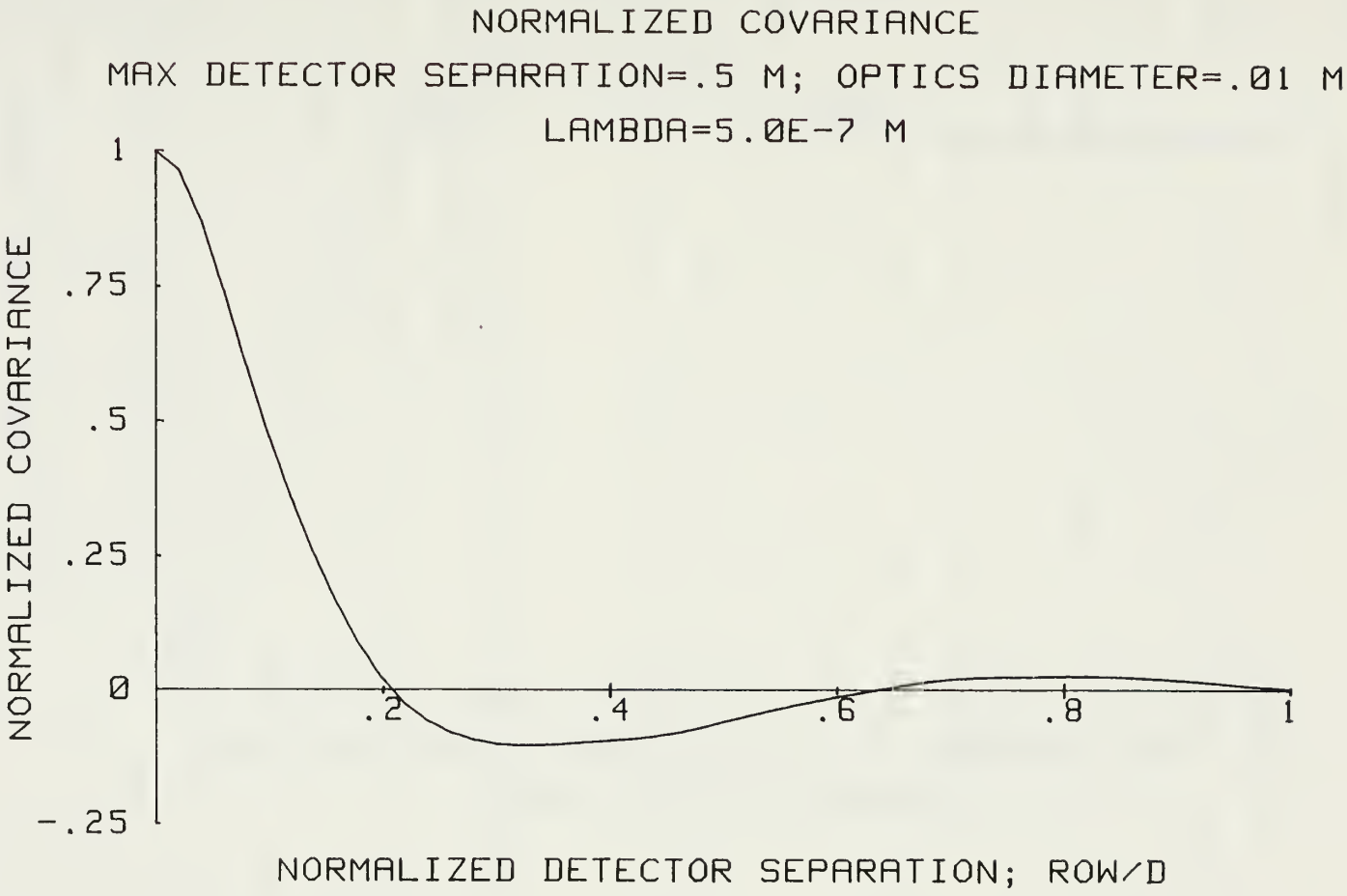

Figure 8.4 The Normalized Scintillation Amplitude Covariance Function

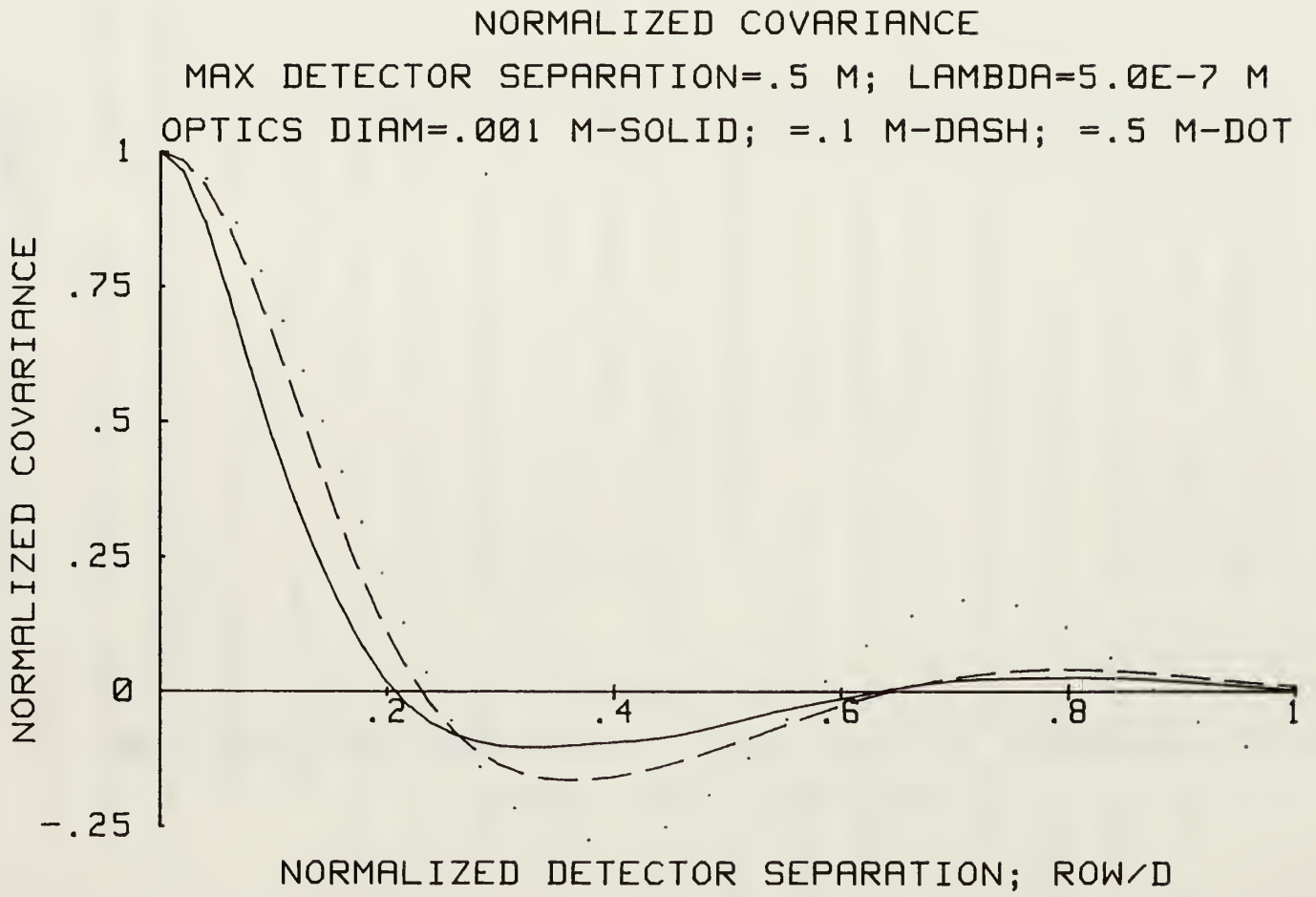

Figure 8.5 Covariance Function Dependence on Receiver Optics Aperture Size

This is predicted by the transform properties involved. Figure 8.6 shows that the covariance function widens for increasing wavelength.

In a C_N^2 profiling system based on this technique, we would measure the intensity covariance function. Hence, the covariance function is the starting point for inversion to obtain the C_N^2 profile. The following sections describe the data manipulations required for an actual measurement system. It is interesting to note that experimental covariance function measurements of laser beam scintillation do not have the negative portion that represents the correlation of maxima and minima in the scintillation pattern [Ref. 28]. This may be due to the fact that the photomultipliers measure a positive definite quantity (i.e., intensity).

C. CONSTRUCTING THE SCINTILLATION SPECTRUM AND APPLYING TIKHONOV REGULARIZATION

The scintillation spectrum $F_x(K)$ is the Hankel transform of the covariance function. The dimensionless form of the transform is given by (7.15). $C_N^2(K)$ is found by (7.16). To compensate for the ill-conditioning present, we introduce a low pass filter of the form given in (7.23). This is the Tikhonov regularization. Figure 8.7 shows $C_N^2(K)$ after the regularization with a stabilizer of the form αK^3. Note the affect of the filter on the higher spatial frequencies.

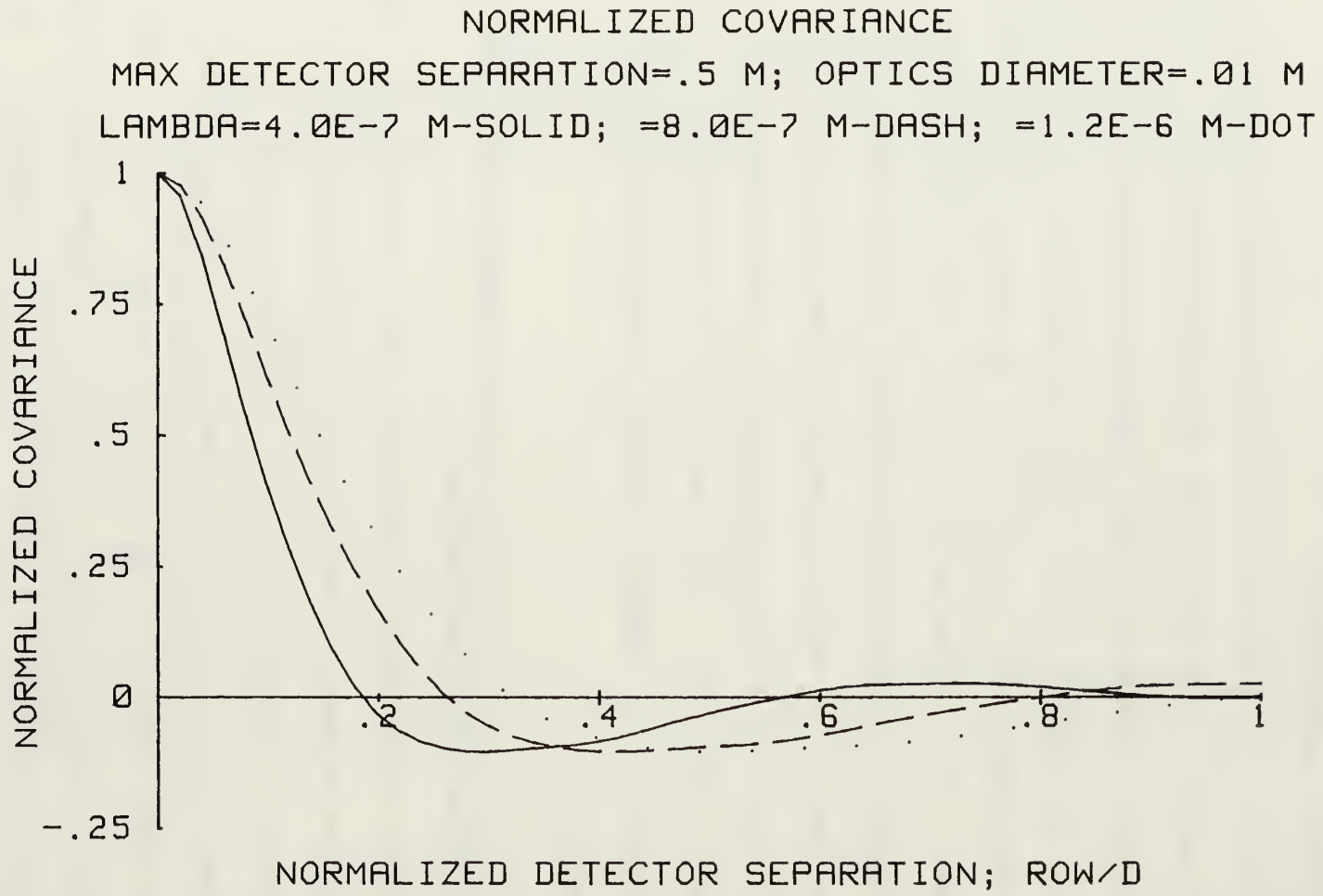

Figure 8.6 Covariance Function Dependence on the Wavelength of the Incident Electromagnetic Radiation

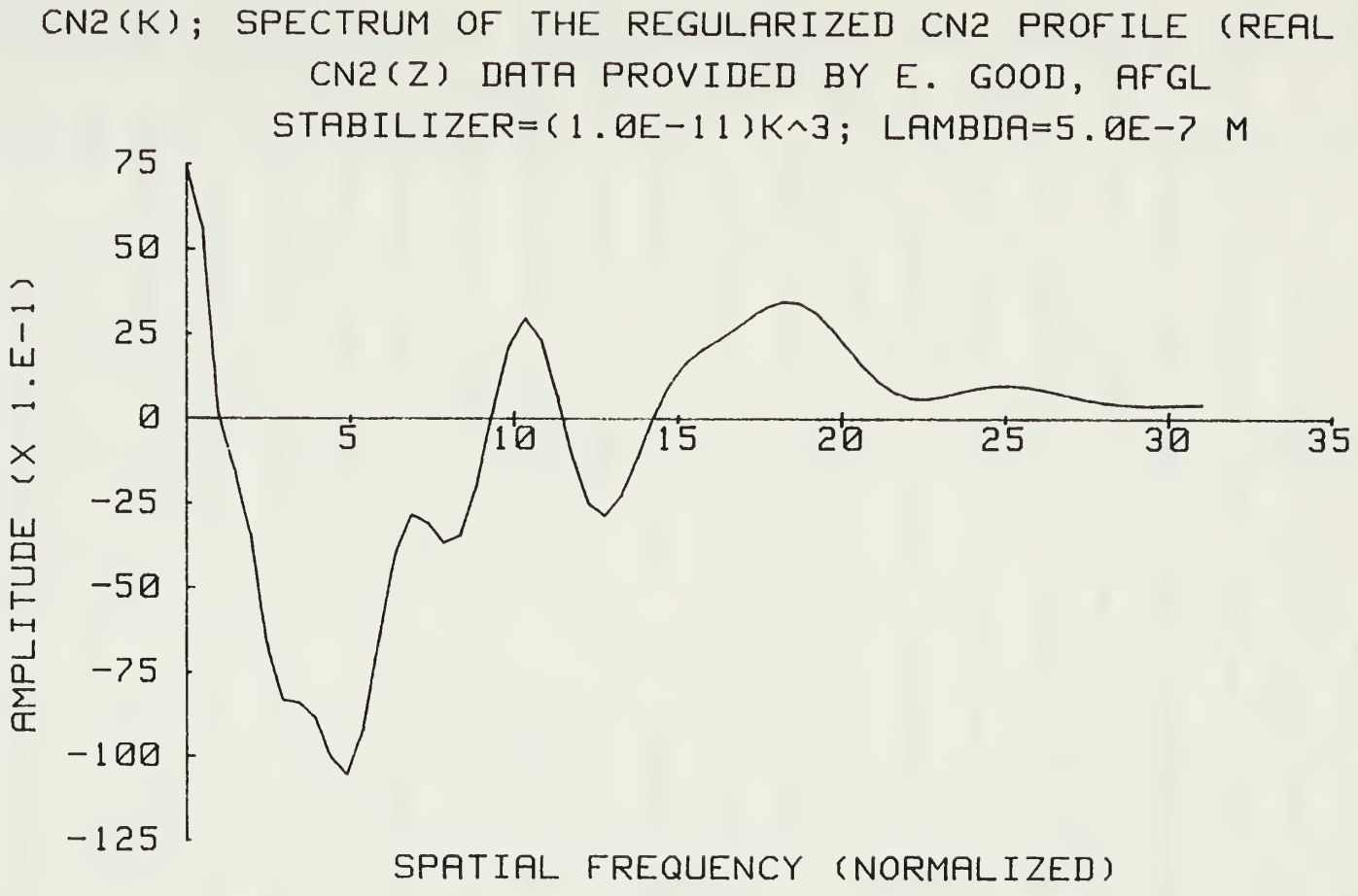

Figure 8.7 $C_N^2(K)$ Constructed From the Covariance Function with Tikhonov Regularization

Figure 8.8 shows how $C_N^2(K)$ changes with stabilizers of different powers of K. We obtain $C_N^2(z)$ by inverse FFT.

Figure 8.9 shows the true $C_N^2(z)$ profile, unregularized solution and regularized solution with $\alpha = 1 \times 10^{-11}$ and a K^3 stabilizer. Remember that α determines the amount of ill-conditioning allowed to enter the solution. The unregularized solution (dots) bears no resemblence to the original $C_N^2(z)$ profile. The regularized profile with $\alpha = 1 \times 10^{-11}$ does very well resolving much of the 500 m resolution structure present in the actual data. The small "hump" in the regularized solution after the real data has gone to zero is part of the ill-conditioning. Note that the regularized solution has problems near zero. It in fact becomes negative (not shown) which is unphysical. This is very likely due to the frequency truncation. Consider a "top hat" aperture. We can Hankel transform the "top hat" to obtain the Airy spectrum. Hankel transforming back to aperture coordinates produces an oscillation in the original aperture function, Figure 8.10. This is due to frequency truncation. This same truncation occurs in our calculation of the covariance function and C_N^2 spectrum. Hence, an induced oscillation in $C_N^2(K)$ transforms as the large negative value in the space coordinate, z. The fact that it is negative implies that the oscillation in the spectra is out of phase with the other frequencies present.

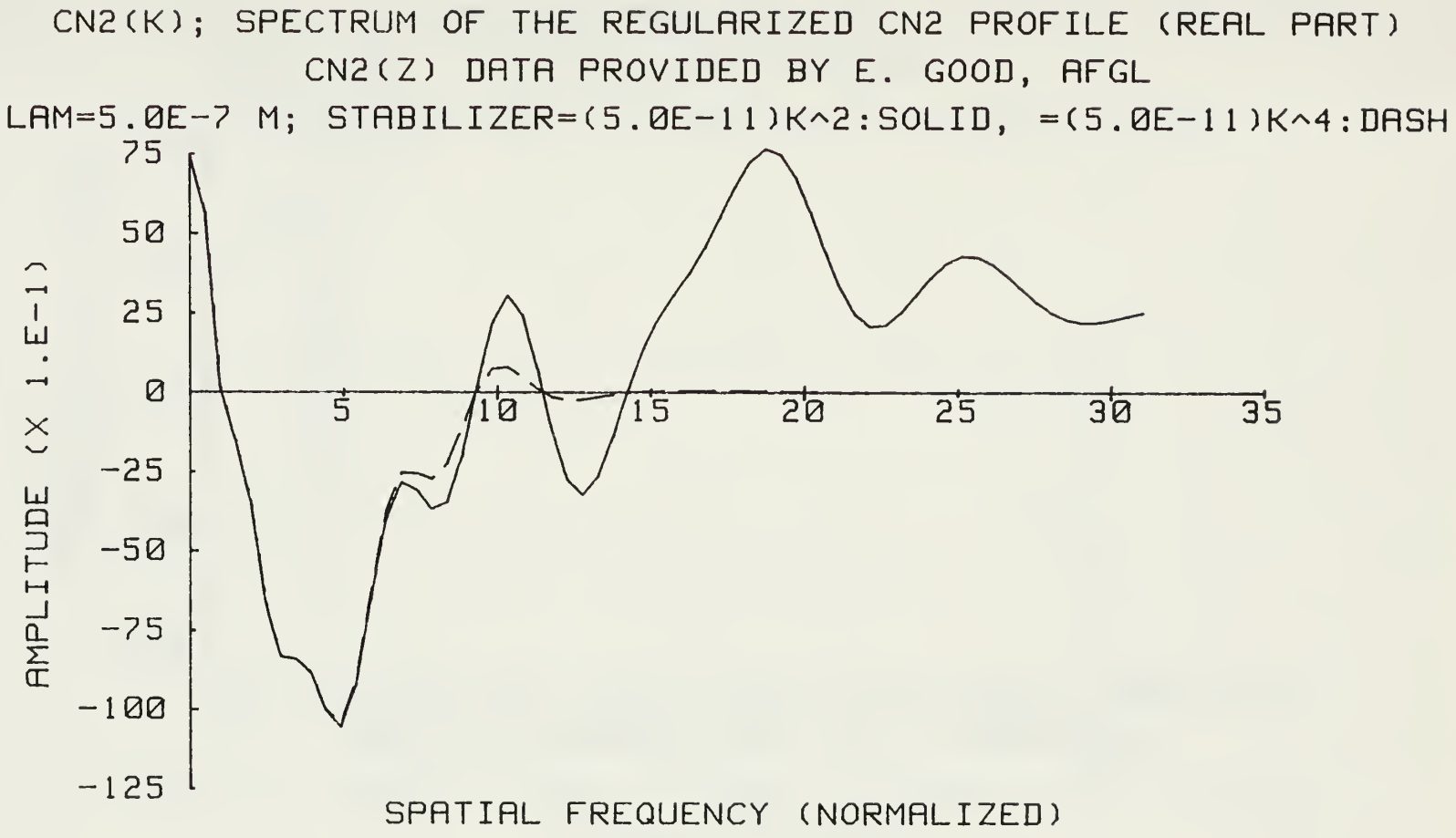

Figure 8.8 $C_N^2(K)$ for Different Stabilizers

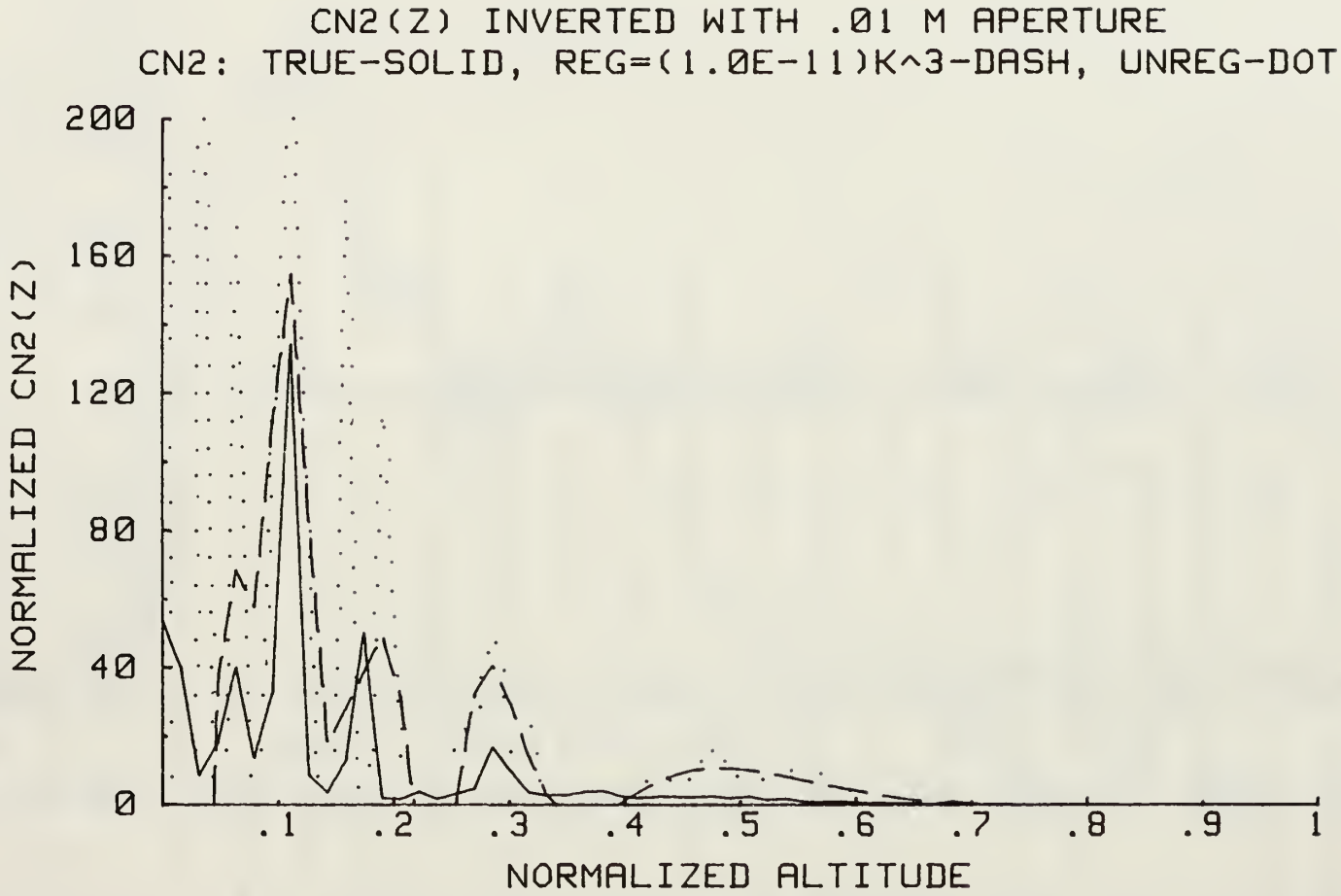

Figure 8.9 $C_N^2(z)$ for Regularized, Unregularized and the Actual Profile

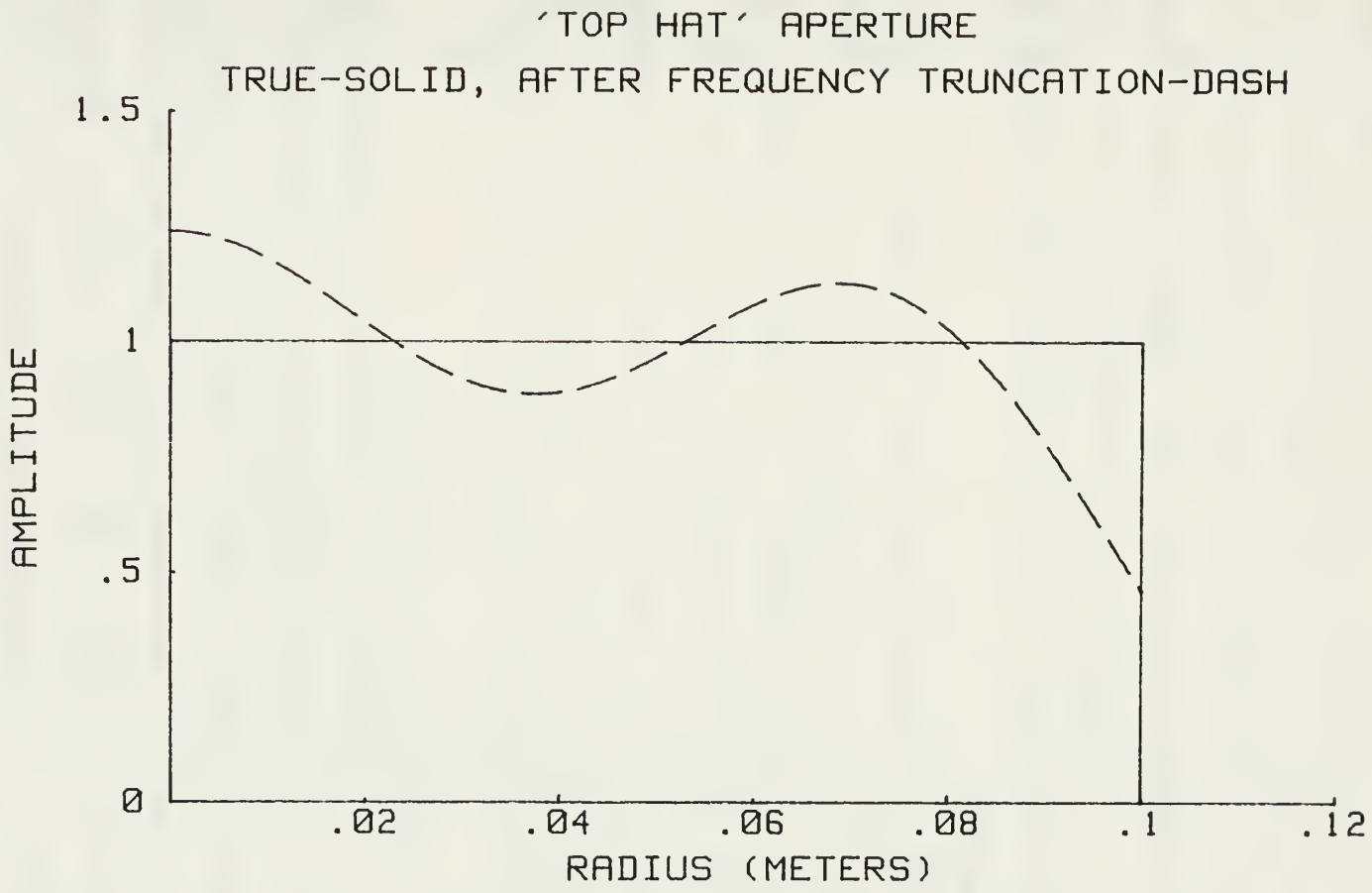

Figure 8.10 Effect of Frequency Truncation on the "Top Hat" Aperture

Lowering the regularization parameter α allows more of the ill-posed nature of the problem into the solution. Figure 8.11 shows the true solution and regularized solutions with $\alpha = 1 \times 10^{-9}$ and 1×10^{-13} for a K^3 stabilizer. Clearly, the choice of α is a trade-off between structure and magnitude accuracy. The aperture averaging does in fact filter the higher spatial frequencies, however manipulating α produces more favorable results than changing the optics diameter.

It is interesting to note the affect on $C_N^2(z)$ for stabilizers with different powers of K and the same regularization constant, α. Figure 8.12 shows $C_N^2(z)$ for K^2, K^3 and K^4 stabilizers all with $\alpha = 1.0 \times 10^{-11}$. In Chapter VII, we found that K^2 stabilizers correspond to the optimal Wiener filter. From this simulation, I feel that K^3 stabilizers offer the best fit to the C_N^2 profile.

D. REGULARIZATION CONCLUSIONS

Initially, we were interested in whether direct inversion of the covariance function with Tikhonov regularization offered a practical way of obtaining C_N^2 profiles. I have shown that one can obtain high vertical resolution profiles ($\Delta z = 500$ m) with this technique. However, covariance function measurements are very difficult to make. The quality of the measured covariance functions will never be comparable to those calculated numerically in

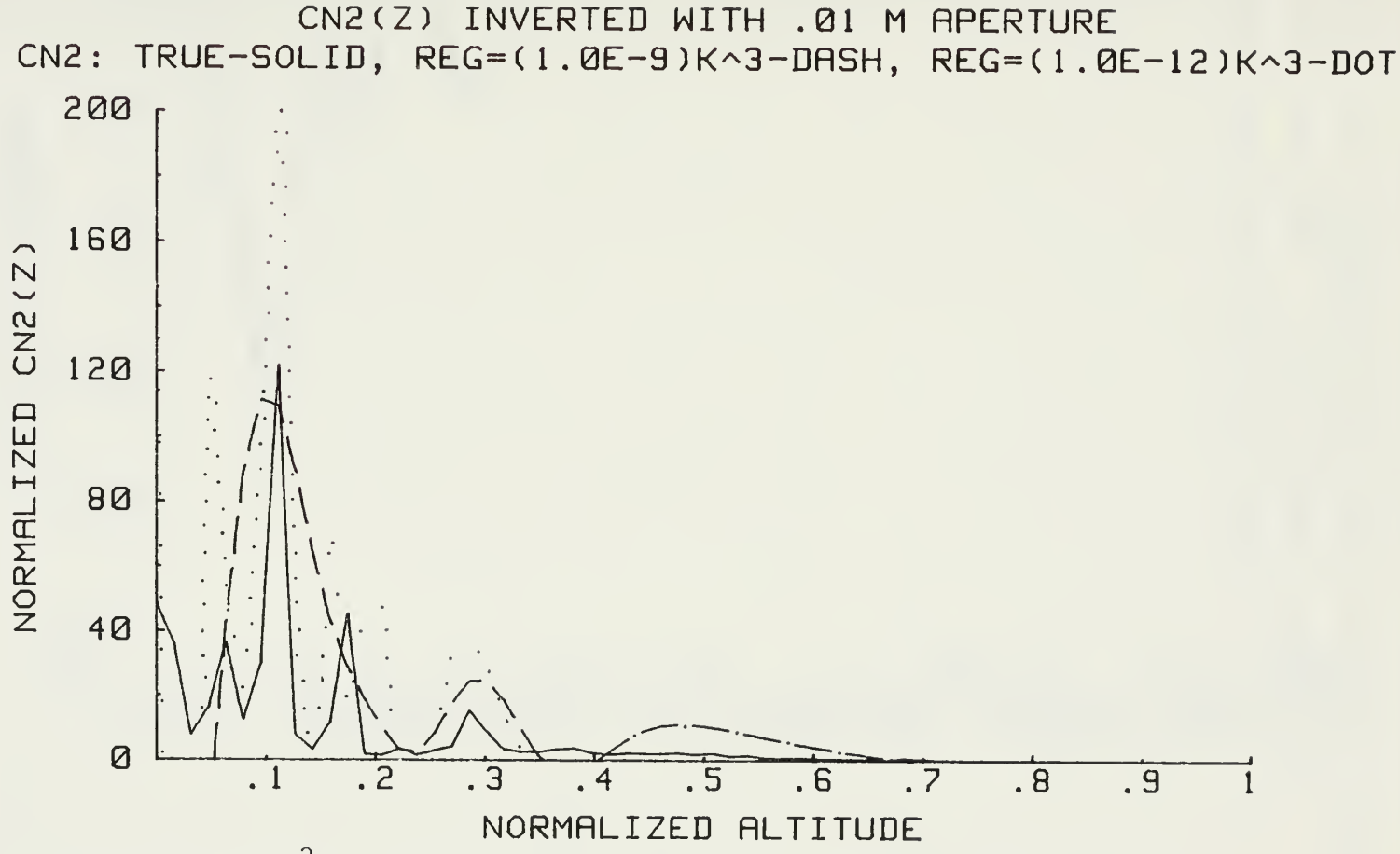

Figure 8.11 $C_N^2(z)$ with Different Regularization Parameters, α

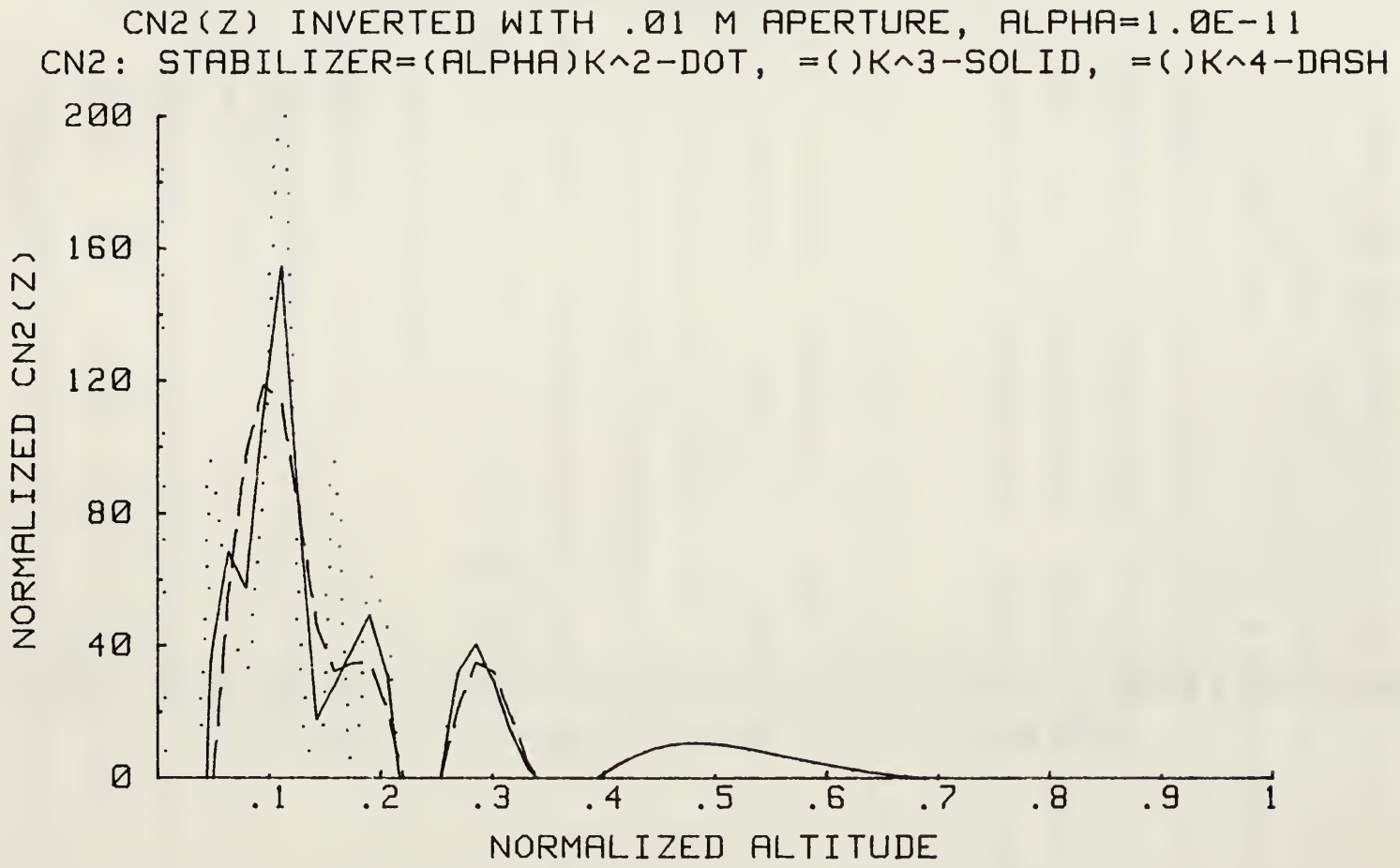

Figure 8.12 $C_N^2(z)$ for Different Stabilizers

this section. Based on this fact alone, I feel that other techniques are more likely to yield accurate, high vertical resolution C_N^2 profiles. I will propose a method for obtaining such profiles in the next chapter.

IX. CONCLUSIONS

The importance of the atmospheric isoplanatic angle and refractive turbulence profiles to the Space Defense Initiative (SDI) cannot be overstated. In this dissertation I have demonstrated an improved isoplanatic angle measurement system and presented a technique to measure refractive turbulence profiles. In the following sections, I will briefly review each area and propose future work.

A. ISOPLANATIC ANGLE MEASUREMENT

We saw that the original Walters isoplanometer could be improved by apodizing the aperture of the receiver telescope. To best approximate the $z^{5/3}$ altitude weighting required for isoplanatic angle measurement, I constructed a double annulus aperture function optimized for a Celestron C8 telescope. The double annulus aperture weighting function is a significant improvement over that of the "top hat" clear aperture used on the previous isoplanometers.

Sensitivity analysis of the double annulus weighting function to strong low altitude turbulence and inner scale changes with altitude showed no effect detrimental to a measurement system. Hence, we fabricated a fourth generation isoplanometer based on the double annulus aperture. This instrument is designed for night use and

offers many advantages over the previous system. First, the double annulus no longer requires the use of the Celestron C14 telescope as did the "top hat" aperture. This is a considerable savings in cost and instrument managability. This instrument also has the ability to make isoplanatic angle measurements once per second giving data with very high temporal resolution. Trends in the isoplanatic angle are emerging now that have never been seen before and indicate that this instrument may be an extremely effective tool to probe the tropopause.

In Chapter V, I detailed tests proving that the instrument is indeed measuring the isoplanatic angle correctly. And lastly, I presented data from Maui showing interesting trends in the isoplanatic angle. Currently, two fourth generation isoplanometers are operating at different locations, supporting high priority programs.

Clearly, the greatest need in the area of isoplanatic angle measurement is a painstaking correlation between the structure observed in isoplanatic angle measurements and meteorological data. One hopes that the isoplanometer might effectively measure turbulence at the tropopause. This would save money in balloon flights, etc.

Also of interest would be to modify the fourth generation system to provide high temporal resolution data during the day. This requires the use of high quality

telescope mounts and drives, but I feel daytime data is well worth the expense.

B. REFRACTIVE TURBULENCE PROFILING

In this section, we investigated the inversion of the scintillation amplitude covariance equation. I included the filtering done by the receiver optics and obtained a closed form solution to the inversion problem. Unfortunately, inverting the covariance function is ill-posed in a mathematical sense, meaning that noise in the data causes an unstable solution. Hence, I incorporated a regularization technique developed by Tikhonov to compensate for the ill-conditioning. Tikhonov regularization is a low pass filter designed to eliminate high spatial frequencies most contaminated by the ill-conditioning.

I modeled the inversion numerically using an actual refractive turbulence profile with 500 m vertical resolution. We saw that the Tikhonov regularization reproduced much of the profiles very well. However, we note that actual covariance function measurements are very difficult to make. Hence, I recommend pursuing the weighting function approach to refractive turbulence profiling described in Chapter VII. One should be able to obtain suitable weighting functions given an appropriate basis set. This would allow refractive turbulence profiling by scintillation intensity variance measurements, operating much like the isoplanometer.

APPENDIX A

OTHER WEIGHTING FUNCTIONS

Many different weighting functions can be generated using the technique mentioned in Chapter III. What follows is a brief overview of the many weighting functions I generated while trying to approximate to the $z^{5/3}$ behavior or find weighting functions that peak at a given z.

First, a few words about the double annulus aperture. In Figure 3.8, we have noted the error remaining at low z. This can be improved by making the inner annulus larger, Figure A.1. However, you sacrifice some performance at larger altitudes. Because of the $z^{5/3}$ weighting for the isoplanometer, we felt error should be minimized at higher z at the expense of low z.

I also tried other combinations of Bessel functions. One is the "wedding cake" aperture function (in my nomenclature), which is composed of two "top hat" functions with different transmissivities, Figure A.2. Typically, the "wedding cake" aperture gave a weighting function of z^2 below 3 km, Figure A.3. Associated with the "wedding cake" is the "three tier" aperture function, which has one more "layer". Weighting function behavior with the "three tier" is basically the same as the "wedding cake".

One can incoherently add spectra of different aperture functions since the correlation distance is so small (on the order of centimeters), given a telescope with a sufficiently large aperture. Using this technique, I was able to make the weighting function bend at a given z, Figure A.4. The weighting function in Figure A.4 is an incoherent addition of the "top hat" and "wedding cake" aperture functions. Weighting functions with this characteristic are also important.

From the Bateman manuscripts, I tried some Hankel transform pairs. If we consider the Hankel transform of f(x), (the spectrum), in the form

$$f(y) = \int_0^\infty f(x)J_0(xy)(xy)^{1/2}dx \qquad (1)$$

the function $x^{-1/2}e^{-ax}$ has the spectrum $y^{1/2}(y^2 + a^2)^{-1/2}$. The exponential aperture function has the weighting function shown in A.5. This weighting function is also on the z^2 side of $z^{5/3}$.

Shown in Figures A.6 and A.7 are the weighting functions associated with sine and cosine spectra. Both have analytical aperture functions that can be found in the Bateman Manuscript [Ref. 34].

This is by no means a complete list of all the apertures I found weighting functions for. However, these are the more interesting and applicable.

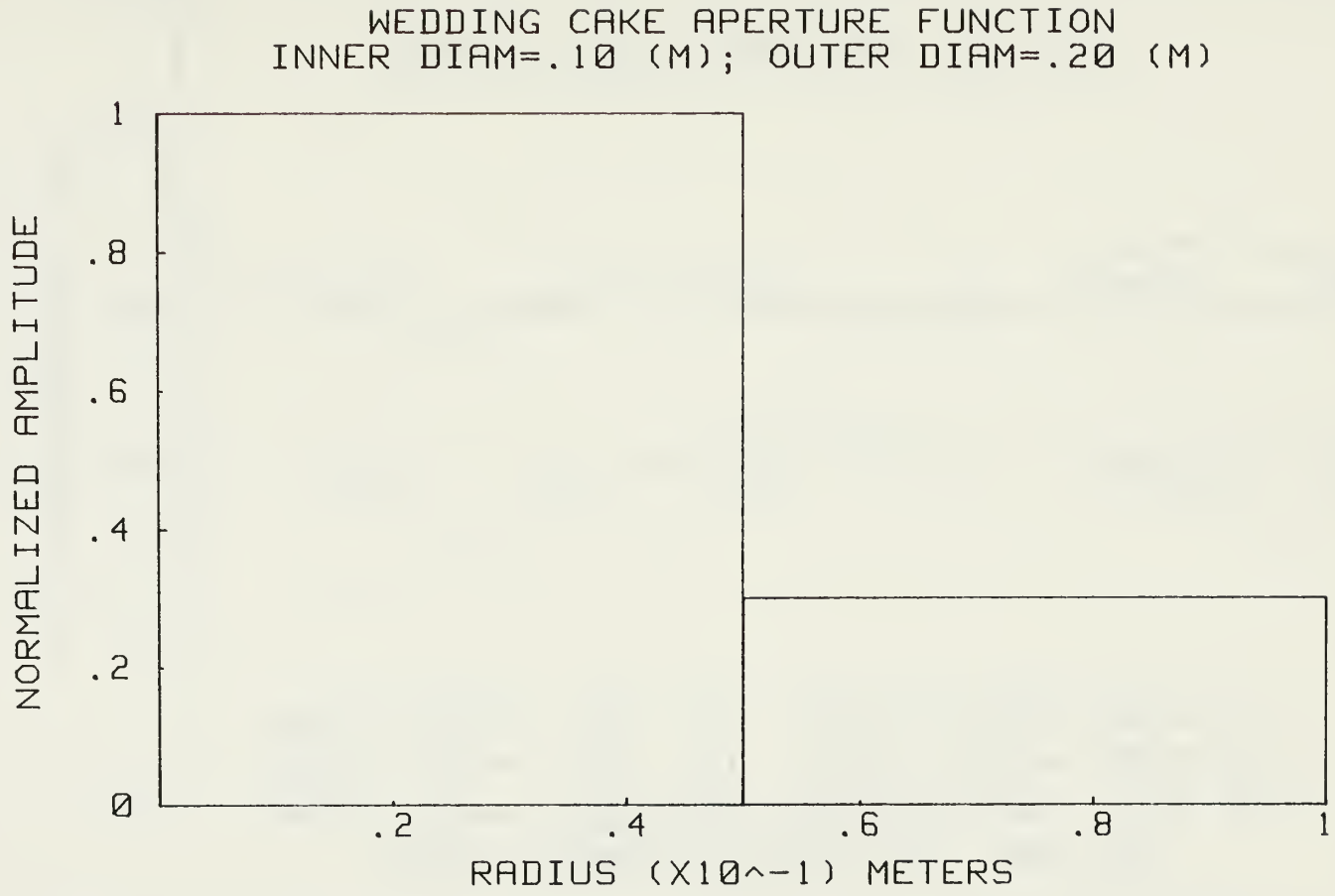

Figure A.1 Wedding Cake Aperture Function

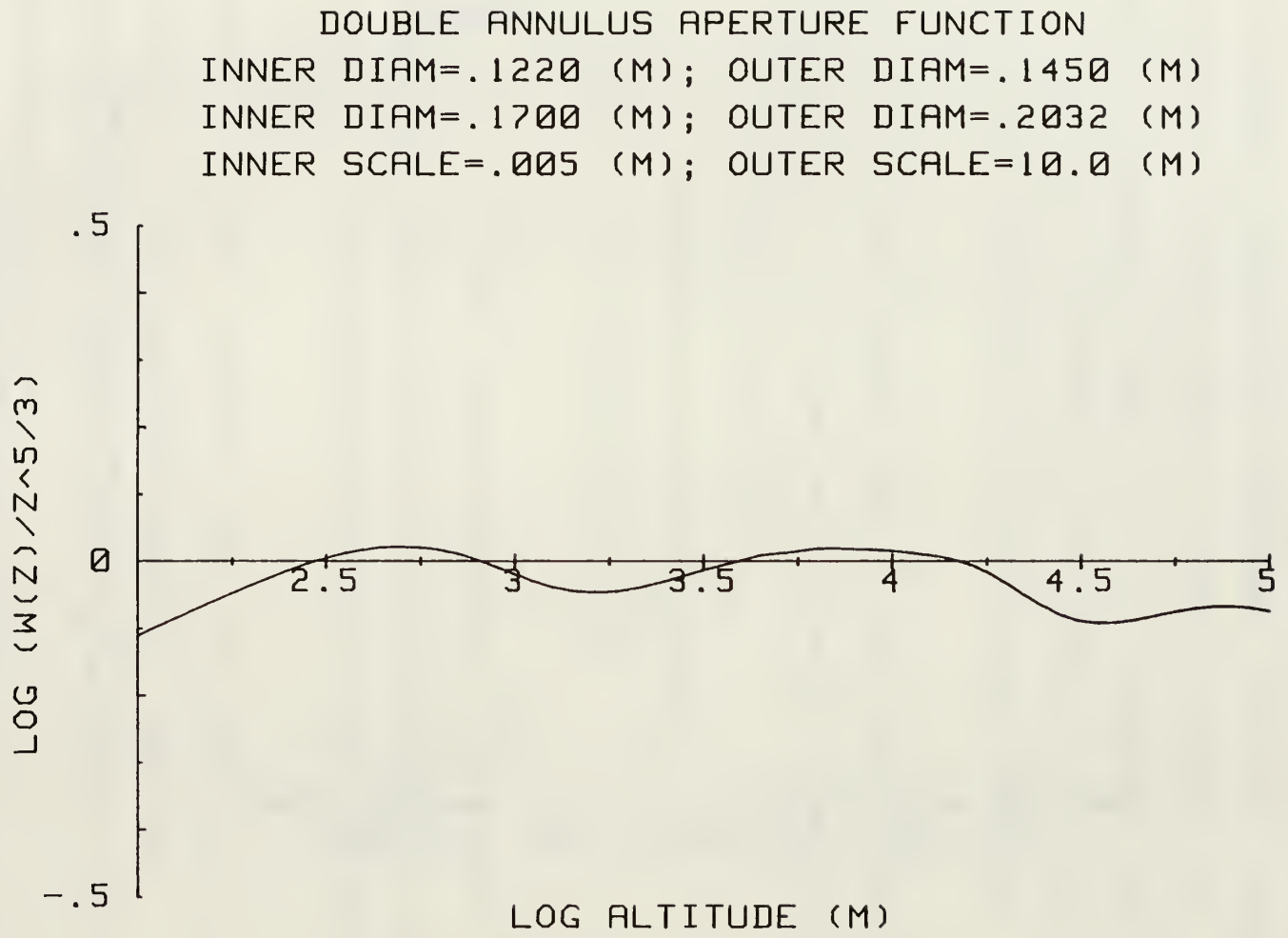

Figure A.2 Error from $Z^{5/3}$ for a Double Annulus Aperture Function

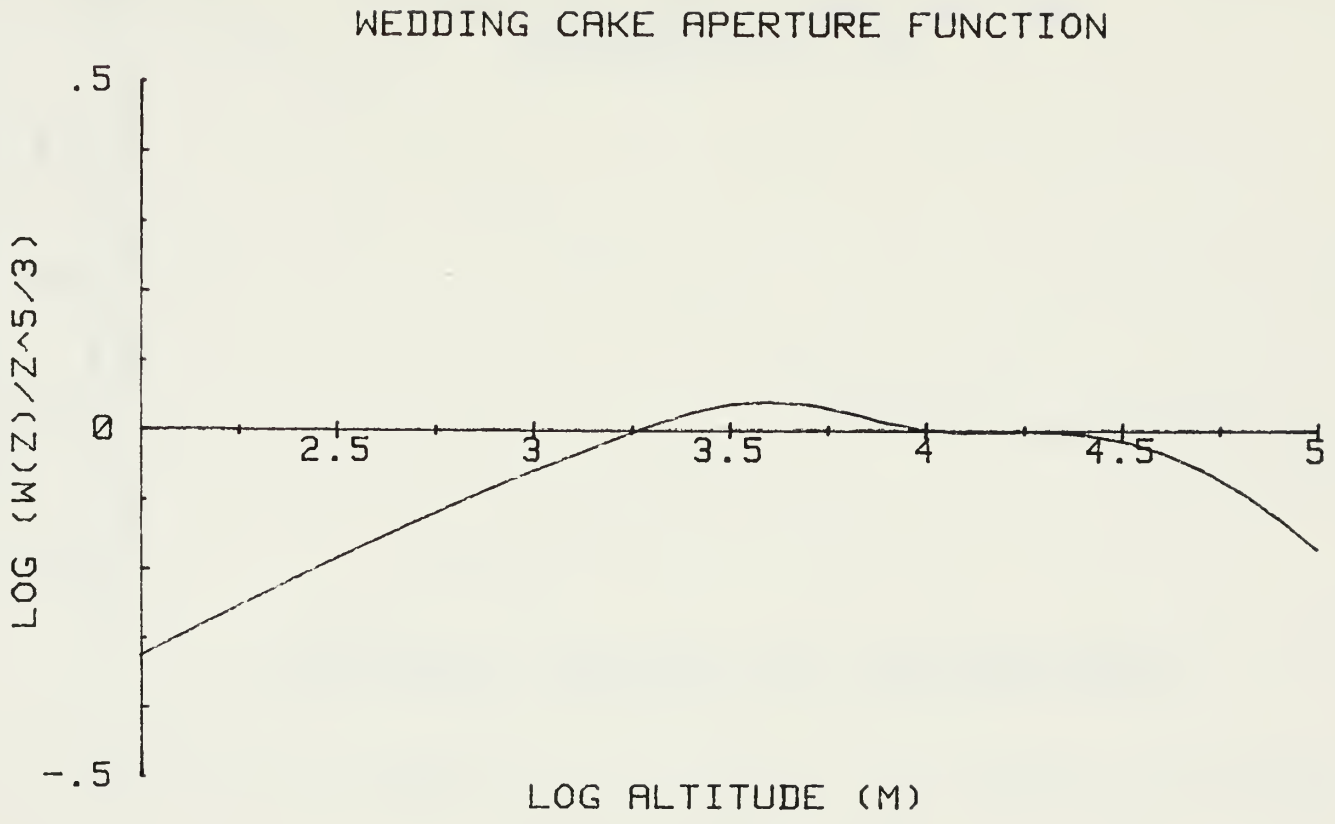

Figure A.3 Error from $z^{5/3}$ for a Wedding Cake Aperture Function

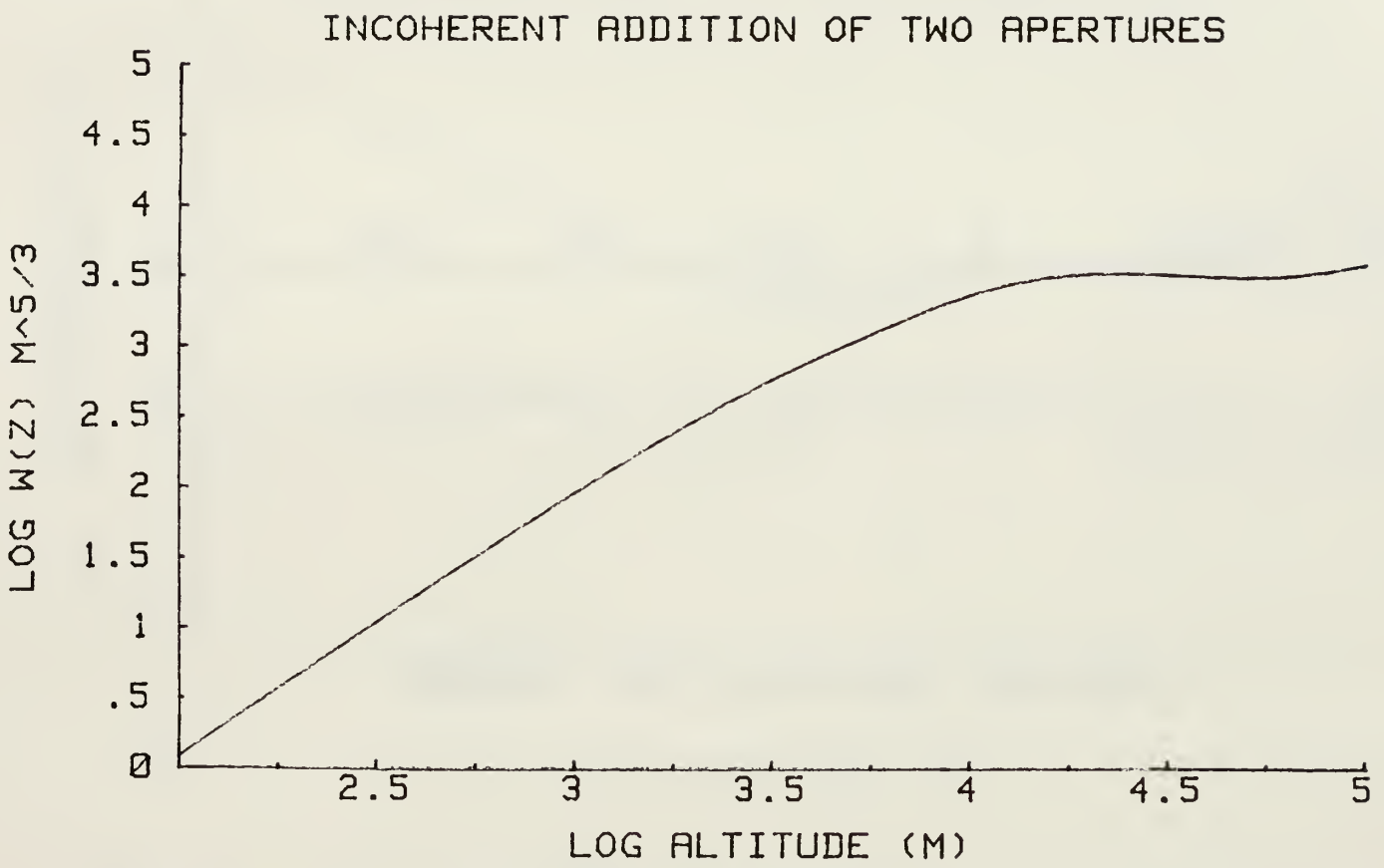

Figure A.4 Weighting Function for Incoherent Addition of Two Apertures

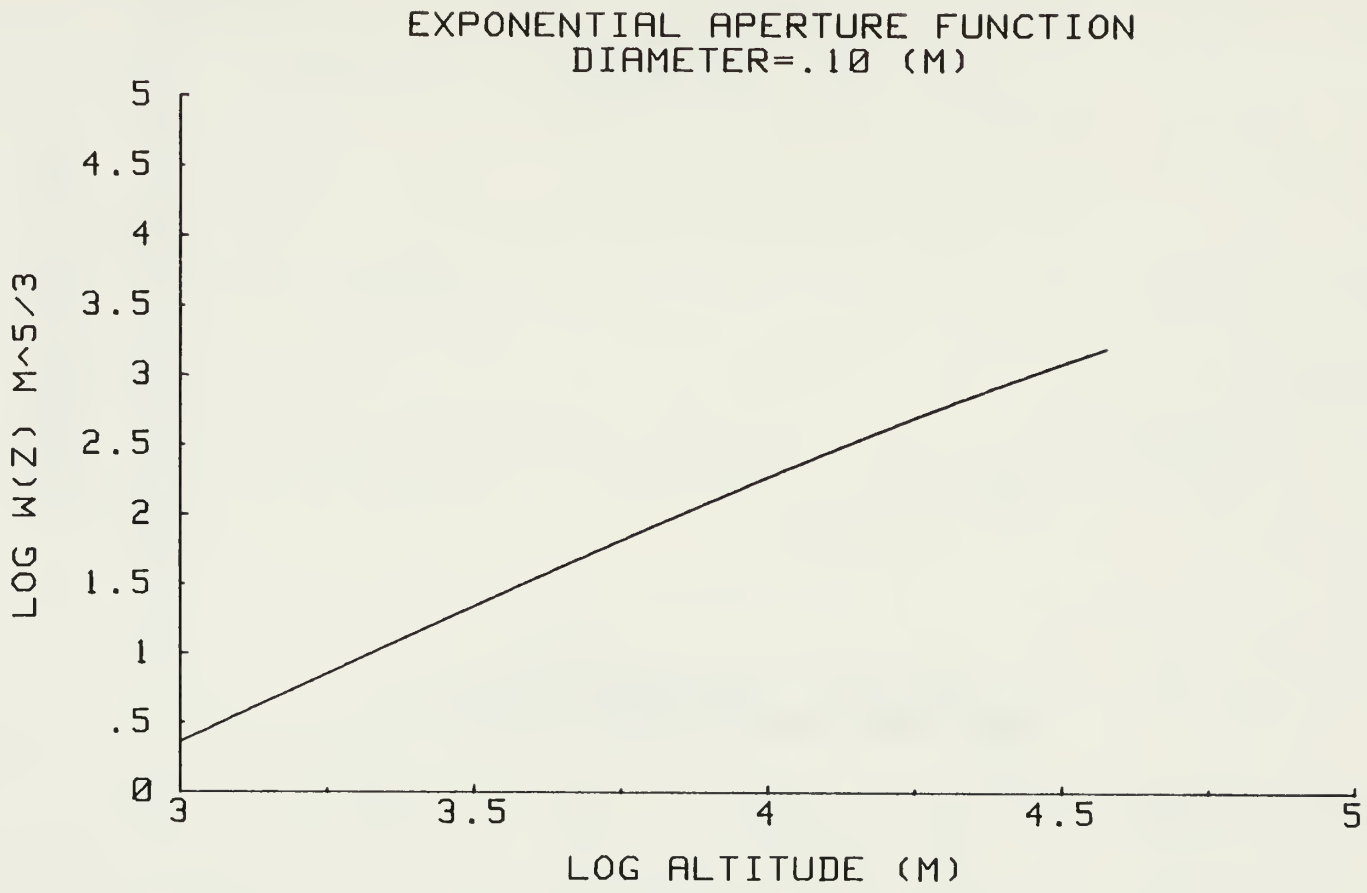

Figure A.5 Weighting Function for an Exponential Aperture Function

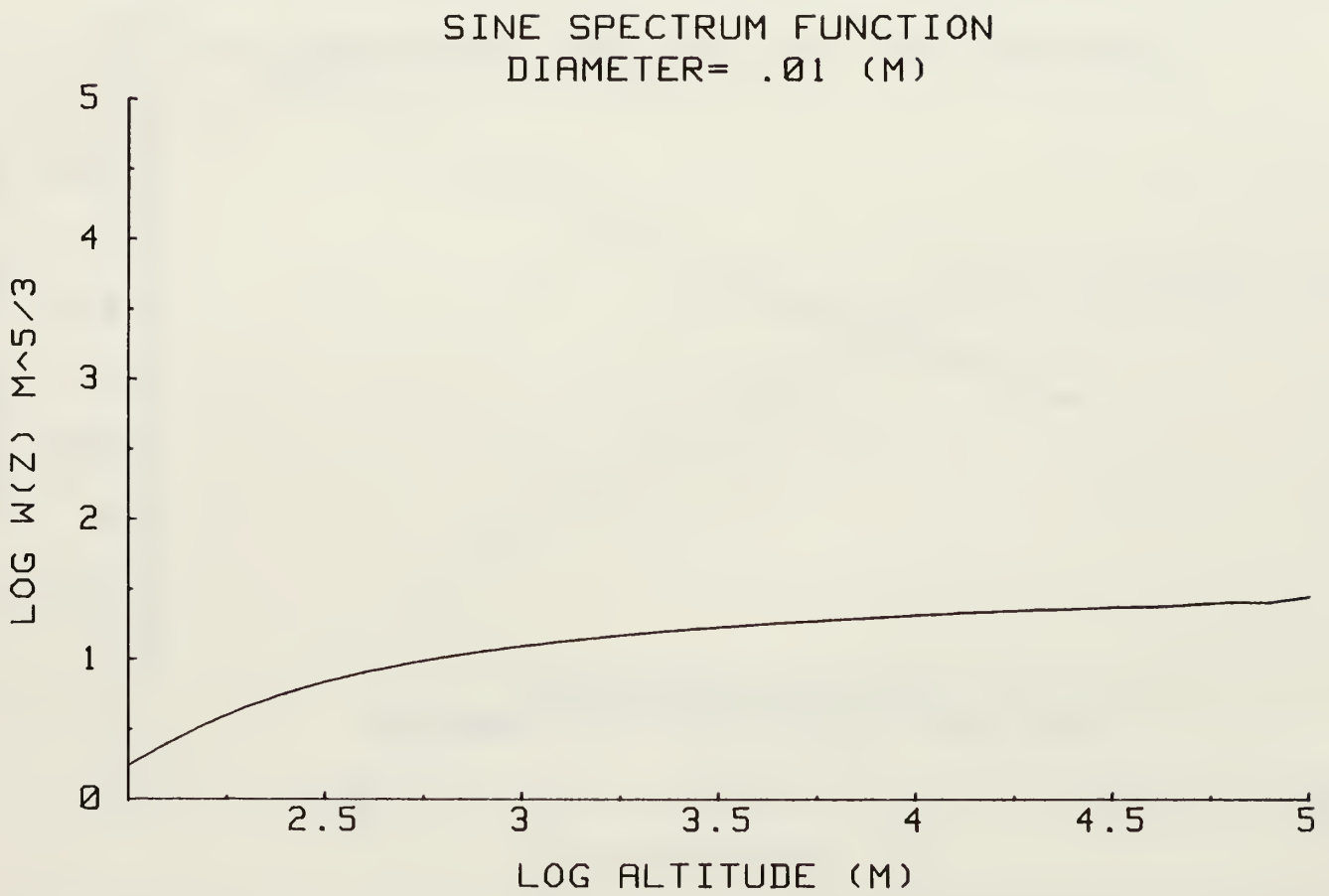

Figure A.6 Weighting Function for a Sine Intensity Spectrum

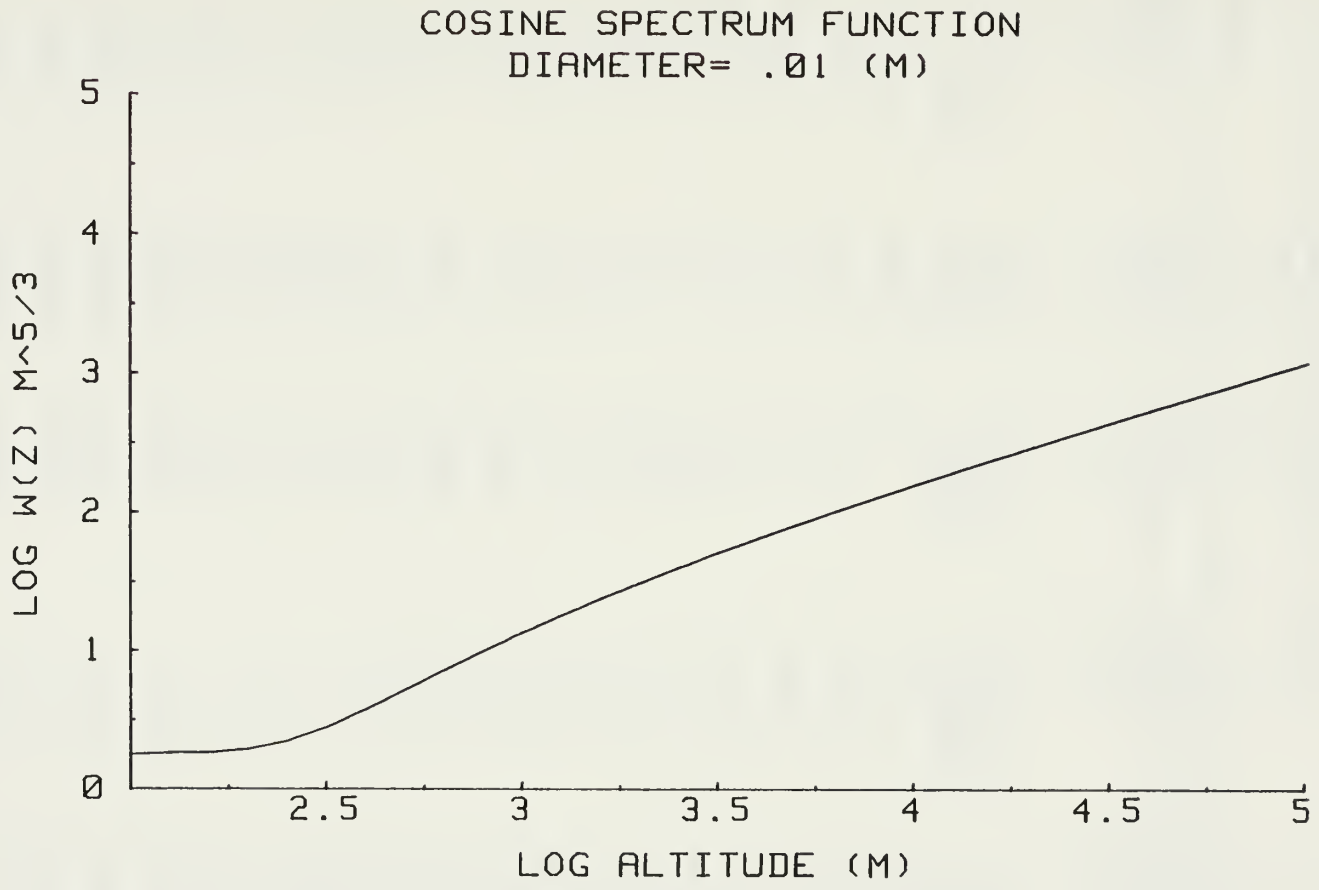

Figure A.7 Weighting Function for a Cosine Intensity Spectrum

APPENDIX B

MAUI METEOROLOGICAL BALLOON DATA

LO-CATE WO-8000 UPPER AIR DATA MANAGEMENT SYSTEM P106277
REV2.11 (C) 1984

DATE(GMT)	TIME(GMT)	ASCENT NO.	FLIGHT EQ.	STATION	SONDE NO.
850917	04:16	17	5	0	6685

TIME MIN.	PRESSURE MBARS	HEIGHT M-MSL	TEMP CEL.	DP-DEP CEL.	RH PERCENT
0.00	711.4	0	12.0	21.1	22.0
0.65	700.0	135	11.2	17.8	28.3
1.73	682.4	348	11.2	14.6	36.2
2.73	659.4	633	9.5	15.0	34.7
4.00	627.7	1038	4.6	12.0	41.7
6.10	577.7	1709	0.0	11.2	42.9**
6.15	576.4	1727	-0.1	11.3	42.6
6.28	573.2	1788	90.8	17.8	46.9
6.35	571.7	1816	-0.3	11.1	43.3
7.80	540.6	2261	-4.1	7.1	57.7
8.75	518.8	2585	-5.5	12.6	36.8
8.82	517.3	2608	-2.7	12.8	37.1
8.88	515.7	2632	-5.9	12.3	37.6
9.67	500.0	2874	-7.3	13.1	34.6
9.88	495.7	2941	-7.9	15.0	29.0
11.40	466.0	3418	-11.6	11.5	38.4
12.80	443.3	3800	-12.6	14.5	28.9
15.55	400.0	4576	-18.4	14.0	28.3
22.23	305.6	6530	-32.5	10.3	35.1
22.65	300.0	6660	-33.5	10.0	35.6
25.73	260.8	7627	-41.6	6.6	47.9

TIME MIN.	PRESSURE MBARS	HEIGHT M-MSL	TEMP CEL.	DP-DEP CEL.	RH PERCENT
26.60	250.0	7913	-43.8	8.4	38.4
27.87	233.8	8359	-47.5	8.1	37.9
29.80	216.1	8876	-50.2	8.2	36.5
31.30	200.0	9377	-54.2	7.9	35.8
34.78	169.1	10427	-65.0	7.0	35.1
36.72	153.2	11022	-70.0	6.6	34.8
37.13	150.0	11147	-70.6	6.5	34.7
37.40	148.0	11227	-71.1	6.5	34.7
38.40	140.6	11531	-70.0	6.6	34.7
38.45	140.1	11554	-26.4	9.8	39.4
38.58	139.0	11606	-70.1	6.6	34.7
40.38	126.9	12143	-73.7	6.3	34.4
43.53	109.0	13029	-74.7	6.2	34.3
44.83	102.3	13396	-76.6	6.0	34.2
45.30	100.0	13527	-76.8	6.0	34.1
45.63	98.4	13620	-76.7	6.0	34.1
48.10	87.4	14310	-72.2	6.4	34.5
52.60	70.0	15633	-67.2	6.8	34.8
54.15	64.9	16092	-65.0	7.0	34.9
56.53	57.5	16830	-65.0	7.0	34.9
58.75	51.6	17495	-62.0	7.3	34.9
59.42	50.0	17690	-61.7	7.4	34.9
63.05	41.6	18835	-59.4	7.6	34.7
66.17	30.0	20883	-59.2	7.7	34.4
66.73	20.0	23427	-58.8	7.7	34.4
66.75	19.6	23554	-58.8	7.7	34.4
68.03	10.0	27711	-65.8	7.1	34.2
70.00	0.0	28794	-69.3	6.7	34.2
70.07	0.0	28794	-68.5	6.8	34.2
70.13	0.0	28794	-67.6	6.9	34.3
70.25	0.0	28794	-65.7	7.1	34.4

TIME MIN.	PRESSURE MBARS	HEIGHT M-MSL	TEMP CEL.	DP-DEP CEL.	RH PERCENT
70.32	0.0	28794	-64.7	7.2	34.4
71.78	0.0	30992	-43.0	8.5	38.1
71.85	0.0	30992	-42.0	8.5	38.4
71.92	0.0	30992	-41.0	8.5	39.0
71.98	0.0	30992	-40.3	8.4	39.7
72.03	0.0	30992	-39.4	8.3	40.7
72.10	0.0	30992	-38.5	8.1	41.8

WIND VELOCITY

TIME MIN.	HEIGHT M-AS	DIRECTION DEGREES	SPEED KNOTS	HEIGHT FT-MSL
0	0	79	29.0	0.0
1	204	102	21.3	668.7
2	424	99	11.6	1391.1
3	718	94	6.8	2356.5
4	1038	49	2.8	3405.5
5	1358	43	3.4	4453.8
6	1677	67	3.1	5502.1
7	2015	116	3.3	6612.5
8	2329	178	3.5	7641.8
9	2668	188	6.2	8753.4
10	2978	216	6.8	9769.3
11	3292	247	6.1	10801.2
12	3582	246	7.2	11751.0
13	3856	212	9.4	12652.3
14	4139	199	12.7	13578.1
15	4421	198	10.7	14503.9
16	4708	206	9.8	15444.7
17	5000	219	10.4	16404.0
18	5292	234	12.2	17363.2
19	5585	220	12.2	18322.4

TIME MIN.	HEIGHT M-AS	DIRECTION DEGREES	SPEED KNOTS	HEIGHT FT-MSL
20	5877	234	10.6	19281.6
21	6169	257	13.1	20240.8
22	6462	256	19.3	21200.0
23	6770	248	21.1	22210.5
24	7083	246	26.9	23239.4
25	7397	265	21.1	24268.4
26	7715	284	25.6	25311.6
27	8054	292	33.5	26423.3
28	8395	295	37.6	27541.5
29	8662	296	39.0	28418.8
30	8943	291	35.3	29339.8
31	9277	283	31.0	30435.6
32	9588	268	25.6	31456.6
33	9889	255	26.2	32445.6
34	10191	240	27.2	33434.6
35	10494	239	28.0	34428.0
36	10801	229	37.7	35437.7
37	11107	246	36.0	36440.2
38	11409	260	29.0	37432.3
39	11730	284	20.1	38485.2
40	12029	247	23.4	39464.0
41	12316	243	21.9	40408.2
42	12598	248	18.4	41331.0
43	12879	255	16.7	42253.8
44	13161	251	13.0	43178.2
45	13443	209	11.8	44103.5
46	13723	197	14.4	45021.5
47	14002	203	8.3	45939.2
48	14282	24	2.9	46856.9
49	14575	50	10.9	47816.8
50	14868	79	15.7	48781.4

TIME MIN.	HEIGHT M-AS	DIRECTION DEGREES	SPEED KNOTS	HEIGHT FT-MSL
51	15163	87	19.7	49746.0
52	15457	90	19.1	50710.5
53	15751	102	20.4	51677.9
54	16048	107	18.6	52649.4
55	16355	95	19.7	53658.7
56	16665	80	20.4	54674.6
57	16970	86	23.9	55675.7
58	17270	97	23.8	56660.0
59	17568	100	21.7	57638.1
60	17874	97	13.0	58641.1
61	18189	88	13.2	59675.0
62	18504	89	19.2	60708.9
63	18819	96	25.4	61742.8
64	19459	106	27.2	63842.6
65	20116	106	27.1	65998.5
66	20773	106	27.1	68154.3
67	24364	106	27.1	79933.6
68	27603	106	27.1	90560.9
69	28794	277	47.8	94468.3

LIST OF REFERENCES

1. Walters, D. L., Favier, D. L., and Hines, J. R., "Vertical Path Atmospheric MTF Measurements," Journal of the Optical Society of America 69, pp. 828-837, 1979.

2. Walters, D. L. and Kunkel, K. E., "Atmospheric Modulation Transfer Function for Desert and Mountain Locations: The Atmospheric Effects on r_0," Journal of the Optical Society of America 71, pp. 397-405, 1981.

3. Jarem, J., "Remote Determination of the Structure Constant Profile from Amplitude Scintillation Data Using Tikhonov's Regularized Inverse Method," IEEE Transactions on Antennas and Propagation AP-31, pp. 145-148, 1983.

4. Jarem, J., "Remote Sensing of Structure Constant Profiles Using Tikhonov's Regularized Fourier Integral Method," Applied Optics 23, pp. 2614-2619, 1984.

5. Tikhonov, A. N., and Arsenin, V. Y., Solutions of Ill-Posed Problems, Wiley, New York, 1977.

6. Tatarski, V. I., Wave Propagation in a Turbulent Medium, Dover Publications, New York, p. 1967, 1961.

7. Tatarski, V. I., The Effects of the Turbulent Atmosphere on Wave Propagation, NTIS, U.S. Department of Commerce, 1971.

8. Tennekes, H. and Lumley, J. L., A First Course in Turbulence, The M.I.T. Press, Cambridge, Massachusetts, 1972.

9. Landau, L. D. and Lifshitz, E. M., Fluid Mechanics, Vol. 6 of Course of Theoretical Physics, Pergamon Press, New York, 1959.

10. Monin, A. S. and Yaglom, A. M., Statistical Fluid Mechanics, the MIT Press, p. 9, 1971.

11. Kolmogorv, A. N., "The Local Structure of Turbulence in Incompressible Viscous Fluid for Very Large Reynolds Numbers," Doklady Akad. Nauk SSSR, 30, p. 301, 1941.

12. Lumley, J. L., Stochastic Tools in Turbulence, Academic Press, New York, 1970.

13. Batchelor, G. K., The Theory of Homogeneous Turbulence, Cambridge University Press, London, 1959.

14. Walters, D. L., "Propagation Through Atmospheric Turbulence," High Energy Laser Propagation Handbook, Chapter 5, Optimetrics, Inc., Ann Arbor, Michigan, 1983.

15. Clifford, S. F., "The Classical Theory of Wave Propagation in a Turbulent Medium," Topics in Applied Physics, Laser Beam Propagation in the Atmosphere, Vol. 25, Chapter 2, Springer-Verlag, 1978.

16. Lutomirski, R. F. and Yura, H. T., "Propagation of a Finite Optical Beam in an Inhomogeneous Medium," Applied Optics 10, pp. 1652-1658, 1971.

17. Lutomirski, R. F. and Yura, H. T., "Wave Structure Function and Mutual Coherence Function of an Optical Wave in a Turbulent Atmosphere," Journal of the Optical Society of America 61, pp. 482-487, 1971.

18. Born, M. and Wolf, E., Principles of Optics, Sixth Edition, Pergamon Press, Oxford, 1980.

19. Fried, D. L., "Optical Resolution through a Randomly Inhomogeneous Medium for Very Long and Very Short Exposures," Journal of the Optical Society of America 56, pp. 1372-1379, 1966.

20. Fried, D. L., "Limiting Resolution Looking Down through the Atmosphere," Journal of the Optical Society of America 56, pp. 1380-1384, 1966.

21. Fried, D. L., "Anisoplanatism in Adaptive Optics," Journal of the Optical Society of America 72, pp. 52-61, 1982.

22. Fried, D. L., "Aperture Averaging of Scintillations," Journal of the Optical Society of America 57, pp. 169-175, 1967.

23. Loos, G. C. and Hogge, C. B., "Turbulence of the Upper-Atmosphere and Isoplanatism," Applied Optics 18, pp. 2654-2667, 1979.

24. Lutomirski, R. F., and Yura, H. T., "Aperture-Averaging Factor of a Fluctuating Light Signal," Journal of the Optical Society of America 59, pp. 1247-1248, 1969.

25. Dunphy, J. R. and Kerr, J. R., "Scintillation Measurements for Large Integrated-Path Turbulence," Journal of the Optical Society of America 63, p. 981, 1973.

26. Homstad, G. E., Strobehn, J. W., Berger, R. H., and Heneghan, J. M., "Aperture-Averaging Effects for Weak Scintillations," Journal of the Optical Society of America 64, pp. 162-165, 1974.

27. Azar, Z., Loebenstein, H. M., Appelbaum, G., Azoulay, E., Halavee, M., Tamir, M., and Tur, M., "Aperture Averaging of the Two-Wavelength Intensity Covariance Function in Atmospheric Turbulence," Applied Optics 24, pp. 2401-2407, 1985.

28. Clifford, S. F., Ochs, G. R., and Lawrence, R.S., "Saturation of Optical Scintillation by Strong Turbulence," Journal of the Optical Society of America 64, p. 148, 1974.

29. Strobehn, J. W., "Modern Theories in the Propagation of Optical Waves in a Turbulent Medium," Topics in Applied Physics, Laser Beam Propagation in the Atmosphere, Vol. 25, Chapter 3, Springer-Verlag, 1978.

30. Walters, D. L., Saturation and the Zenith Angle Dependence of Atmospheric Isoplanatic Angle Measurements, paper presented at the SPIE Conference, 11 April 1985.

31. Lee, R. W., "Remote Probing Using Spacially Filtered Apertures," Journal of the Optical Society of America 64, pp. 1295-1300, 1974.

32. Ochs, G. R., Wang, Ting-i, Lawrence, R. S., and Clifford, S. F., "Refractive-Turbulence Profiles Measured by One-Dimensional Spatial Filtering of Scintillations," Applied Optics 15, pp. 2504-2510, 1976.

33. Wang, Ting-i, Ochs, G. R., and Clifford, S. F., "A Saturation-Resistant Optical Scintillometer to Measure C_n^2," Journal of the Optical Society of America 68, pp. 334-338, 1978.

34. Bateman, H., Tables of Integral Transforms, Vol. 2, McGraw-Hill, Inc., New York, 1954.

35. U.S. Standard Atmosphere, 1962, National Aeronautics and Space Administration, United States Air Force, United States Weather Bureau, U.S. Government Printing Office, Washington, D.C., 1962.

36. Trout, D. and Panofsky, H. A., "Energy Dissipation Near the Tropopause," Tellus XXI, pp. 354-358, 1969.

37. Ellsaesser, H. W., "A Climatology of Epsilon (Atmospheric Dissipation)," Monthly Weather Review 97, pp. 415-423, 1969.

38. Chen, W. Y., "Energy Dissipation Rates of Free Atmospheric Turbulence," Journal of the Atmospheric Sciences 31, pp. 2222-2225, 1974.

39. Cadet, D., "Energy Dissipation within Intermittant Clear Air Turbulence Patches," Journal of the Atmospheric Sciences 34, pp. 137-142, 1977.

40. Frish, A. S. and Strauch, R. G., "Doppler Radar Measurements of Turbulent Kinetic Energy Dissipation Rates in a Northeastern Colorado Convective Storm," Journal of Applied Meteorology 15, pp. 1012-1017, 1976.

41. Gage, K. S., Green, J. L., and Van Zandt, "Use of Doppler Radar for the Measurement of Atmospheric Turbulence Parameters from Intensity of Clear-Air Echoes," Radio Science 15, pp. 407-416, 1980.

42. Van Zandt, T. E., Green, J. L., Gage, K. S., and Clark, W. L., "Vertical Profiles of Refractivity Turbulence Structure Constant: Comparison of Observations by the Sunset Radar with a New Theoretical Model," Radio Science 13, pp. 819-829, 1978.

43. Bean, B. R., "Application of FM-CW Radar and Acoustic Echo-Sounder Techniques to Boundary Layer and CAT Studies," Remote Sensing of the Troposphere, Chapter 20, U.S. Government Printing Office, Washington, D.C., 1972.

44. Wang, Ting-i, Ochs, G. R., and Lawrence, R. S., "Wind Measurements by the Temporal Cross-Correlation of the Optical Scintillations," Applid Optics 20, pp. 4073-4081, 1981.

45. Peskoff, A., "Theory of Remote Sensing of Clear-Air Turbulence Profiles," Journal of the Optical Society of America 58, pp. 1032-1040, 1968.

46. Shen, Liang-Chi, "Remote Probing of Atmosphere and Wind Velocity by Millimeter Waves," IEEE Transactions on Antennas and Propagation AP-18, pp. 493-497, 1970.

47. Heneghan, J. M., and Ishimaru, A., "Remote Determination of the Profiles of the Atmospheric Structure Constant and Wind Velocity Along a Line-of-Sight Path by a Statistical Inversion Procedure," IEEE Transactions on Antennas and Propagation AP-22, pp. 457-464, 1974.

48. Rocca, A. Roddier, F., and Vernin, J., "Detection of Atmospheric Turbulent Layers by Spaciotemporal and Spacioangular Correlation Measurements of Stellar-Light Scintillation," Journal of the Optical Society of America 64, pp. 1000-1004, 1974.

49. Azouit, M. and Vernin, J., "Remote Investigation of Tropospheric Turbulence by Two-Dimensional Analysis of Stellar Scintillation," Journal of the Optical Society of America 37, pp. 1550-1557, 1980.

50. Vernin, J. and Azouit, M., "Traitement D'Image Adapte Au Speckle Atmospherique, II. Analyse Multidimensionnelle Appliquee Au Diagnostic A Distance De La Turbulence," Journal Optics 14, pp. 131-142, 1983.

51. Yariv, A., Optical Electronics, 3rd edition, Holt, Rinehart and Winston, New York, 1985.

52. Observer's Handbook 1985, The Royal Astronomical Society of Canada, Toronto, 1985.

53. RCA Electro-Optics Handbook, RCA Corporation, 1974.

54. Brigham, E. O., The Fast Fourier Transform, Prentice-Hall, Inc., New Jersey, 1974.

55. Nyquist, H., "Certain Topics in Telegraph Transmission Theory," Transactions of the A.I.E.E., pp. 617-644, April 1928.

56. Knuth, D. E., Seminumerical Algorithms: The Art of Computer Programming, Vol. 2, Addison-Wesley, Reading, MA, p. 117, 1981.

INITIAL DISTRIBUTION LIST

		No. Copies
1.	Defense Technical Information Center Cameron Station Alexandria, Virginia 22304-6145	2
2.	Library, Code 0142 Naval Postgraduate School Monterey, California 93943-5100	2
3.	Professor Donald L. Walters, Code 61We Naval Postgraduate School Monterey, California 93943-5100	15
4.	AFIT/CIRD Wright-Patterson AFB, Ohio 45433	1
5.	CAPT Kurt B. Stevens 45 Tuscarora Street Addison, New York 14801	3

Thesis
S71292
c.1

215334

Stevens

Remote measurement of the atmospheric isoplanatic angle and determination of refractive turbulence profiles by direct inversion of the scintillation amplitude covariance function with Tikhonov regularization.